

# Excitation and acceleration of atoms in tailored strong laser fields

vorgelegt von  
Dipl. Phys. Sebastian EILZER  
geb. in Großröhrsdorf

von der Fakultät II - Mathematik und Naturwissenschaften  
der Technischen Universität Berlin  
zur Erlangung des akademischen Grades  
Doktor der Naturwissenschaften  
- Dr. rer. nat.-  
genehmigte Dissertation

Promotionsausschuss:

Vorsitzender: Prof. Dr. Andreas KNORR  
Gutachterin: Prof. Dr. Olga SMIRNOVA  
Gutachter: Prof. Dr. Gerhard PAULUS

Tag der wissenschaftlichen Aussprache: 25. November 2016

Berlin 2017



# Selbständigkeitserklärung

Die selbständige und eigenhändige Anfertigung dieser Dissertation versichere ich an Eides statt. Alle genutzten Quellen und Hilfsmittel sind in der Dissertation aufgeführt.

Berlin, den

---

Sebastian Eilzer



# Zusammenfassung

Diese Forschungsarbeit untersucht die neu gefundene Wirkung der frustrierten Tunnelionisation (FTI) in komplexen elektromagnetischen Feldkonfigurationen. Nach der Entdeckung, dass neutrale Atome starke Laserfelder überleben können, wurde die Stabilität dieser Atome gegen Ionisation, als auch die Beschleunigung dieser Atome getestet. Diese Arbeit erweitert daher das Verständnis der Prozesse die innerhalb der Starkfeldinteraktion auftreten können.

Umfangreiche experimentelle Untersuchungen mit zwei Laseraufbauten erlaubte die Messung mehrerer wichtiger Aspekte der FTI. Ein Zwei-Puls Experiment ermöglichte die Interaktion von Rydberg Atomen mit starken Laserfeldern, während eine stehende Welle die Untersuchung der FTI im Umfeld starker Feldgradienten erlaubte. Weiterhin wurde mit systematischen Monte-Carlo Simulationen ein Vergleich zwischen allen Messungen sowie den Experimenten durchgeführt. Hierbei konnten sowohl die Unterschiede verschiedener Modelle analysiert werden, als auch die Vereinfachungen aufgezeigt werden, welche realistische Ergebnisse ermöglichen.

Mehrere Entdeckungen sind im Umfang dieser Arbeit gemacht worden. So konnte der Einfluss des FTI Prozesses auf die Ionisationsraten nachgewiesen werden, welcher durch Einführung des Coulombfeldes bei der Betrachtung der Kinematik nach dem Tunneln berücksichtigt werden kann. Desweiteren wurde die hohe Stabilität der präparierten Rydberg Atome gegen Ionisation durch ein starkes Laserfeld beobachtet. In diesem Zusammenhang wurde ebenfalls eine kontrollierte Methode vorgestellt um neutrale Atome gezielt zu steuern, welche sehr gute Übereinstimmung mit der Theorie aufweist. Schließlich wurde das empfindliche Zusammenspiel der Ionisation und der Beschleunigung innerhalb der stehenden Welle entdeckt und untersucht.



# Abstract

This research investigates the new found effect of frustrated tunnelling ionisation (FTI) in complex electromagnetic field configurations. After the surprising finding of neutral atoms which survive strong laser fields, more light had to be shed on their stability against ionisation as well as the record acceleration of neutral atoms measured in conjunction with this effect. This research therefore expands the picture of strong field light matter interaction towards a deeper understanding of the many processes that can take place in this regime.

Extensive experimental research using two unique laser setups allowed to measure several key aspects of the FTI process. A two pulse experiment made exposure of Rydberg atoms to strong laser fields possible while a femtosecond standing wave setup permitted the study of the FTI process in the presence of an oscillating field gradient. Additionally, systematic Monte-Carlo simulations of the exposed atoms performed for all experimental setups allowed the comparison of the experimental findings and the theoretical picture. Different theories have been used in the calculations to pinpoint the differences as well as to identify the simplifications allowed to still yield valuable results.

Several discoveries have been made throughout the research. Firstly, the influence of the FTI process on the calculation of strong field ionisation rates has been introduced which can be included by considering the Coulomb influence of the atom after tunnelling. Secondly, Rydberg atoms have been found to be very stable against ionisation with short pulses of high field strength. A controlled method to steer neutral atoms with two consecutive pulses has been presented and shows high agreement with the calculation. Lastly, the delicate interplay between ionisation and acceleration inside the high field gradient conditions provided by a standing wave has been detected and investigated.



Publications arising from this thesis:

- U.Eichmann, A. Saenz, S. Eilzer, T.Nubbemeyer and W. Sandner, *Observing Rydberg Atoms to Survive Intense Laser Fields*, Phys. Rev. Lett. **110**, 203002 (2013).
- S. Eilzer, H. Zimmermann and U. Eichmann, *Strong-Field Kapitza-Dirac Scattering of Neutral Atoms*, Phys. Rev. Lett. **112**, 113001 (2014).
- S. Eilzer and U. Eichmann, *Steering neutral atoms in strong laser fields*, J. Phys. B: At. Mol. Opt. Phys. **47**, 204014 (2014).

Additional publications not covered in this thesis:

- H. Zimmermann, J. Buller, S. Eilzer and U. Eichmann, *Strong-Field Excitation of Helium: Bound State Distribution and Spin Effects*, Phys. Rev. Lett. **114**, 123003 (2015).



# Contents

<b>1</b>	<b>Introduction</b>	<b>1</b>
<b>2</b>	<b>Atoms in strong laser fields</b>	<b>5</b>
2.1	Light matter interaction . . . . .	5
2.2	Excitation of neutral atoms in strong laser fields . . . . .	14
2.3	Acceleration of excited neutral atoms . . . . .	21
<b>3</b>	<b>Experimental setup</b>	<b>25</b>
3.1	Detection of neutral atoms . . . . .	25
3.2	Vacuum setup . . . . .	29
3.3	Laser system . . . . .	30
3.4	Two pulse setup . . . . .	32
3.5	Standing wave setup . . . . .	34
3.6	Beam characterisation . . . . .	35
<b>4</b>	<b>Two pulse excitation and acceleration</b>	<b>39</b>
4.1	Exposing neutral Rydberg atoms to a strong laser field . . . . .	39
4.2	Classical trajectory calculation with two pulses . . . . .	41
4.3	Steering of neutral atoms with strong fields . . . . .	48
4.4	Conclusion . . . . .	53
<b>5</b>	<b>Standing Wave</b>	<b>55</b>
5.1	Electromagnetic field configuration . . . . .	56
5.2	Simple quantum mechanical model . . . . .	62
5.3	Observing the standing wave deflection . . . . .	64
5.4	Semi classical simulation . . . . .	80
5.5	Conclusion . . . . .	94
<b>6</b>	<b>Summary</b>	<b>97</b>

<b>Appendix</b>	<b>101</b>
<b>List of Figures</b>	<b>107</b>
<b>Bibliography</b>	<b>111</b>

# 1 Introduction

The interaction of laser light with atoms is a fundamental pillar of modern research. The electromagnetic fields produced by a modern laser system are used to test theories about the fundamental interactions of atoms and molecules. Physics always needs the experiment to apply and check predictions of the predominant models. Therefore, theory and experiment inspire and stimulate each other all the time. While for example quantum dynamics can be used to calculate many interactions that are observable today, it is often not feasible because of the huge calculating effort that is needed, even for effects where only very few particles are involved. It is therefore necessary to develop models which explain certain aspects of a process in such a way, that reliable predictions can be made with reasonable effort. Hence, experimental research in new areas, not accessible before, has to be done to test these theories in extreme conditions. Either known correlation are validated or new pictures can be formed which include all found results.

A good example is the light matter interaction of single atoms in electromagnetic fields. In the beginning ionisation was explained by introducing the quantum nature of photons and the related wavelength dependence [1]. It was called the photoeffect. But already in the early 1930s the theory of ionisation with several photons of any arbitrary wavelength was introduced [2]. The so called multi-photon ionisation (MPI), where more than one photon needs to be absorbed to overcome the energy gap, could only be observed many years later when lasers provided the high photon flux necessary for it to take place [3]. With even higher intensities the new process of above threshold ionisation (ATI) was discovered experimentally [4] and could be included in the established picture with perturbation theory. In this case more photons are absorbed than necessary for ionisation. The additional energy is converted into kinetic energy of the ionised electron.

Along with constant development in the laser research, higher and higher peak intensities could be realised in laboratories. When reaching intensities close to the atomic field strength ( $5.14 \cdot 10^{11}$  V/m) perturbation theory cannot be used anymore, as the perturbation itself is not small compared to the fundamental field. The so-called tunnelling theory by L. V. Keldysh proved a very valuable picture for a descriptive explanation of many new processes found in this regime [5]. It also introduced the  $\gamma$ -parameter, which can be used to distinguish the wavelength and intensity range where it is reasonable to use the tunnelling picture or the multi photon picture. After including some corrections, this model is very successful in providing ionisation rates [6, 7] which reproduce experimental measurements including the sequential multiple ionisation [8].

To include the observed nonlinear processes such as the non-sequential double ionisation (NSDI), the ATI plateau [9] or high harmonic generation (HHG) [10] P. Corkum suggested an extension of the tunnelling model by including ideas about the mechanisms of the energy absorption in the strong field which have been developed at that time [11, 12]. The so-called three-step model includes the dynamics of the electron after the tunnelling. The electron is then driven in the field of the laser pulse and gains energy depending on the time of tunnelling. In a linear polarised field the electron can return to the ionic core and interact with it. If the electron scatters on the ionic core and its energy is transferred to an additional electron which gets ionised, the non-sequential double ionisation can be explained. In the case of the recombination of the initial electron with the core, the gained energy leads to the emission of a photon and high harmonic generation can be calculated.

For ease of calculation the model did not include the Coulomb potential of the parent atom when calculating the trajectories. Since the electron is far away from the core for most of the time, the influence of the ionic core was believed to be small. In depth calculations performed in the extent of this thesis reveal how much the Coulomb field actually influences the trajectories after tunnelling depending on the energy (see section 2.2).

Specifically including the Coulomb field also opens the possibility to understand an additional process taking place in this regime. Electrons gaining low drift momentum never leave the Coulomb potential, which means that the atom is never ionised, although the electron tunnels through the barrier by

---

the combined Coulomb and laser field. The neutral atom survives the intense laser pulse as a Rydberg atom. The process was predicted theoretically [13] and dubbed frustrated tunnelling ionisation (FTI) after finding the experimental evidence [14].

The goal of this thesis is twofold and two different setups were therefore realised to measure strong field effects.

The stability of the Rydberg atoms which stem from the FTI process was tested with a novel method, which ensures that the Rydberg atoms experience the full intensity of a second laser field. Stabilisation of atoms in intense laser fields was predicted very early [15–17] and discussed theoretically extensively throughout the years [18–20]. Different stabilisation methods have been suggested for Rydberg atoms such as interference stabilisation [21–25], dynamic stabilisation [26, 27] or inhibited ionisation due to high angular momentum [28]. Several experiments, mostly at lower intensities, have been performed [29–34]. It is, therefore, interesting to investigate the stabilisation at higher intensities where the Keldysh theory can only give insight into ionisation from the ground state. The behaviour of Rydberg atoms should be dramatically different however. In the proposed pump-probe type setup Rydberg atoms are firstly produced according to the FTI theory, and afterwards they are exposed to a second pulse they interact with. Due to the intentional use of different polarisations the atoms that interact with the full intensity of the second laser pulse can be identified. Therefore, it can be made sure that Rydberg atoms experiencing intensities of  $10^{15} \text{ W/cm}^2$  actually survive the laser pulse.

Knowing that the atoms do survive, the acceleration observed in conjunction with the FTI process can be exploited to control neutral atoms. A scheme to steer neutral atoms is presented together with the survival experiment. The results and the theory explaining the survival and steering are presented in chapter 4.

With the second setup a different kind of electromagnetic field is utilised to produce and accelerate Rydberg atoms. Two counter-propagating laser pulses are overlapped to form a standing wave with high intensity. The magnetic component of the laser field is usually neglected in the non relativistic regime because of its weakness compared to the electric field component. In the

standing wave, however, areas of pure electric and pure magnetic field exist. Additionally, the gradient of the electric field, which is responsible for the observed acceleration, changes on a much smaller scale. Here it is on the scale of the laser wavelength, while it is on the scale of the focus spot in case of a classical single pulse process. Therefore, a deflection of neutral atoms can be observed that is caused by the standing wave. This corresponds to the Kapitza-Dirac effect, which deals with the deflection of matter by a standing light wave. Originally the effect was formulated only for electrons [35] but neutral atoms were included later [36]. In the weak field case it has been studied thoroughly [37–40] with applications for example in quantum gas control. In the high field case many calculations have been performed [41–47] but only very few experiments exclusively with electrons [48–50].

The setup introduced in this thesis is used to accelerate neutral atoms on a light grating produced by two counter-propagating high intensity laser pulses. A specific polarisation scheme is used, which allows a background free observation of atoms stemming purely from the standing wave. Additionally, it enables a continuous change of the gradient strength inside the standing wave to unravel the FTI process in a wider array and with unprecedented maximum electric field gradient. The polarisation scheme, complex trajectory calculations and experimental results are shown in chapter 5.

Chapter 2 gives a brief introduction into the physical foundation of the light matter interaction, as well as an insight into the principle of the FTI process, while chapter 3 explains the laboratory setups used to obtain the experimental data in this thesis. Chapter 6 finally concludes this thesis with an overview over the accomplishments and the physical insight that was obtained.

## 2 Atoms in strong laser fields

### 2.1 Light matter interaction

To fully describe the non relativistic behaviour of atoms in strong laser fields one has to solve the Schrödinger equation

$$i\hbar\frac{\partial}{\partial t}\psi(\mathbf{r}, t) = \hat{H}\psi(\mathbf{r}, t) \quad (2.1)$$

with

$$\hat{H} = \frac{1}{2} \left( \mathbf{p} + \frac{1}{c} \mathbf{A}(\mathbf{r}, t) \right)^2 - \Phi(\mathbf{r}, t) + V(\mathbf{r}, t),$$

where  $\mathbf{p}$  represents the momentum and  $V$  an arbitrary potential.

In most cases, however, this is not possible and one has to use simplified models which can explain certain problems and predict reliable results for subsequent experiments.

The magnetic vector potential  $\mathbf{A}$  and the scalar electric potential  $\Phi$  inside the Hamiltonian are not observables themselves, they are only defined over the electric field  $\mathbf{E}$  and the magnetic field  $\mathbf{B}$  which can be measured.

$$\mathbf{B} = \nabla \times \mathbf{A} \quad (2.2)$$

$$\mathbf{E} = -\nabla\Phi - \frac{\partial\mathbf{A}}{\partial t} \quad (2.3)$$

Because of this, there exists a certain gauge freedom for these potentials.

$$\mathbf{A}' = \mathbf{A} + \nabla f \quad (2.4)$$

$$\Phi' = \Phi - \frac{1}{c} \frac{\partial f}{\partial t} \quad (2.5)$$

If one assumes the dipole approximation, which states that the electromagnetic field is constant over the dimension of an atom, which holds true for wavelengths in the infrared (IR) region, the problem can be simplified.

For a plane wave in Coulomb gauge ( $\Phi = 0$  and  $\mathbf{A} = \mathbf{A}_0 \cos(\omega t)$ ), one can choose  $f$  to be

$$f = -\mathbf{A}_0 \cdot \mathbf{r} \cos(\omega t) \quad (2.6)$$

( [51], pages 9 ff), which yields for the potentials

$$\mathbf{A}' = \mathbf{A} - \nabla(\mathbf{A}_0 \cdot \mathbf{r}) \cos(\omega t) = 0, \quad (2.7)$$

$$\Phi' = \Phi + \frac{\omega}{c} \mathbf{A}_0 \cdot \mathbf{r} \sin(\omega t) = \frac{\omega}{c} \mathbf{A}_0 \cdot \mathbf{r} \sin(\omega t). \quad (2.8)$$

Choosing this form is also called length gauge and yields the following Hamiltonian

$$\hat{H} = \frac{\mathbf{p}^2}{2} - \frac{\omega}{c} \mathbf{A}_0 \cdot \mathbf{r} \sin(\omega t) + V(\mathbf{r}, t). \quad (2.9)$$

The advantage of the length gauge lies in the fact, that the momentum  $\mathbf{p}$  is identical to the measured kinetic momentum of the electron in the lab frame. Also, especially in the case of time independence, the visualisation of the combined potential  $\Phi(\mathbf{r}) + V(\mathbf{r})$  is rather descriptive and easy to apprehend.

In contrast to this gauge, one can choose  $f$  in a way so that the potential  $\Phi$  vanishes. This is called velocity gauge.

$$f_1 = \omega \int \mathbf{A}_0 \cdot \mathbf{r} \sin(\omega t) dt, \quad (2.10)$$

which leads to the Hamiltonian

$$\hat{H} = \frac{1}{2} \left( \mathbf{p} + \frac{1}{c} \mathbf{A} \right)^2 + V(\mathbf{r}, t) = \frac{\mathbf{p}^2}{2} + \frac{\mathbf{A} \cdot \mathbf{p}}{c} + \frac{A^2}{2c^2} + V(\mathbf{r}, t)$$

with

$$\mathbf{A} = \omega \int \mathbf{A}_0 \sin(\omega t) dt.$$

$\frac{A^2}{2c^2}$  does not depend on the position  $\mathbf{r}$  and can thus be interpreted as a new potential. With a subsequent gauge transformation

$$f_2 = -\frac{1}{2c} \int_0^t A^2(t') dt' \quad (2.11)$$

one ends with

$$\hat{H} = \frac{\mathbf{p}^2}{2} + \frac{\mathbf{A} \cdot \mathbf{p}}{c} + V(\mathbf{r}, t), \quad (2.12)$$

$$\Phi = 0, \quad (2.13)$$

$$\mathbf{A} = \omega \int \mathbf{A}_0 \sin(\omega t) dt. \quad (2.14)$$

The solutions of the Schrödinger equation in this gauge represents the multiphoton picture of ionisation. The graphic description of the potential compared to length gauge is lost however.

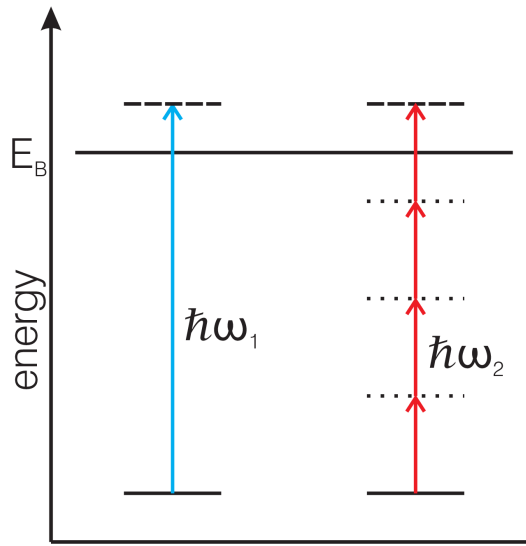


Figure 2.1: Photo ionisation with a photon of high frequency  $\omega_1$  and multiphoton ionisation with several photons of lower frequency  $\omega_2$ .

After explaining the fundamental formulas, one can now have a look at the processes which have been observed. In the case of classical excitation, which occurs in weak laser fields, the energy needed to excite an electron into a higher state or into the continuum is provided by a single photon (photo ionisation - PI). If the photon flux is high enough an atom can also be ionised by photons with lower energy. This is called multiphoton ionisation (MPI) and it occurs when, during excitation of an intermediate virtual energy-level (given by the time-energy uncertainty), enough photons are available to excite the electron even higher.

The energy of such a photoelectron is given by

$$E_e = n\hbar\omega - E_B, \quad (2.15)$$

with  $n = 1$  for PI and  $n > 1$  for MPI.  $E_B$  is the binding energy of the electron inside the parent atom and  $\omega$  the frequency of the photons.

For even higher intensities one can observe above threshold ionisation (ATI), which can be included in the multiphoton picture by perturbation theory. The electron accumulates more energy than necessary for ionisation

$$E_e = (n + s)\hbar\omega - E_B, \quad (2.16)$$

where  $s$  stands for the amount of excess electrons absorbed.

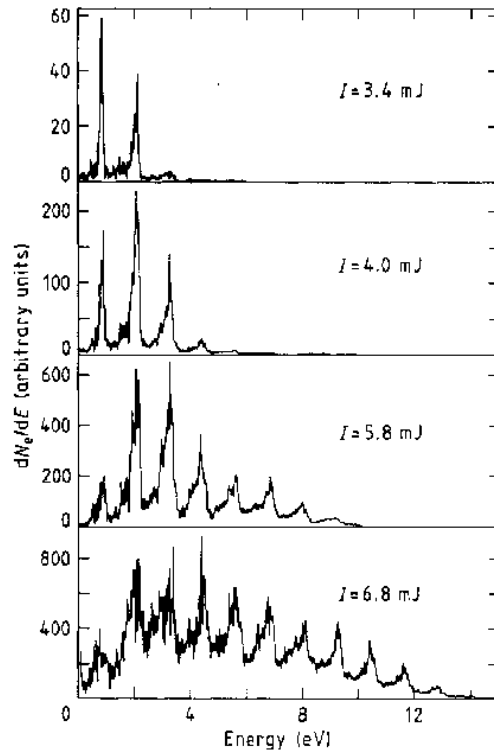


Figure 2.2: Photoelectron energy spectrum of ATI-peaks with different pulse energies from [52].

The ATI spectrum changes its appearance with higher and higher intensities (see figure 2.2). The spectrum loses its discrete nature and a broad continuous spectrum begins to show. Additionally, the first peak slowly

vanishes, which can be understood by including the shift of the energy levels that the atom experiences in a strong field.

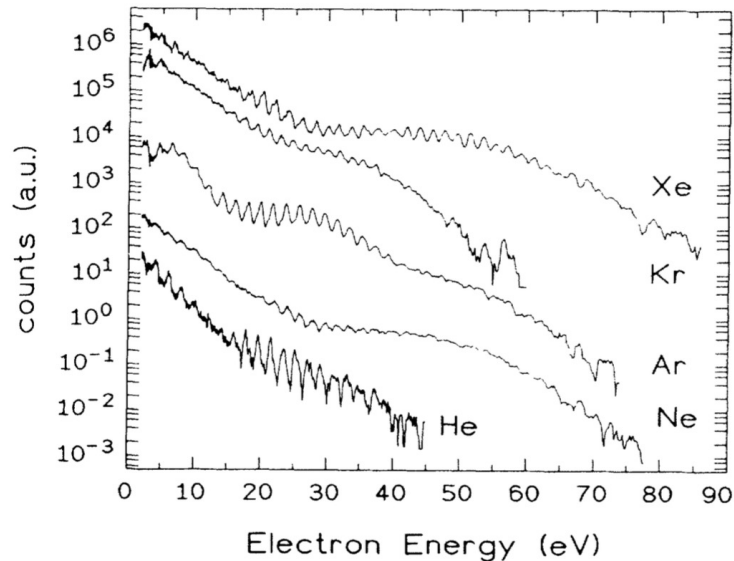


Figure 2.3: Observation of the plateau region of different noble gases from [9].

With even higher intensities, where the perturbation theory cannot be used anymore, a new feature was found. The photoelectron spectrum does not follow the expected exponential decrease, but instead develops a plateau region (see figure 2.3). The investigation of this plateau region has been performed extensively and gave rise to the investigation of new effects such as high above threshold ionisation [9].

For a slowly varying electric field, which holds true for wavelengths in the infrared spectrum, and field strengths on the order of the atomic field strength ( $5.14 \cdot 10^{11} \text{ V/m}$ ) it has been successful to look at the combined field of the quasi-static electric component of the laser field and the Coulomb potential (see equation 2.9; length gauge). More precisely the Coulomb potential is treated as a perturbation to the laser field, which constitutes the main influence on the electron. This combined potential has a saddle point and electrons can tunnel from the Coulomb potential through the finite barrier (see figure 2.4 a) when the laser field reaches its maximum. Because of this, the model is called the tunnelling picture of strong field ionisation. With the help of this model several effects in strong field interaction can be explained. With even higher field strength the distortion becomes so high that for weakly bound electrons

the barrier is lowered below their energy level and they can leave the core directly into the continuum. This is called above barrier ionisation (ABI) and resembles the classical field ionisation (see figure 2.4 b).

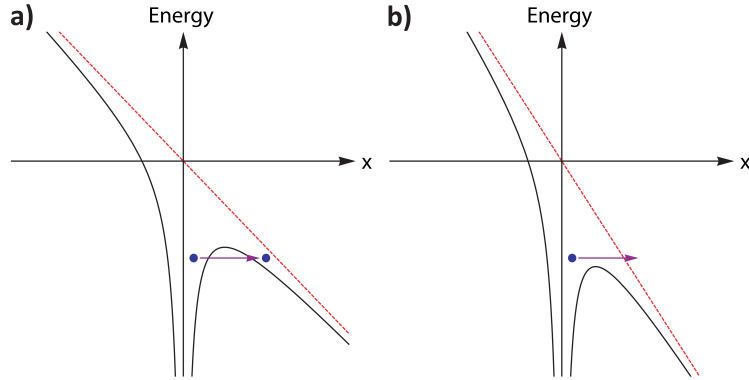


Figure 2.4: Tunnel ionisation at lower field strength (a) and ABI at high field strength (b).

To distinguish between multiphoton picture and tunnelling picture L.V. Keldysh introduced a parameter [5]

$$\gamma = \sqrt{\frac{E_B}{2U_P}}, \quad (2.17)$$

with

$$U_P = \frac{I}{4\omega^2},$$

where  $E_B$  is the binding potential of the electron,  $I$  the intensity in the focus area of the laser and  $U_P$  the ponderomotive energy. In the extreme cases  $\gamma \gg 1$  the multiphoton picture yields good results and for  $\gamma \ll 1$  the tunnelling picture is applicable. At a Keldysh parameter slightly below 1 tunnelling through the barrier can occur.

In case of helium interacting with wavelengths at the upper end of the visible spectrum ( $\approx 800 \text{ nm}$ ) and intensities in the range of  $10^{15} - 10^{16} \text{ W/cm}^2$ , as used in the experiments, one is well in the area of tunnelling ionisation with  $\gamma$  in the range of 0.1 – 0.5. For processes observed at these wavelengths like high harmonic generation (HHG) [10, 53, 54] or non sequential double ionisation (NSDI) [55–57] the three-step model as described by P. Corkum [58] can give a very descriptive explanation.

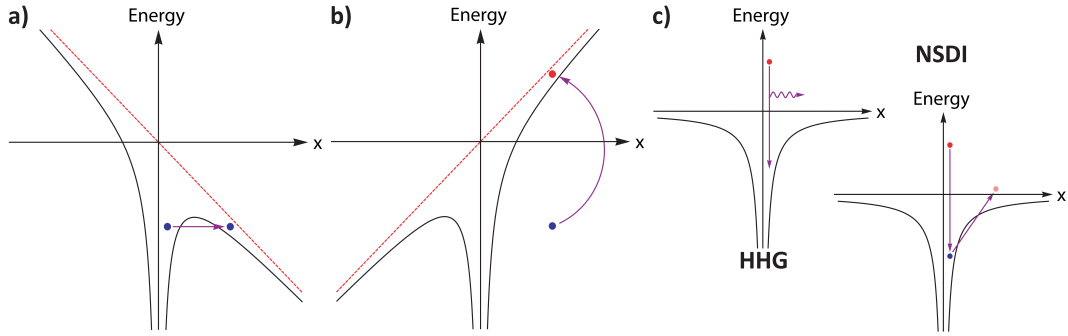


Figure 2.5: Three-step model of P. Corkum:

- a) Tunnel ionisation
- b) Acceleration in the laser field
- c) Return to the core and recombination or scattering at it

In the first step an electron can tunnel through the barrier created by the distorted Coulomb potential (see figure 2.5 a). The tunnelling probability can be calculated from the complex theory by A. M. Perelomov, V. S. Popov and M. V. Terentev (PPT-theory [6]) which includes oscillations of the deformed Coulomb potential, or the slightly more accessible theory by M. V. Ammosov, N. N. Delone and V. P. Krainov (ADK-theory [7]) which assumes a static field. Afterwards the electron is treated like a classical charge in the electromagnetic field of the laser, where it is accelerated (see figure 2.5 b). The force acting on the electron is the Lorentz force

$$\mathbf{F}_L = q(\mathbf{E} + \dot{\mathbf{r}} \times \mathbf{B}). \quad (2.18)$$

In the case of linear polarised light the periodical change of the laser field after half a cycle causes the electron to return close to the core area. For elliptical polarised light the laser drift momentum is always nonzero and increases with higher ellipticity [59]. Because of that, the electron will always be driven away from the core. The distinctly different behaviour of the recombination process for higher ellipticities due to the wave packet missing the core, compared to strong field ionisation, is shown in figure 2.6.

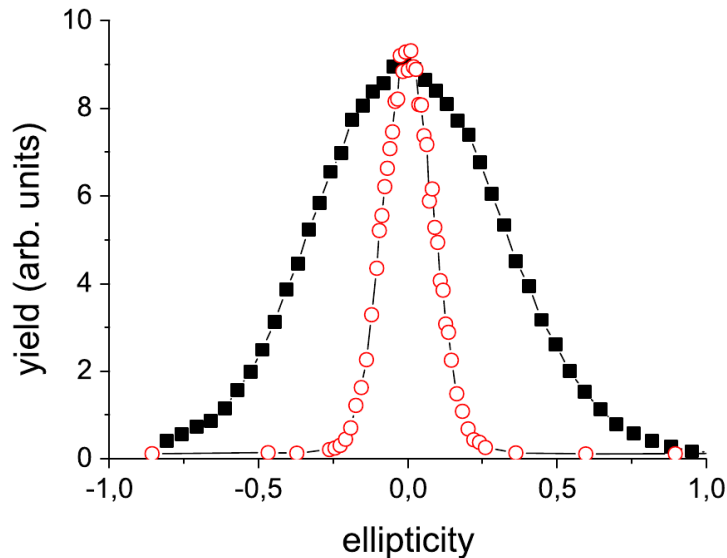


Figure 2.6: Dependence of the  $\text{He}^+$  (■) and  $\text{He}^*$  (○) yield on ellipticity from [14].

In dipole approximation the magnetic field component  $\mathbf{B}$  is neglected for the non relativistic case ( $v \ll c$ ). By inserting a linear polarised field in  $x$ -direction  $\mathbf{E} = \mathbf{E}_0 \cos(\omega t)$ , with  $\mathbf{E}_0 = E_0 \mathbf{e}_1$  and  $\mathbf{e}_1$  as unit vector in  $x$ -direction, one arrives at

$$\ddot{\mathbf{r}}(t) = \mathbf{e}_1 \frac{-eE_0}{m_e} \cos(\omega t). \quad (2.19)$$

The velocity is calculated by simple integration

$$\dot{\mathbf{r}}(t) = \mathbf{e}_1 \frac{-eE_0}{m_e \omega} (\sin(\omega t) - \sin(\omega t_0)) \quad (2.20)$$

and the trajectory by double integration

$$\mathbf{r}(t) = \mathbf{e}_1 \frac{-eE_0}{m_e \omega^2} (\cos(\omega t_0) - \cos(\omega t) + \omega(t_0 - t) \sin(\omega t_0)). \quad (2.21)$$

From 2.20 one can calculate the drift energy. By cycle averaging over the laser period one yields

$$E_{kin} = \frac{1}{2} m_e \overline{v^2} = \frac{e^2 E_0^2}{2 m_e \omega^2} \left( \frac{1}{2} + \sin^2(\omega t_0) \right) = U_P (1 + 2 \sin^2(\omega t_0)). \quad (2.22)$$

The first constant  $U_P$  only has to be taken into account for long pulses where the electron leaves the focus region during the pulse length. For short pulses, which are over before the electron moves out of the focus, it has to be omitted, as the rising and the falling edge of the pulse cancel each other out. The maximum drift energy then calculates to  $2U_P$ . Additionally, one can see that the gained energy depends on the time of tunnelling  $t_0$ .

This description of the electron motion after ionisation is also known as the simple man's model [60] and was introduced to explain secondary processes such as ATI. In contrast to the three-step model it does not focus on the different effects that can happen when the electron returns, but instead on the energy the electron gains in the laser field. The influence of the ionic core was completely neglected in the first formulation of the simple man's model. It was successfully used to explain ATI effects in a wide array of parameters [61] or even with circular polarised light [62].

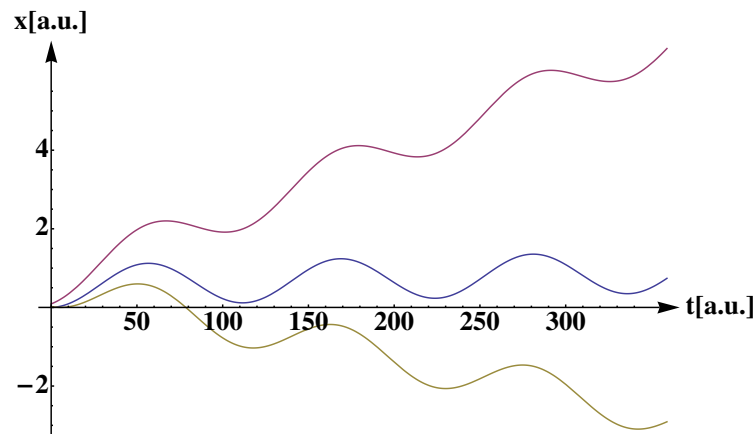


Figure 2.7: Electron trajectories for different ionisation times. Ionisation at  $55^\circ$  (red),  $88^\circ$  (blue) and  $108^\circ$  (yellow).

The trajectories of the electron for three different ionisation times are shown in figure 2.7. In the case of ionisation distinctly before the electric field maximum (which is located at  $90^\circ$ ) the electron just leaves the vicinity of the core (red curve). It can be detected as an ATI electron on a suitable detector. The electrons which are ionised well after the maximum return once to the core and can interact with it (yellow curve). During this process the obtained energy can either be employed to free another electron (NSDI) or the energy can be released as a high energy photon (HHG) (see figure 2.5 c). The pictured

case at  $108^\circ$  represents the maximum energy transfer from the laser field to the electron. Additionally to these two cases there exists a group of trajectories which start very close to the maximum (blue curve). These electrons return to the core several times and stay close to it even after the laser pulse is over. They are the basis for the process of frustrated tunnelling ionisation (FTI) which will be explained in the following section.

## 2.2 Excitation of neutral atoms in strong laser fields

In the weak field case the rate of ionisation for an atom in any bound state can be described with the well known Fermi's golden rule

$$\Gamma = \frac{2\pi}{\hbar} \left| \frac{d_{b \rightarrow f} \cdot \epsilon_0}{2} \right|^2, \quad (2.23)$$

which yields a transition rate  $\Gamma$  between two arbitrary states.  $\epsilon_0$  is the field strength and  $d$  denotes the dipole matrix element of the two states. In the case of ionisation a bound-free transition  $b \rightarrow f$  has to be used. For growing field strengths this rate increases until it finally reaches depletion, which would correspond to all atoms in the interaction area being ionised. However, this is not the case, as some atoms do survive very high field strength without being ionised.

Different descriptions have been found to explain this behaviour. In the strong field case the perturbation theory applied to obtain the golden rule cannot be used. Instead a new concept was developed, where the external field is the main influence on the energy states inside the atom, and a so called "dressed atom" is formed. New effects can be found in this regime, like stabilisation, which describes the resistance of an atom against ionisation. Some theories concern atoms in the ground state which withstand ionisation during a strong laser pulse and survive in an excited state, others deal with specific energy levels which do not get ionised during a strong pulse.

A basic concept for stabilisation was given 1988 by M. V. Fedorov and A. M. Movsesian [22] long before experimental observation and has been continuously

extended. The basic idea states, that an initially excited Rydberg state slowly populates its neighbouring levels over  $\Lambda$ -transitions with the continuum (see figure 2.8), or  $V$ -type transitions with a lower lying energy level.

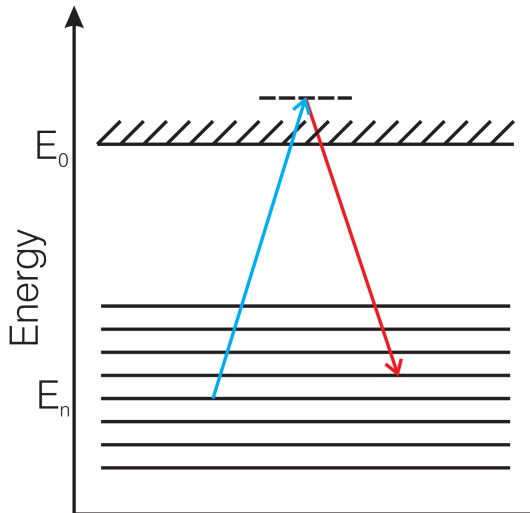


Figure 2.8: Sketch of a  $\Lambda$ -transition in a Rydberg atom. Neighbouring levels of  $E_n$  will be populated by photons inside the energy width of the laser pulse.

During ionisation from this equally populated ensemble, interference between the excited states will lead to suppressed transitions, which ultimately yields a survival probability for specific Rydberg states. Consequently this effect was called interference stabilisation. This process relies on the presence of many almost equally spaced energy levels, as they are existent for highly excited Rydberg atoms close to the ionisation energy. Atoms in the ground state are therefore assumed to get excited into such a state at the rising edge of the laser pulse, and to experience the stabilisation during the rest of the pulse by surviving the strong field.

Another theory exploits the shift of the energy levels during the atoms exposure to a strong laser field, which can lead to avoided crossings between the levels. For long pulses T. F. Gallagher and colleagues [63] found that the ground state population of potassium atoms would be transferred into Rydberg states, in which they remain after the laser pulse is over. The anticrossings between the Rydberg levels caused by the intense field can be seen in figure 2.9 on the right.

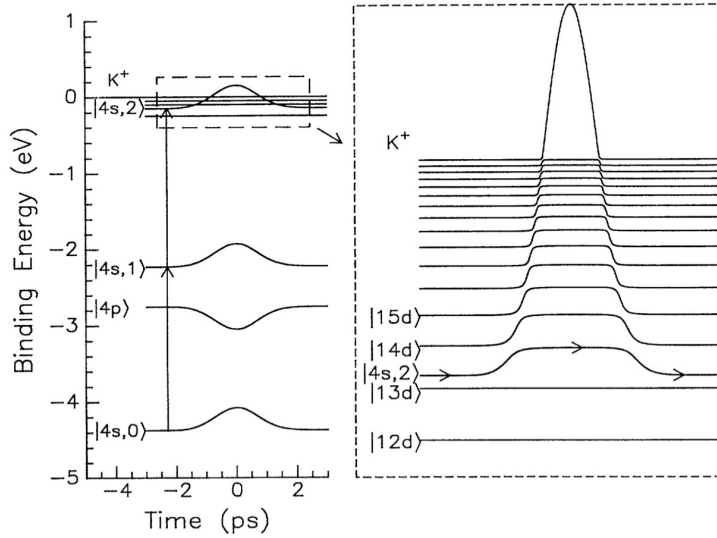


Figure 2.9: Energy levels of the potassium atom during a strong laser pulse from [63]. The population can be transferred from the 2 photon dressed ground state  $|4s, 2\rangle$  to the  $|nd\rangle$  Rydberg series through the anticrossings.

A different descriptive picture of stabilisation is given by the Kramers-Henneberger system [15]. The gauge freedom is utilised again (see equation 2.4 and 2.5) to change into a system where the point of origin follows the movement of an electron in the electromagnetic field. The Hamiltonian of such a system is given by

$$\hat{H} = \frac{\mathbf{p}^2}{2} + V\left(\mathbf{r} - \frac{\mathbf{A}_0}{\omega^2} \cos(\omega t)\right). \quad (2.24)$$

In this system the Coulomb potential of the core oscillates with the frequency of the laser field around the origin of coordinates. The now time dependent potential can be written as a Fourier series

$$V\left(\mathbf{r} - \frac{\mathbf{A}_0}{\omega^2} \cos(\omega t)\right) = V_{KH} + \sum_{n \neq 0} V_n e^{in\omega t}. \quad (2.25)$$

The zeroth order, which represents a time average, is called Kramers-Henneberger potential ( $V_{KH}$ ). The foundation of this theory is given in [15]. Higher orders can be included with perturbation theory.  $V_{KH}$  is a time independent double well potential, in which stationary wave functions during the laser interaction can be formed. The energy levels of the ground level

atoms have to be projected onto these KH-levels during the turn on of the field. M. Gajda *et al.* [64] calculated that these wave functions can then migrate into a bound Rydberg state at the end of the laser pulse. Due to the smooth transitions needed from the undisturbed Coulomb potential to the KH-potential and back, this model is also known as adiabatic stabilisation.

Thorough quantum mechanical calculations confirming excitation in the tunnelling regime were presented by H. G. Muller [65]. Calculations by M. Pont and M. Gavrilin using Floquet-theory also show stabilisation with circular light [66].

Different experimental evidence of Rydberg atoms surviving a high intensity laser pulse support these theories partly [29–32]. However, a very thorough experimental observation of stabilisation of a single prepared Rydberg atom was demonstrated by H. G. Muller and colleagues [33, 34], which excludes interference stabilisation in this special case due to the lack of neighbouring energy levels. Instead the overlap of the electron wave function with the ionic core is minimised to suppress ionisation.

### **Excitation by the frustrated tunnelling model**

The aforementioned three-step model can also be used to give a descriptive explanation for the excitation and survival of neutral atoms in the tunnelling regime. The atoms are not prepared into specific states during the rise time of the short pulse, instead the energy gain during the whole laser pulse is considered. By including the Coulomb force after tunnelling, Rydberg atoms can be formed during the intense short laser pulse. None of the before mentioned stabilisation mechanisms is at work here, instead the process can be seen as the direct excitation of an atom from the ground level into a highly excited Rydberg state by the strong laser field.

Depending on the time of tunnelling of the electron relative to the phase of the electromagnetic field, it will be accelerated away from the core with different strengths, resulting in varying kinetic energy (see figure 2.7 and equation 2.22). Especially when tunnelling at the field maximum, the electron always returns to the core. But also in the direct vicinity of this maximum, the drift energy is still very low, so that the impact the Coulomb field has, after the laser pulse

is over, is still strong. If one includes the Coulomb potential into the before mentioned equation of motion 2.19, the trajectories will change dramatically.

$$\ddot{\mathbf{r}}(t) = \mathbf{e}_1 \frac{-eE_0}{m_e} \cos(\omega t) - \frac{e^2}{4\pi\epsilon_0} \frac{\mathbf{r}(t)}{r^3} \quad (2.26)$$

The laser polarisation is again set along the  $x$ -direction.

Depending on the initial conditions, the electrons, after tunnelling through the barrier, cannot gain enough drift energy to overcome the Coulomb potential, and thus end up remaining inside it with higher energy, leaving the neutral atom in an excited state. This is called frustrated tunnelling ionisation (FTI). It is important to note, that the electron was never actually free during this process, and the atom, therefore, not ionised. The decision, if an ionisation took place, can only be made well after the laser pulse is over. Therefore, the assumption that tunnelling rates are equal to ionisation rates does not hold true. Also it has to be mentioned that, because of the constant drift momentum that is acting on the electron in case of circular polarised light, it would be further away from the core after the laser pulse is over. Due to this, the electron will not be exposed to a strong binding force and no Rydberg atoms are formed, instead the atom gets ionised.

In figure 2.10 the conditions for electrons, which do not leave the Coulomb potential, are plotted dependent on the phase of the laser field at the time of tunnelling, and the perpendicular momentum  $p_y$ , in regard to the tunnelling direction, the electron possesses at the tunnel exit. It is very clear that there actually exists a wide variety of conditions in which a neutral atom survives. Noteworthy is the fact, that the maximum of the laser field, where small drift energies are transferred, which is necessary for the FTI process, is also the area where most electrons will tunnel through the barrier. It follows that the FTI process is a considerable exit channel in the three-step model which has to be taken into account.

A closer look at the trajectories of these bound atoms promises a deeper understanding of the process. Four exemplary trajectories with different starting parameters (indicated in figure 2.10 by a-d) are shown in figure 2.11. They are calculated for times much longer than the laser pulse, which implies that they have performed several revolutions in their final orbits. After the

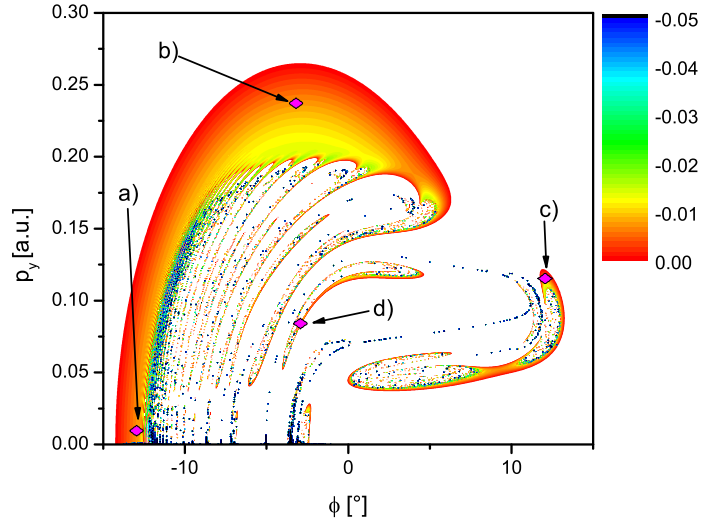


Figure 2.10: Map of electrons which end in an excited state after tunnelling dependent on the laser phase ( $\Phi$ ) and the perpendicular momentum ( $p_y$ ) at the time of tunnelling.

The final total negative energy of the bound electron is colour coded.

a-d indicate initial conditions, for which sample trajectories are shown in figure 2.11.

tunnel exit the quivering motion is clearly visible. More striking is the fact, that in most cases the averaged quivering motion already follows the final orbit. This means that the Coulomb force plays a crucial role directly from the beginning of the process and should not be neglected.

Figure 2.11 a) shows a trajectory, with an electron that tunnels well before the field maximum. As one can see, it gains substantial drift momentum in  $x$ -direction which prevents a recollision with the core at the first return. At the same time the initial perpendicular momentum is very small to allow for a final negative energy, despite the high drift momentum.

The trajectory in figure 2.11 b), in contrast, is produced by the combination of a high perpendicular momentum together with tunnelling close to the field maximum. This time the high initial momentum prevents a recollision with the core in spite of the small drift energy.

Figure 2.11 c) again depicts a high drift energy, which leads to a direction reversal directly after tunnelling. Due to the strong excursion the electron still

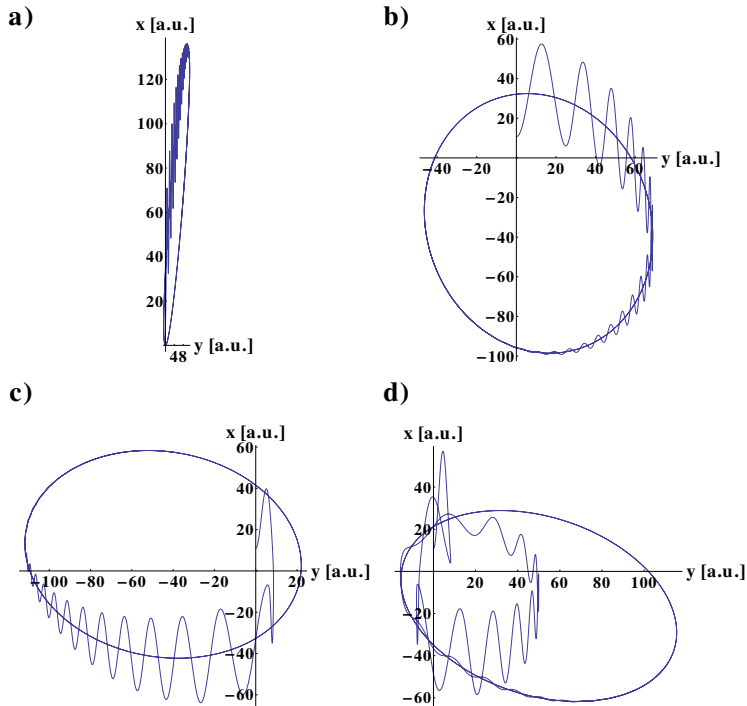


Figure 2.11: Trajectories of FTI electrons for starting parameters indicated in figure 2.10.

misses the core and starts to follow the final orbit very soon.

The speckled area in the middle of figure 2.10 is dominated by chaotic trajectories. Figure 2.11 d) is shown as an example. The close proximity of the electron to the core, at the time when the laser weakens, allows for distinct changes in the orbit, but can still lead to an excited state. As long as rescattering with the core is prevented, and the gained combined drift and initial momentum is small enough, the neutral atom can survive.

If one calculates the principal quantum number  $n$  of these bound atoms, taking the probability of a tunnelling process to be proportional to the ADK tunnelling rates [7], and compares them to quantum mechanical calculations from A. Saenz (see figure 2.12), an excellent agreement between them is apparent. A recently performed experiment confirmed the calculated  $n$ -distribution impressively [67].

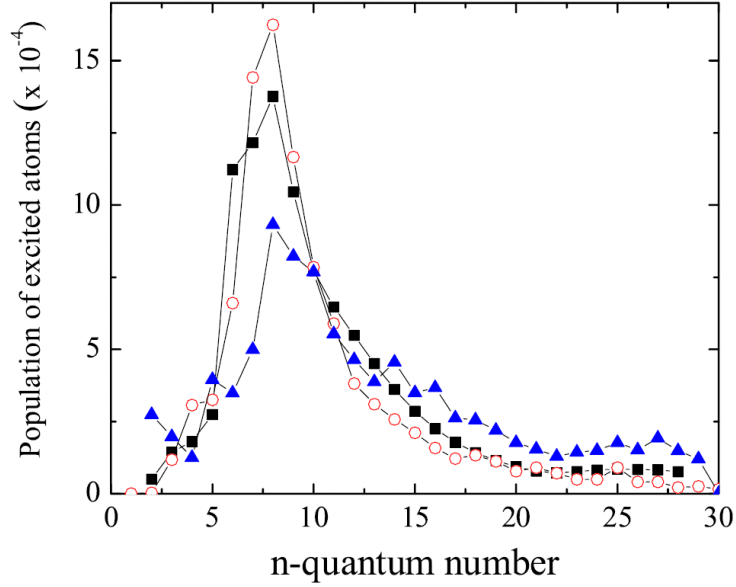


Figure 2.12:  $n$  quantum number distribution from [14].  
 Calculated using Monte-Carlo simulation of classical trajectories (○), quantum mechanical single-active-electron calculation (■) and full two-electron calculation (▲).

## 2.3 Acceleration of excited neutral atoms

Additionally to the survival of neutral atoms in strong laser fields, an acceleration in the focus region has been observed [68]. The reason for this lies in the fact that the electron, while being driven in the laser field, experiences the ponderomotive force. This force is a result of the time-averaged quiver motion inside an inhomogeneous laser field, if one includes the magnetic field component.

Following [69] it is derived by taking the Lorentz force at a given point  $\mathbf{r} = \mathbf{R}_0$

$$\mathbf{F}_L = -q(\mathbf{E} + \dot{\mathbf{r}} \times \mathbf{B}) \quad (2.27)$$

$$\mathbf{F}_L^{(1)} = -q(\mathbf{E}(\mathbf{R}_0) + \mathbf{r}_d \cdot \nabla \mathbf{E}(\mathbf{R}_0) + \dot{\mathbf{r}}_d \times \mathbf{B}(\mathbf{R}_0)) \quad (2.28)$$

and inserting a linear polarised electric field and additionally the displacement current and velocity of a charged particle

$$\mathbf{E} = \mathbf{E}_0 \sin(\omega t), \quad (2.29)$$

$$\mathbf{r}_d = -\frac{q}{m\omega^2} \mathbf{E}_0 (\sin(\omega t) - 1), \quad (2.30)$$

$$\dot{\mathbf{r}}_d = -\frac{q}{m\omega} \mathbf{E}_0 \cos(\omega t). \quad (2.31)$$

By applying  $\nabla \times \mathbf{E} = -\partial_t \mathbf{B}$  one obtains

$$\begin{aligned} \mathbf{F} = & -q\mathbf{E}_0(\mathbf{R}_0) \sin(\omega t) - \frac{q^2}{m\omega^2} \left( \sin^2(\omega t) - \sin(\omega t) \right) (\mathbf{E}_0(\mathbf{R}_0) \cdot \nabla) \mathbf{E}_0(\mathbf{R}_0) \\ & - \frac{q^2}{m\omega^2} \cos^2(\omega t) \mathbf{E}_0(\mathbf{R}_0) \times (\nabla \times \mathbf{E}_0(\mathbf{R}_0)). \end{aligned} \quad (2.32)$$

Averaging over one period of the field simplifies this to

$$\mathbf{F} = -\frac{q^2}{2m\omega^2} \left( (\mathbf{E}_0(\mathbf{R}_0) \cdot \nabla) \mathbf{E}_0(\mathbf{R}_0) + \mathbf{E}_0(\mathbf{R}_0) \times (\nabla \times \mathbf{E}_0(\mathbf{R}_0)) \right). \quad (2.33)$$

And by using the vector relation  $\frac{1}{2} \nabla \mathbf{a}^2 = (\mathbf{a} \cdot \nabla) \mathbf{a} + \mathbf{a} \times (\nabla \times \mathbf{a})$  one ends with the ponderomotive force

$$\mathbf{F}_p = -\frac{q^2}{4m\omega^2} \nabla |\mathbf{E}_0|^2. \quad (2.34)$$

This is the net force on a charged particle with mass  $m$  inside an oscillating field.

To explain the acceleration of a neutral atom, one assumes that the tunnelled electron far from the core as well as the ionic core itself experience this force, while still being bound by the Coulomb force. Because the mass of the ion ( $M$ ) is considerably larger than the electron mass ( $m_e$ ), the ponderomotive force on the ionic core can be neglected and only the force on the electron pulls the whole atom. The final equation for the motion of the neutral atom is given by

$$(M + m_e) \frac{d^2 \mathbf{R}(t)}{dt} = -\frac{e^2}{4m_e \omega^2} \nabla |\mathbf{E}_0|^2. \quad (2.35)$$

For an exact calculation of the force on the neutral atom, one has to look at all forces acting on the ion and electron separately, namely the Coulomb force and the Lorentz force

$$\begin{aligned} M\ddot{\mathbf{R}} &= -e(\mathbf{E}_{Ion} + \mathbf{V} \times \mathbf{B}_{Ion}) + \frac{e^2}{4\pi\epsilon_0} \frac{\mathbf{R} - \mathbf{r}}{|\mathbf{R} - \mathbf{r}|^3} \\ m_e\ddot{\mathbf{r}} &= e(\mathbf{E}_e + \mathbf{v} \times \mathbf{B}_e) + \frac{e^2}{4\pi\epsilon_0} \frac{\mathbf{r} - \mathbf{R}}{|\mathbf{R} - \mathbf{r}|^3}. \end{aligned} \quad (2.36)$$

$M$  and  $\mathbf{R}$  stand for the mass and position vector of the ion,  $m_e$  and  $\mathbf{r}$  for the same in case of the electron.

Such a set of coupled differential equations can only be solved numerically. It yields trajectories in which the electrons end in an excited state, as well as the full acceleration of the bound neutral atom in case of inhomogeneous fields.



## 3 Experimental setup

### 3.1 Detection of neutral atoms

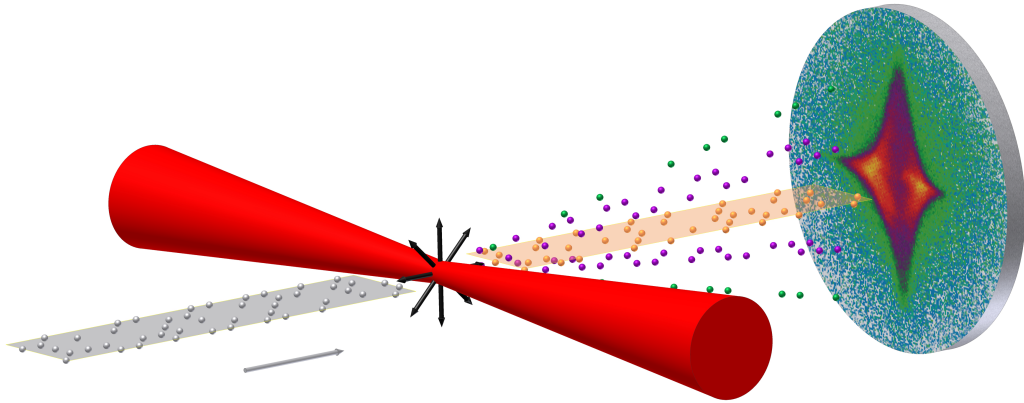


Figure 3.1: Neutral particle detection method.

Grey particles move towards the detector and interact with the laser beam. They can gain different momentum (coloured particles). The position is then detected on a position sensitive detector downstream

The experimental detection of neutral atoms is often done indirectly by ionisation and subsequent detection of the charged fragments, ions and electrons. These can be accelerated with electric and magnetic fields towards a detector, where they lose their kinetic energy and produce a signal. The neutral atoms can also be detected directly, if they carry enough energy. In the case of helium the lowest excited state (the  $^3S_1$  triplet ground state) already carries enough energy to release secondary electrons on the detector surface, which means that all helium atoms in an excited state ( $He^*$ ) can be detected, as they have enough internal energy to produce a signal. This method is well

known and was used to detect neutral metastable atoms (see [70–72]). In contrast to the indirect measurement, where the charged parts are guided by electric fields towards the detector, usually not in line with the gas beam itself, for neutral atom detection the atom beam is directed onto the detector itself. Because of this technique, the atoms from the gas nozzle follow a Maxwell velocity distribution towards the detector, which has to be taken into account during the analysis of the results.

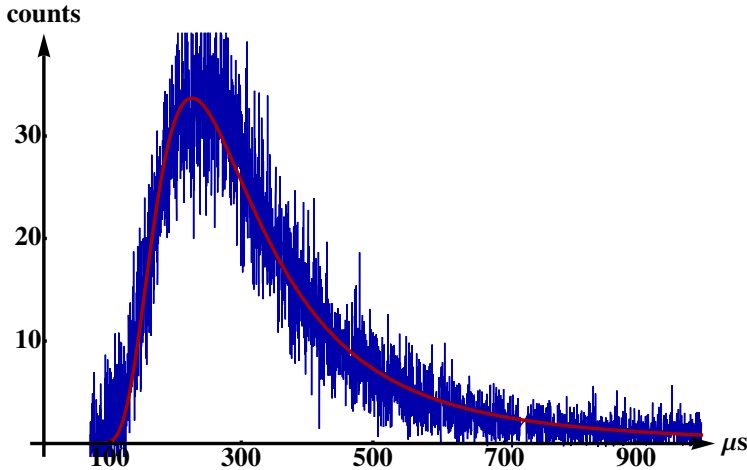


Figure 3.2: Maxwell-Boltzmann distribution of helium atoms moving towards the detector. Measured distribution shown in blue and theoretical fit in red.

The fit in figure 3.2 represents a slightly modified Maxwell distribution, which is given by

$$p(v) = 4\pi v^3 \sqrt{\left(\frac{M}{2\pi kT}\right)^3} e^{-\frac{M(v-v_s)^2}{2kT}}. \quad (3.1)$$

For the atoms inside the gas beam the classical Maxwell-Boltzmann distribution was weighted with the velocity  $v$  and a flow velocity  $v_s$  inside the nozzle is added to obtain equation 3.1 [73]. It is then transferred into a time distribution by the classical velocity relation  $v = s/t$ .  $M$  represents the mass of the helium atoms and  $T$  was set to the lab temperature.

A position sensitive microchannel plate (MCP) configuration DLD80 from RoentDek Handels GmbH was used for detection. A microchannel plate consists of an electrically resistive disc, which has an array of tiny pores ( $25 \mu m$  diameter) running through at a slight angle. By applying a strong electric field from front to back of the plate, any particle hitting the wall inside one of the

pores releases secondary electrons which are then multiplied themselves. The resulting electron cloud exiting at the other side can be easily detected with a simple anode. Because of the high voltage applied to the backside of the MCP, the electron cloud signal has to be decoupled from the anode, which is kept at the same potential, over a high pass filter.

Two standard configurations are known for these detectors, with either high positive or high negative voltage at the front of the stack, to enable detection of electrons or ions respectively. In such a configuration the charged particles, which are measured, are accelerated towards the detector, so they gain additional energy, which is released on impact, to improve detection efficiency. For neutral atoms, however, a custom configuration was used that leaves the front close to ground level and raises the backplate to a high voltage. In this configuration, the detection of charged fragments, which are arriving at the same time as the neutral atoms, is suppressed, as they are not accelerated towards the surface. At the same time, the neutral atom detection is unchanged, which increases the signal-to-noise ratio of the wanted signal.

The DLD80 detector consists of two microchannel plates back to back in chevron configuration and offers an active detection area of  $50 \text{ cm}^2$ , as well as a two dimensional delay-line configuration, which enables one to retrieve the point of impact of the impinging particles. This is accomplished by adding a grid of two wires behind the plates. Both are routed in many parallel passes over the full plate in a zig-zag fashion. The two wires are perpendicular to each other to allow for the two dimensional reconstruction of the point of impact. The amplified electron cloud passing through these wires creates a short electric pulse that travels along both wires. At the four independent ends of these two wires the electrical pulses from the electron cloud can be recorded. Together with their timing to each other, they can be converted into the point of impact of the single particle on the microchannel plate. If no signal is observed on one of the four lines the reconstruction fails and an invalid event is recorded, which has to be removed from the result.

The signals from the MCP are taken from the RoentDek DLA-TR6 control unit, which separates the pulses from the high voltage the MCP is kept on. Additionally, a first amplification is performed to minimise signal loss on the way to the subsequent analysis. To keep the timings correct, exactly

matched cables are used for all channels throughout the signal chain. The raw signals are then fed to an Agilent Technologies (now Keysight) U1051A Acqiris TC890 six-channel time-to-digital converter inside a U1056B Acqiris Data Acquisition System. This unit can acquire timing information for pulses above an adjustable threshold for up to 6 individual channels with a precision of 50 ps with respect to a common start signal. The start and stop times of the MCP signals above the threshold are analysed and an exact timing, similar to a constant fraction discriminator, is extracted. These details make it ideal for acquiring the timing information of the MCP delay lines to reconstruct the point of impact. The start signal was provided by a fast photo diode pointing at a diffuse laser reflex, whose signal was first amplified and then processed by a constant fraction discriminator. The extracted timing information of all four channels is transferred to a PC, where it is analysed with software written within the group by K. Gorling. In the case of a valid signal on all four channels during a set time interval, an event with individual time and position is generated, which can be exported.

## 3.2 Vacuum setup

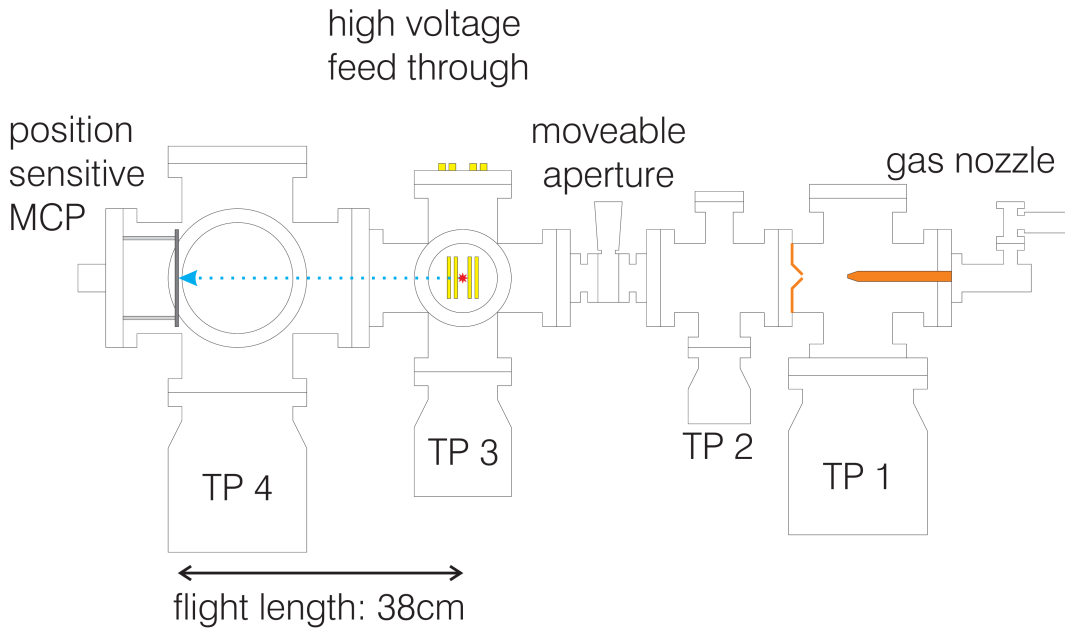


Figure 3.3: Sketch of the vacuum chamber setup used

All experiments were performed inside an ultra-high vacuum chamber (see figure 3.3). It is build in the ConFlat (CF) standard and includes three differential pump stages, which are all evacuated by turbomolecular pumps from Pfeiffer Vacuum and Varian (now Agilent) with varying sizes (TP1 to TP4). The gas load produced by these is pumped by either a Scroll pump from Varian or Oerlikon. The pressure of the test gas inside the boron nitride gas nozzle can be adjusted over a precise dosing valve to adjust the amount of atoms inside the interaction volume. If the pressure is too high, too many atoms hit the detector and their timings cannot be assigned correctly, if it is too low on the other hand, measurement times become too long to keep stable conditions of the laser system. The gas leaves the nozzle through a  $200\ \mu\text{m}$  opening and forms an effusive gas jet. This jet is then restricted by the skimmer, which allows only the central part to enter the next differential pump stage. This ensures that the initial lateral momentum of the atoms in the interaction area is sufficiently small. The first pump stage is evacuated by TP1. After the second stage a moveable aperture is installed, which can either restrict the gas beam even further and lower the background pressure in the

final chamber, or be left open to achieve a greater amount of atoms in the interaction area.

The laser beam enters the chamber through one or two BK7 windows, one on each side. To suppress charged particles in the measurement, four metal rods are installed around the interaction area. They are connected to a high voltage feedthrough and can produce a variable desired electric field to push ions and electrons inside the atomic beam to the side, so that they miss the detector at the end of the drift zone. The differential pump design allows for a very low background pressure of  $10^{-9}$  mbar in the interaction area while still providing a sufficiently high flux of gas atoms.

### 3.3 Laser system

The laser which was used for all experiments is a commercial Titanium-Sapphire (Ti:Sa) system from Spectra Physics (now Newport Corporation) including a Tsunami Oscillator, optically pumped by a Millennia laser, and an upgraded Spitfire Pro amplifier, pumped by an Empower Q-switch laser. The system produces pulses of 40 fs length, 3 mJ pulse energy at 800 nm central wavelength with a repetition rate of 1 kHz.

The laser system can produce these pulses by employing the chirped-pulse amplification method, which allowed a significant step forward in the peak intensities feasible with a single laser. In the first step the oscillator produces short pulses with low energy ( $nJ$  range) at a high repetition rate. A continuous wave pump laser is pumping a Ti:Sa crystal inside a free running resonator, whose design is optimised towards short pulse production. The use of apertures and nonlinear optical elements allows a mode-locking process where short pulses with a length of  $\approx 35$  fs are produced. Additionally, an acousto-optic modulator can be switched on to support the initial mode-locking process, but was always switched off during measurements. The repetition rate of  $\approx 80$  MHz is purely determined by the length of the resonator.

These pulses are then stretched several orders of magnitude in time by passing over an optical grating twice. The first pass introduces a wavelength dependent spread of the pulse into different angles. By careful guidance inside the

stretcher this spread is converted into a length difference of the optical pathway for different wavelengths. Because of that, the different parts of the pulses spectrum arrive at different times when they pass over the grating for the second time. This wavelength shift over the length of the pulse is called a chirp. The grating then reverses the spatial spread so that the whole pulse is reflected into one single angle, but elongated in time. These longer chirped pulses can then be safely amplified inside a pumped Ti:Sa rod because their intensity is lowered below the damage threshold of the laser medium. The repetition rate of the ultrashort pulses is limited by the the Q-switched pump laser inside the amplifier which has to dump the energy inside the active medium before each pulse. Thus, for these high pulse energies the repetition rate of the laser system has to be dropped to e.g.  $1\text{ kHz}$  compared to the  $\text{MHz}$  repetition rate of the oscillator. After amplification, these high energy pulses can be compressed in time close to their original length by sending them over an optical grating again. The wavelength dependent reflection is used again to produce a different length of passageway for each wavelength inside the compressor. By using matched gratings and lengths inside stretcher and compressor, it is possible to reverse the chirp introduced to the pulse before amplification, and end with a high energy pulse where all wavelength are synchronous in time. This parameter can be checked with a SPIDER (spectral phase interferometry for direct electric field reconstruction [74]), which can display the spectral phase over the pulse. In case of an equal phase over the full lengths an ideal compression is achieved.

The laser system only runs sufficiently stable if it is used with a fixed set of energy parameters for the pump lasers and amplification crystals. The experiment on the other hand demands for adjustable pulse energies. Therefore, the beam energy was adjusted after the laser system. This was accomplished by a zero-order (later achromatic) waveplate and two subsequent thin film polarisers with high extinction ratio along the beam path. By changing the rotation of the waveplate the energy percentage which is reflected by the polarisers and reaches the experiment can be adjusted. The residual energy is dumped in optical traps.

For the research in this thesis the laser was mainly used for two different setups, which will be described briefly in the following sections.

### 3.4 Two pulse setup

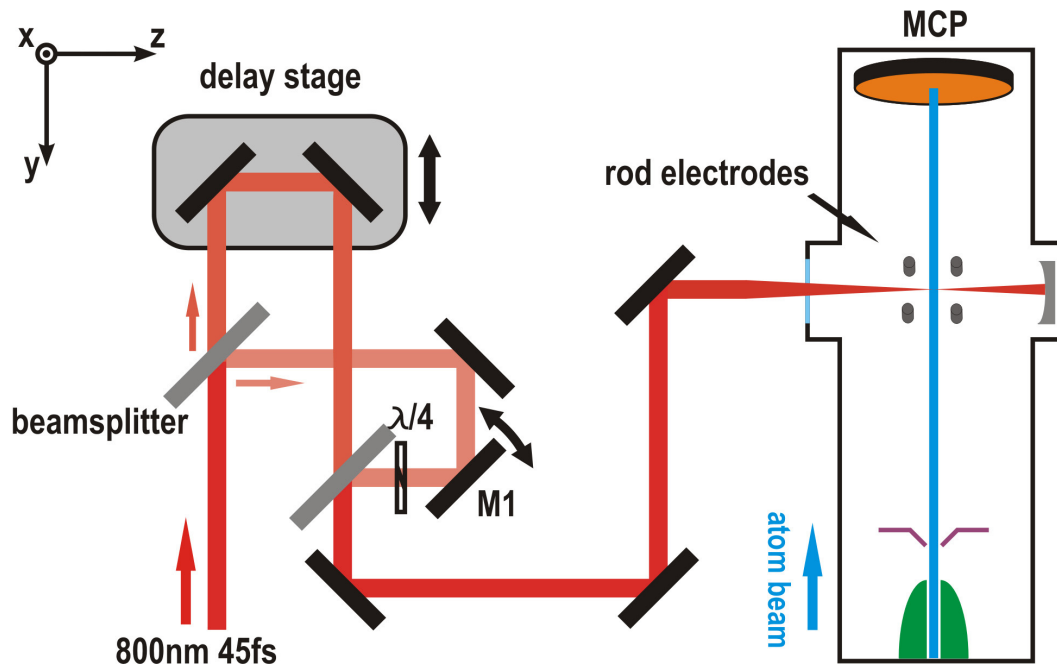


Figure 3.4: Drawing of the setup used to measure the steering of neutral atoms

To test the stability and properties of the aforementioned Rydberg atoms after laser interaction, a modified laser beam scheme was used. A schematic diagram is shown in figure 3.4. After attenuation, the laser enters a Mach-Zehnder interferometer, where it is split into two equally strong parts by a beam splitter. These two parts take a different path to a second beam splitter, where they are overlapped again. One part is guided over a delay stage with a high precision motor stage by Aerotech Inc., which allows changing of the arms length with  $nm$  resolution, while the other arm has a fixed length but can accommodate additional optics. This setup is first presented in [75]. A perfect overlap of the two beam parts inside the vacuum chamber was established. By changing the position of the delay stage in one arm, one of the two pulses can be retarded. But the foci of the two subsequent pulses after the focussing mirror are still exactly at the same position in space.

By introducing a quarter wave plate in one arm a consecutive interaction with an elliptically polarised beam directly after the initial interaction with linear light can be realised. Because of the relatively slow speed of the thermal atoms

in the gas beam, compared to the speed of light, they do not drift away and the second beam interacts with the same atoms that were excited by the first beam moments before.

Half of the total laser energy is lost in such an interferometer setup, as it ends up in the other possible path behind the second beam splitter. In the interferometric case of full overlap, one can adjust where the laser beam exits the beam splitter, in the temporally separated case, however, exactly half is going in each direction. Because of this, tight focussing is needed to still reach the desired intensities in the focus area. This is realised by using a fully adjustable concave silver mirror with a short focal distance of 15 *cm* inside the vacuum chamber.

By performing very slight adjustments to mirror *M1* (see figure 3.4) the overlap of the two beams is intentionally varied, which allows for a shift in space of only one of the two foci. In this case the focus spot of the elliptically polarised beam can be shifted in space, with respect to the linear beam passing through the unaltered arm. Thus a selective interaction with respect to the two beams can be realised, where the atoms produced by the first beam see a different intensity of the second beam depending on their point in space.

### 3.5 Standing wave setup

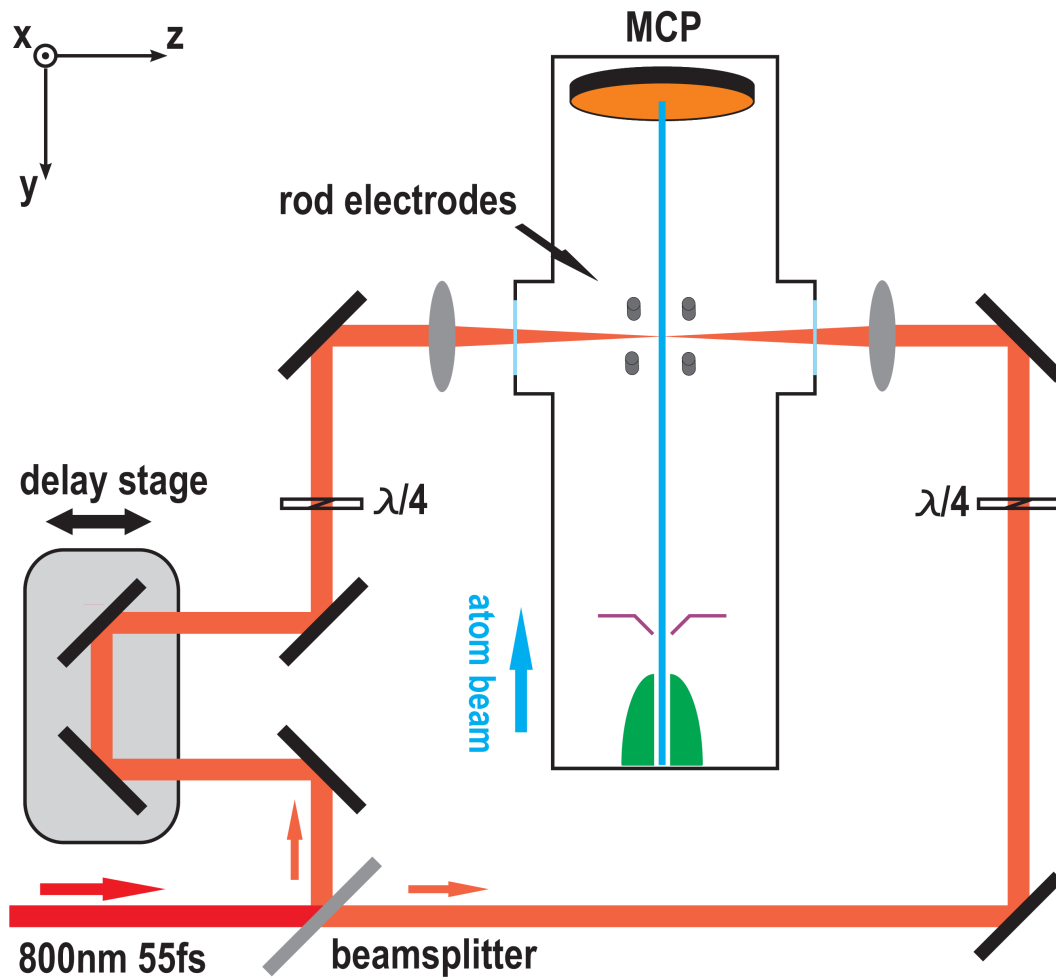


Figure 3.5: Sketch of the standing wave setup

To realise a standing wave, two pulses propagating in opposite direction are needed. A sketch of this setup is shown in figure 3.5. The attenuated beam is split into two arms with a beam splitter as well. Both arms are then steered into opposing windows of the vacuum chamber. An equal length is sustained by building a detour into the shorter arm, which also includes a motorised delay stage to finely adapt its length towards equality with the second arm. Substantial effort is made to ensure a maximum stability for both laser arms. This includes a full decoupling of all optical elements from the vacuum chamber to suppress any unwanted vibrations from the vacuum pumps, while maintaining maximum adjustability. Both laser arms are fully

overlapping over the complete optical pathway after the beam splitter, which results in a clear interferometric picture visible behind the beam splitter, independent of the lengths of both arms.

Identical lenses are used for both beams and their distance is chosen so that the focal planes are equal. The delay stage in one arm directly changes the point of overlap for the two beams along the beam path, so that, in conjunction with the spatial freedom of each arm on its own, one can adjust the overlap region fully in space and time. To ensure a very good overlap in time, both beams individually are producing a plasma in air at atmospheric pressure which can be observed. In case of an overlap in time an increase in signal strength at one point in the beam path can be monitored. It represents the length along the beam path where the two counter-propagating pulses overlap. By adjusting the length of the arm which includes the delay stage, this overlap region can be shifted along the laser axis to the common focal spot of both beams.

Both arms also employ an achromatic quarter wave plate by B.Halle Nachfl. GmbH to change the ellipticity of each arm individually. Due to the possibility of very fine displacements caused by a non perpendicular mounting of the optics, special attention has been given to the inclusion of these, to maintain the full standing wave overlap in the focus region, independently of the rotation of both wave plates.

## **3.6 Beam characterisation**

The intensity of the laser beam can be calculated from the energy, the pulse length and the focus spot size. For the energy measurements two QE25SP-S-MT-D0 detector heads together with a MAESTRO and a UNO monitor from Gentec EO were used. They comprise a fast response pyroelectric sensor, which transforms the heat changes, which are triggered by the laser pulses hitting its surface, into an electric pulse. With proper calibration curves these signals can be converted into precise energy readings for the pulses used in the experiment. Additionally a Newport 407A power meter with a thermopile sensor was used, which gives a voltage proportional to the temperature of its detector surface.

For pulse length measurement an early production SPIDER from APE and the FEMTOMETER autocorrelator from Femtolasers were used. Both retrieve the pulse length by overlapping two copies of the pulse inside a nonlinear crystal and measuring the resulting interferometric intensity with a detector. In the SPIDER one of the two pulses is additionally chirped by guiding it over a grating, to retrieve additional information about the spectral phase compared to the autocorrelator.

While energy and pulse length were determined using these detectors, the focus size was determined with the knife-edge method. It utilises the decreasing energy a laser beam deploys on a detector if part of it is covered. The intensity of a Gaussian beam is given by

$$I(x, y) = I_0 e^{-\frac{2x^2}{w_x^2}} \cdot e^{-\frac{2y^2}{w_y^2}}. \quad (3.2)$$

To calculate the total energy  $E_{total}$   $I(x, y)$  has to be integrated. The residual energy of a Gaussian beam that is partly blocked by a linear obstacle up to  $x$  is given by

$$E(X) = E_{total} - I_0 \int_{-\infty}^X e^{-\frac{2x^2}{w_x^2}} dx \int_{-\infty}^{\infty} e^{-\frac{2y^2}{w_y^2}} dy \quad (3.3)$$

$$= \frac{E_{total}}{2} - \sqrt{\frac{\pi}{2}} I_0 w_y \int_0^X e^{-\frac{2x^2}{w_x^2}} dx. \quad (3.4)$$

With the substitution

$$z^2 = \frac{2x^2}{w_x^2} \quad (3.5)$$

$$dx = \frac{w_x dz}{\sqrt{2}} \quad (3.6)$$

one yields

$$E(X) = \frac{E_{total}}{2} \left[ 1 - \operatorname{erf} \left( \frac{\sqrt{2}X}{w_x} \right) \right]. \quad (3.7)$$

Using this formula, the width of the beam in the  $x$ -axis can be measured by measuring the residual energy that reaches an energy detector, while slowly moving a blade into the beam profile and thereby blocking part of the beam. This was done by including a small mirror between lens and vacuum chamber to direct the laser beam towards the measuring apparatus. This method alone

would already yield the spot size if measured exactly in the focus. Since the knife has to be moved with very high precision and the signal directly at the focus changes on a very short length, several measurements around the focus area have been performed instead. These can be combined into a single graph which reveals the width progression along the laser propagation axis. Shown here is the measurement performed for the standing wave setup.

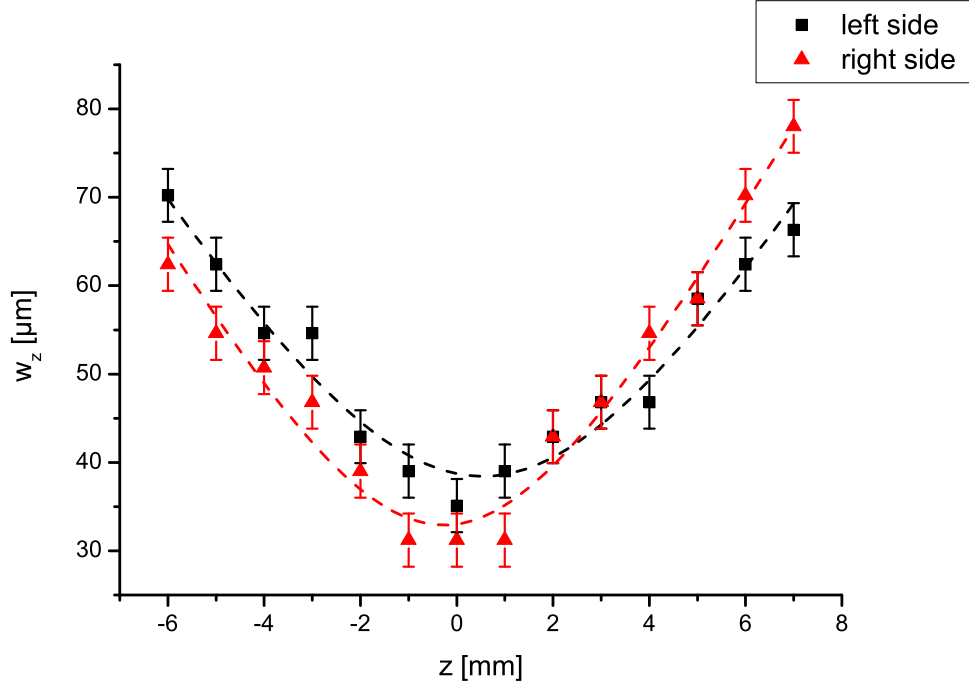


Figure 3.6: Width of the laser beams along the focus measured with the knife edge method. The dotted curves represent the fit to equation 3.8 for each beam.

This result is then fitted to the width of a Gaussian beam in the focus area given by

$$w(z) = w_0 \sqrt{1 + \left(\frac{z}{z_R}\right)^2}, \quad (3.8)$$

where  $z_R = \pi w_0^2 / \lambda$  is the Rayleigh length, to extract the minimal beam waist  $w_0$ .

Using this method, the two foci were measured to be  $38 \mu m$  for one arm and  $33 \mu m$  for the other (see figure 3.6).



## **4 Two pulse excitation and acceleration**

The focus of this thesis lies in the interaction of neutral atoms with high intensity laser fields. The final product of the frustrated tunnelling process, as introduced in section 2.2, consists of a neutral atom in a high excited state (Rydberg atom). A more detailed introduction of this model, as well as the fundamental theory concerning the acceleration, that was observed in conjunction with it, can also be found in [69]. The first experiment performed in the extent of this thesis was designed to expose the Rydberg atoms to another strong laser field and observe their stability. Additionally, the acceleration acting on the atoms is measured and used as an indicator for the field strength the Rydberg atoms interacted with.

### **4.1 Exposing neutral Rydberg atoms to a strong laser field**

Shortly after a first intense laser pulse which produced the excited Rydberg atoms is gone, a second pulse is applied to these atoms. To ensure that the observed atoms actually interacted with both beams, a modification has been introduced. As stated in section 2.1, the FTI-process is only possible for linear polarised light. Thus an elliptically polarised beam does not excite new stable Rydberg atoms itself, and all Rydberg atoms that are detected after both pulses stem from the excitation of the first pulse.

Since the speed of the atoms is mainly determined by the thermal energy of the beam source, which is kept at room temperature, the time they need to pass

through the interaction area is long compared to the delay between the two subsequent pulses. This means that the atoms can be considered stationary for a short enough time delay between the pulses. Therefore, the atoms produced by the first beam will still be in the focus area of the second elliptical beam and will experience the full field.

The acceleration that one observes with a single laser pulse, as explained in section 2.3, is acting due to the gradient of the field. Because of that, a pulse with elliptical polarisation should also add additional momentum onto the Rydberg atoms, as long as the atoms themselves are not ionised by it.

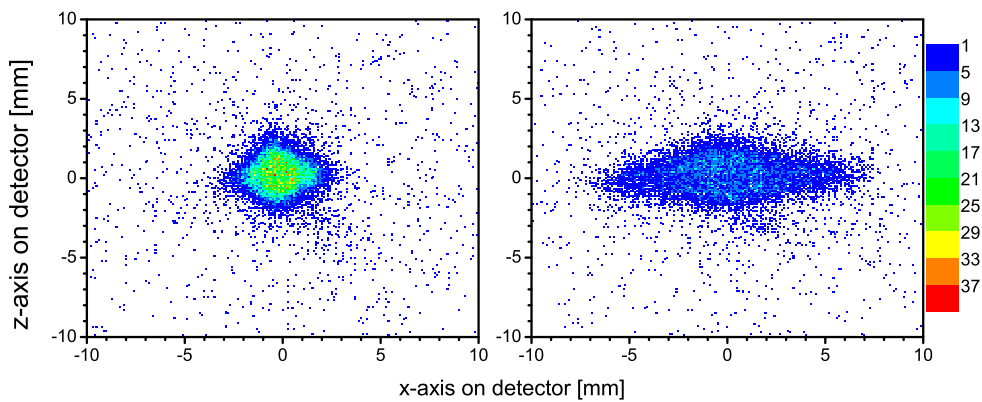


Figure 4.1: Additional acceleration imparted on Rydberg atoms. Acceleration by the first pulse alone on the left side, double pulse acceleration by both subsequent pulses on the right. The laser beam is aligned along the  $z$ -axis while the observed acceleration can be seen in  $x$  direction.

Exactly this momentum increase is observed in the experiment (see figure 4.1). The measurements shown represent a projection of the focus area onto the MCP surface area. Atoms excited by the laser keep their initial momentum towards the detector and can gain additional momentum perpendicular to the laser beam, which is small compared to the thermal velocity. Therefore, only the changed momentum perpendicular to both, the laser axis ( $z$ -axis), as well as the travel direction ( $y$ -axis), is registered as deflection ( $x$ -axis).

The laser travels along the  $z$ -axis, which means that the length of the projection in this direction represents the length of the focus area where the intensity is high enough to excite neutral atoms. One has to keep in mind, that this

length is elongated by the divergence of the atomic beam in the subsequent flight time. The length in the  $x$ -axis represents the projected acceleration that is imparted on the atoms in the focus area. In contrast to the laser axis this is hardly elongated, as all atoms arriving at the detector stem from the few  $\mu\text{m}$  wide focus. In conjunction with the flight time this axis can directly be converted into a velocity imparted onto the neutral atoms during the short time of interaction.

The distribution with the second laser pulse applied is a lot broader than the one on the left, which stems from just a single linear laser pulse. The atoms on the extreme ends of the  $x$ -axis can only be deflected that far if they acquire energy from both pulses. The full intensity the atoms have interacted with is, therefore, encoded in the position on the detector. These far deviated atoms thus directly prove that the neutral atoms do survive the second pulse. Summing over all detected atoms from these two measurements reveals that 73% of Rydberg atoms survive the second pulse in this example. It is important to note that no signal at all can be seen if only the second elliptical pulse is applied, which means that all atoms detected on the MCP are initially excited by the first linear polarised laser pulse. A detailed analysis of several Rydberg survival rates, measured for different pulse energies, can be found in [76], including quantum mechanical calculations with a good agreement with the experiment. The interference stabilisation presented in section 2.2 can be utilised to explain the stability observed in Rydberg atoms [25]. Recent calculations using the Magnus expansion also showed a very good agreement between the measured and calculated survival rate [77]. In contrast to the calculations by A. Saenz from [76], non-dipole effects are identified to be the main influence for ionisation during the second pulse in this paper.

## 4.2 Classical trajectory calculation with two pulses

The field amplitude of the electric component of the laser field is higher than  $1 \text{ GV/cm}$ , which exceeds the threshold for static field ionisation by more than 6 orders of magnitude. Atoms still surviving this field can only be explained by looking at the dynamics of the charged particles in the oscillating field. A simplified picture can already give reasonable explanation for this

behaviour. The classical Newton equation with dipole approximation was solved in Coulomb gauge (see page 6) for the active electron in vicinity of the ionic core (see equation 2.26), only this time two laser pulses are included. The first linearly polarised, the second one circularly polarised.

$$\ddot{\mathbf{r}}(t) = \frac{e}{m_e} \begin{pmatrix} E_0 e^{\frac{t^2}{\sigma^2}} \cos(\omega t) + \frac{E_0^*}{\sqrt{2}} e^{\frac{(t-t^*)^2}{\sigma^2}} \cos(\omega t) \\ \frac{E_0^*}{\sqrt{2}} e^{\frac{(t-t^*)^2}{\sigma^2}} \sin(\omega t) \\ 0 \end{pmatrix} - \frac{e^2}{4\pi\epsilon_0} \frac{\mathbf{r}(t)}{r^3} \quad (4.1)$$

All calculations have been performed with Mathematica 8 by Wolfram Research Inc. using the included NDSolve algorithm. Starting parameters are chosen from the coloured region of figure 2.10.

Figures 4.2 to 4.4 show the trajectories of the tunnelled electron in three special cases.

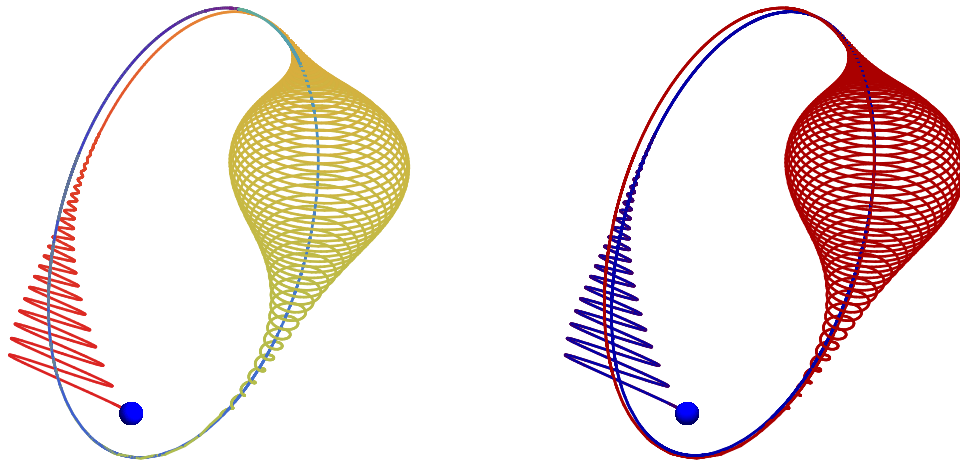


Figure 4.2: Trajectories for double pulse experiment part 1.

Left side: the time evolution is pictured in colour from red (early) to blue (late)

Right side: the full evolution with the same starting conditions for a single pulse (blue) and the double pulse (red)

In figure 4.2 one can clearly see that the second pulse acts during a time, when the electron is far from the core region. Thus it acts on a "quasi free" electron

and the two trajectories before and after the second interaction are nearly identical (blue and red in the right figure). The energy of the excited Rydberg atom remains almost unchanged. Since for Rydberg atoms in general the electron spends a majority of its time far away from the core, this behaviour is to be expected for many of the excited atoms, as the second pulse statistically hits with a high probability during this "quasi free" time.

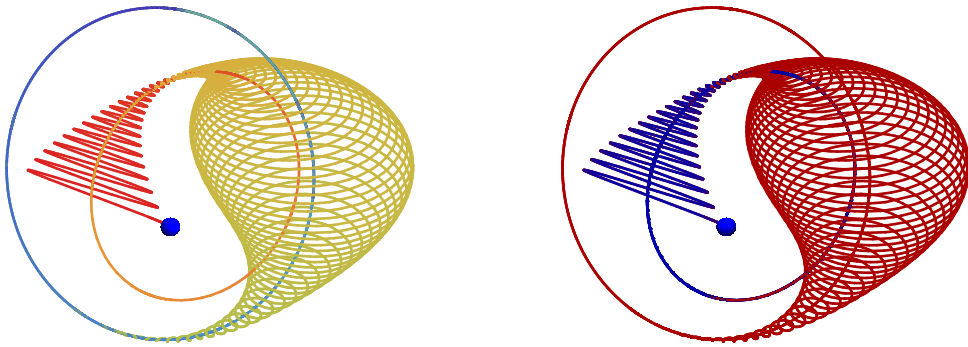


Figure 4.3: Trajectories for double pulse experiment part 2.

Left side: the time evolution is pictured in colour from red (early) to blue (late)

Right side: the full evolution with the same starting conditions for a single pulse (blue) and the double pulse (red)

However, the situation changes when the electron is closer to the core during the interaction with the second pulse. Now momentum can be transferred and the path of the electron is changed. The vicinity of the electron to the core is thereby a good indicator of the influence the second pulse has on the energy state of the Rydberg atom. In the second example the additional pulse hits the atom shortly after the first completed round-trip of the electron in its Rydberg orbit. As can be seen in figure 4.3 the second pulse drives the electron nearer to the core and a change of trajectory, in this case towards a higher excited state, is possible. Without the second pulse the electron remains in the smaller blue orbit. The plane in space, in which the motion takes place, is unchanged though.

In contrast, if the second laser pulse drives the electron into the direct vicinity of the core, ionisation is very likely and the Rydberg atom will be lost. If an ionisation does not occur then the trajectory of the electron is still dramatically changed, as can be seen in figure 4.4. Here, the initial and the final orbit are distinctly different from each other because the electron can gain noticeable angular momentum while being driven violently around the ionic core.

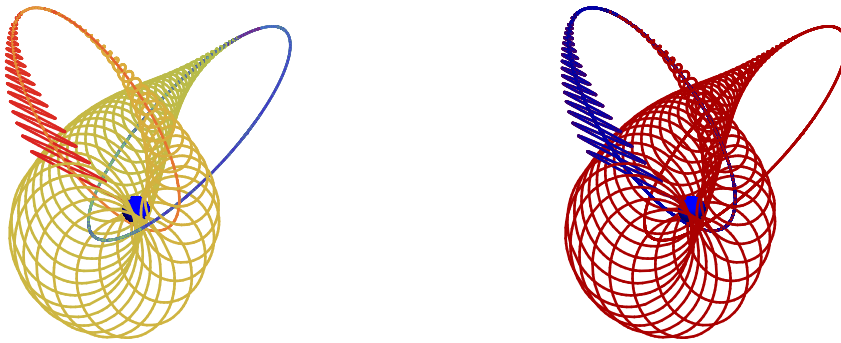


Figure 4.4: Trajectories for double pulse experiment part 3.  
 Left side: the time evolution is pictured in colour from red (early) to blue (late)  
 Right side: the full evolution with the same starting conditions for a single pulse (blue) and the double pulse (red)

For closer inspection an ensemble calculation of these atoms was performed. The starting position was given by the tunnel exit in  $x$ -direction. The phase of the electric field was randomised over one oscillation at the maximum of the pulse. One can have a look at the principal quantum number distribution calculated from these Rydberg orbits. It is obtained by using the classical Rydberg energy level structure, which, while not exact for helium, should produce very similar results for higher excited states.

$$E = -\frac{13.6eV}{n^2} \quad (4.2)$$

The electrons which are found with negative energies long after the laser pulse is over, are converted into their corresponding principle quantum numbers, after which they are sorted into bins to obtain a histogram.

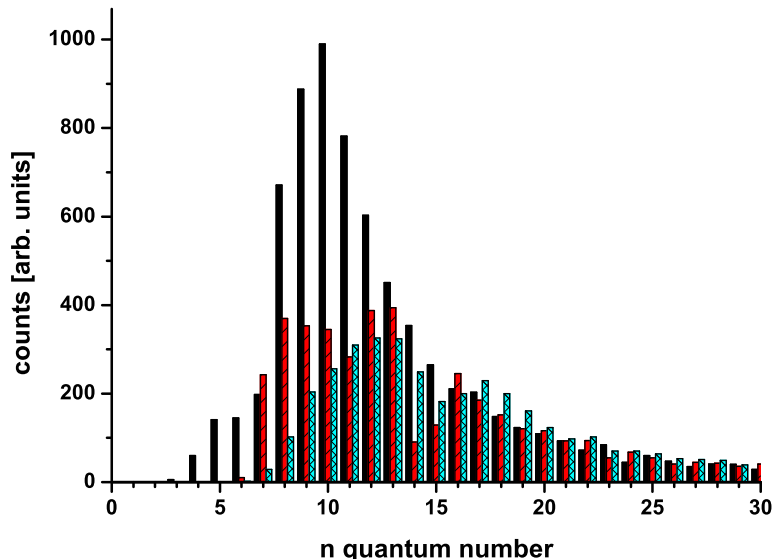


Figure 4.5:  $n$ -distribution of He atoms after strong-field interaction.

Black bars: First linearly polarised laser pulse alone (laser intensity  $I = 10^{15} \text{ W/cm}^2$ ).

Red bars (striped): Additionally, a second circularly polarised laser pulse is applied after 500 fs ( $I = 2 \cdot 10^{15} \text{ W/cm}^2$ ).

Blue bars (crossed): As before, but the second laser intensity  $I = 2.8 \cdot 10^{17} \text{ W/cm}^2$ .

Figure 4.5 shows this principal quantum number  $n$  histogram for three different calculations. The black bars represent the distribution produced by a single linearly polarised laser pulse with an intensity of  $10^{15} \text{ W/cm}^2$  and a laser pulse duration of 45 fs (FWHM). Only atoms tunnelling around the field cycle maximum at the peak of the pulse envelope are considered. A shorter pulse length or later tunnelling would result in a slightly shifted distribution, as these electrons would gain less drift energy in the laser field. The red bars represent the atoms which survive a second circularly polarised laser pulse with an intensity of  $2 \cdot 10^{15} \text{ W/cm}^2$  applied 500 fs after the first one. Its field strength is the same as the linearly polarised first pulse. In the blue results

a second pulse with considerable higher laser intensity of  $2.8 \cdot 10^{17} \text{ W/cm}^2$  was used. The survival percentages extracted from these calculations are 61% and 56% respectively.

The most striking finding from these calculations is the fact, that the difference between the moderate second pulse and a very strong one is not very prominent. Also there is a lower  $n$  limit below which no atom survives the second pulse. Looking at the Kepler orbit times of these states  $T_{\text{orb}} = 2\pi n^3$  (for  $n = 5 \implies T_{\text{orb}} = 19 \text{ fs}$ ), one finds that these are shorter than the laser pulse itself, which means that the electron returns to the core during the interaction with the second laser pulse and scattering on it will lead to ionisation. For states with  $7 < n < 15$ , corresponding to Kepler orbit times  $52 \text{ fs} < T_{\text{orb}} < 5.1 \text{ ps}$ , the count rate is roughly reduced by half. Here the strong laser pulse depletes states with  $n < 10$  slightly more than the moderate laser pulse.  $n = 7$  is an interesting exception, where for the low intensity pulse the population after the second pulse is actually higher than before. The Kepler orbit time of this state is around the same as the laser pulse duration, which shows that a small redistribution of some  $n$ -states takes place during the second pulse. For states with  $n > 15$  the distribution is mainly the same in all three cases. One can deduce, that for Kepler orbit times much larger than the laser pulse itself, the atoms are almost unaffected by the second pulse. However, it has to be noted that ionisation in the focus region due to the intensity gradient present during focussing is not considered in this calculation, but should affect the survival rate for such a high intensity as applied in the calculation shown in green [78]. The observation of a reduced ionisation rate is in accord with theoretical predictions made for ionisation of Rydberg states at lower intensities [23].

In figure 4.6 the survival probability of every principal quantum number  $n$  after the second laser pulse is plotted. In 4.6 a) different ellipticities are used. It is revealed that the ellipticity dependence is mostly present up to  $n = 10$ . For these lower states the higher ellipticity hinders the electron to approach the core too closely and thus prohibits ionisation. For higher states the survivability slowly approaches unity for all ellipticities. The only exception is given by  $n = 15$  where a clear dip is visible in each curve. For  $n = 15$  the round-trip time matches the delay of  $500 \text{ fs}$  so that the electron

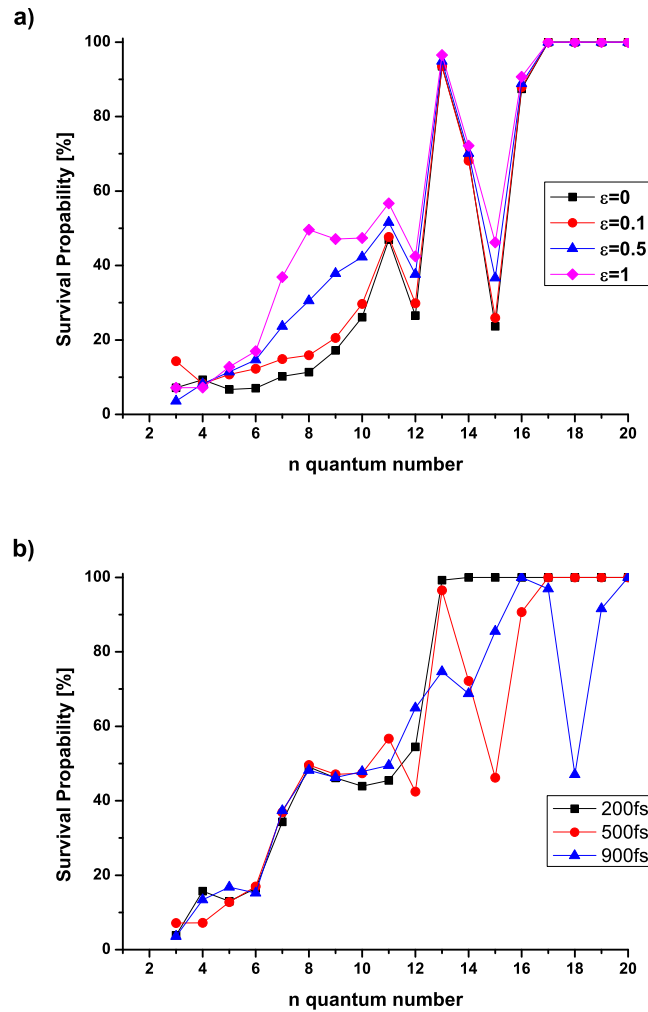


Figure 4.6:  $n$  selective survival probability of He Rydberg atoms exposed to a polarised laser pulse.

a) for different ellipticity and a time delay of 500  $fs$ .

b) for circularly polarised pulses at different time delays.

is again close to the core at the time when the second pulse hits the atom. In figure 4.6 b) one can see how the position of the dip changes for different delays. For a delay of 900  $fs$  the dip is visible at  $n = 18$  which corresponds exactly to the Kepler orbit time of this state. In the 200  $fs$  case the decrease is not that obvious but can also be seen around  $n = 10-11$ , which again corresponds to its round-trip time. For higher principal quantum numbers the atom always survives the second pulse. This can be explained by the

fact that the tunnelled electron never returns to the core region before and during the time the second pulse hits the atom. Thus their trajectories are only determined by the interaction with the first pulse in conjunction with the Coulomb potential.

### 4.3 Steering of neutral atoms with strong fields

To exploit the observed stability a new experiment was conceived. The focus spot of the second laser was moved in space with regard to the first one.

To understand the observed figures one has to recall the acceleration explained before. Neglecting the electrons mass compared to the total mass of the atom  $M + m_e \approx M$ , equation 2.35 can be reduced to

$$\frac{d^2\mathbf{R}(t)}{dt} = -\frac{e^2}{4Mm_e\omega^2}\nabla|\mathbf{E}_0|^2. \quad (4.3)$$

Together with the intensity distribution of a Gaussian laser beam in the focus

$$I(\mathbf{r}) = I_0 \left(1 + \left(\frac{z}{z_0}\right)^2\right)^{-1} \exp\left(-\frac{2r^2}{r_0^2}\right), \quad (4.4)$$

where  $r_0 = w_0\sqrt{1 + (\frac{z}{z_0})^2}$ , with the beam waist  $w_0$  and the laser intensity  $I_0$ , one can obtain the radial component  $r_c$  of motion, which is perpendicular to the laser axis

$$\ddot{r}_c(t) = \frac{I(\mathbf{R})}{M\omega^2} \frac{r_c(t)}{r_0^2} \exp(-t^2/\tau^2). \quad (4.5)$$

A Gaussian laser pulse envelope with a pulse length of  $\tau$  is assumed. The radial component has to be used because the measurement method projects the acceleration, which is present in all directions perpendicular to the laser axis, onto the detector in the  $x$ - $z$ -plane. Equation 4.5 yields the acceleration by a short laser pulse which causes a deflection of the atoms. This deflection can be observed on the detector.

Assuming that the ion does not move during the laser pulse, the time dependence of  $r_c(t)$  can be neglected and the equation can be solved by mere integration over the pulse envelope. It is important to note, that, since the electron tunnels around the maximum of the pulse, only the second half of

the pulse has to be taken into account when integrating to obtain the correct imparted momentum. When the second pulse is applied, however, the full envelope has to be used, because the "quasi free" electron is interacting with this field the entire time.

A full Monte-Carlo simulation of the expected particle distribution on the detector was performed. All trajectories start inside the focal volume of the first pulse and their amount is weighted by the tunnelling ionisation rate (ADK-rate, see [7] and [79]), which depends on the local field strength. It is assumed that the Rydberg excitation is proportional to the tunnelling rate, which is given by [13, 80]

$$\left(\frac{2(2I_P)^{3/2}}{|F(t_0)|}\right)^{\left(\frac{2}{\sqrt{2I_P}}-1\right)} \exp\left(\frac{-2(2I_P)^{3/2}}{3|F(t_0)|}\right), \quad (4.6)$$

where  $I_P$  stands for the ionisation potential.

Additionally the lateral momentum the electron possesses after tunnelling is given by

$$\exp(-p_{\perp}^2 \sqrt{2I_P} / |F(t_0)|) \quad (4.7)$$

(see [80]).

The second pulse imparts additional momentum onto the atoms following the same principle and its overlap with the first beam is varied systematically. For every trajectory starting inside the focus of the first beam, the individual position inside the second focus is calculated and the additional acceleration is added accordingly. From the retrieved trajectories the final position on the detector after the drift tube is computed (see figure 4.8 on the right).

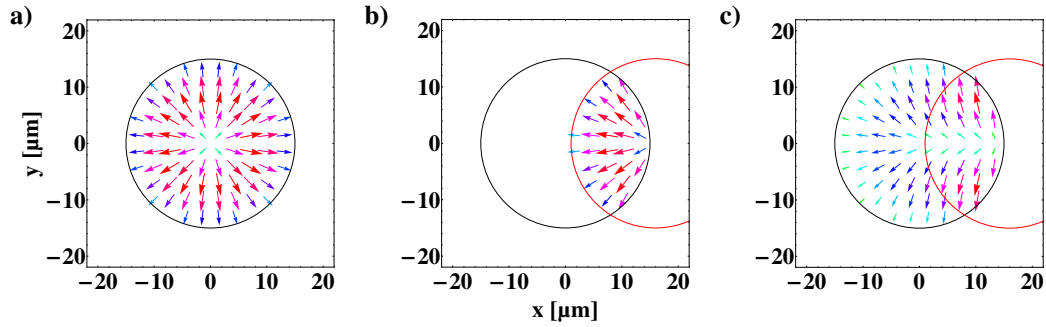


Figure 4.7: Vector plots of the momentum imparted on the atoms. The arrows indicate the direction of momentum transfer and the magnitude (length of the arrows). The circles with a diameter of the focal waists of the two laser beams indicate the two laser foci separated by  $16\mu\text{m}$  from centre to centre. The black and red circle designate the first and second laser beam respectively.

- a) Momentum distribution induced by the first laser pulse alone.
- b) Momentum distribution induced solely by the second elliptically polarised laser pulse. The momentum transfer is only shown for the overlap region where excited neutrals are expected.
- c) The combined momentum transfer of both laser pulses, shown only for the region where excited neutrals are expected.

To visualise the additional acceleration a representation of the imparted momentum in the focus region is shown in figure 4.7. In 4.7 a) the momentum of the first pulse points outwards and its maximum is at the point of the highest gradient which is located at half the beam waist distance from centre. In 4.7 b) the pure influence of the second beam acting inside the beam waist of the first focus is shown, while 4.7 c) finally shows the imparted momentum of the two combined pulses. Due to the predominantly one sided acceleration of the second pulse, one can clearly see a momentum imbalance towards the left side in the final momentum representation.

Figure 4.8 shows the full detector images and the results of the calculations for displacements in one direction. There exists a very good agreement between the calculations and the measured distributions. Most of the visible features are present in both pictures. Not only does the general shape fit very nicely, also the absolute size of calculation and measurement exhibits a very high agreement. Additionally, the probability structure inside the outer shape shows a very high similarity as well. In the first row the results of only applying the

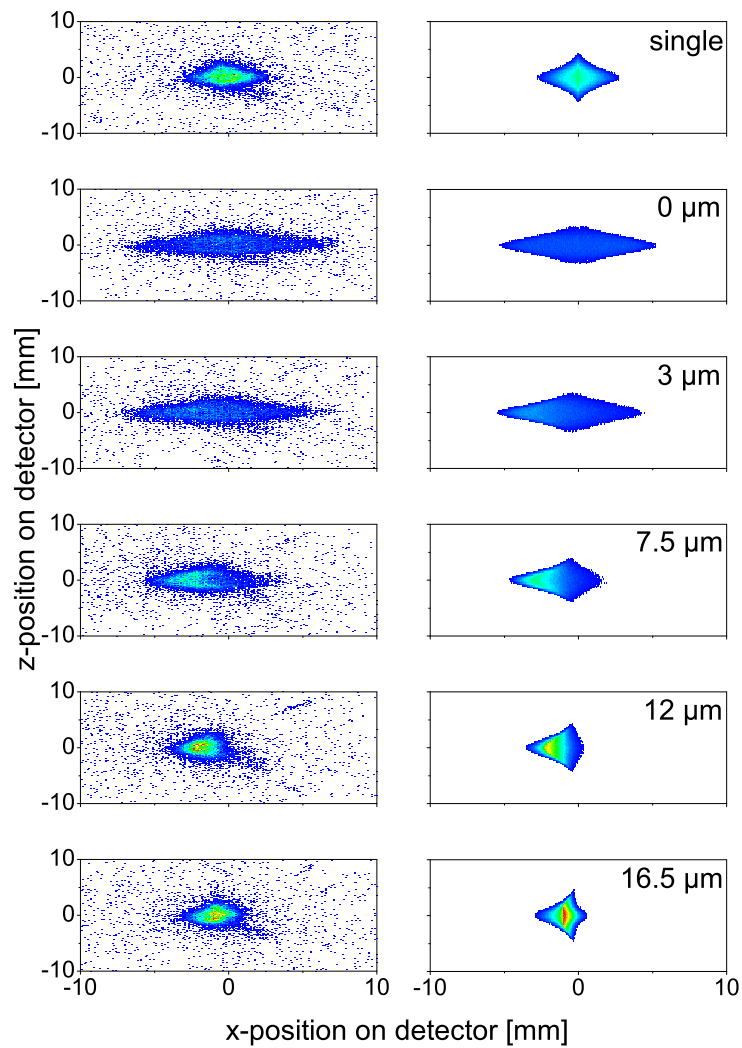


Figure 4.8: Experimental (left side) and theoretical (right side) neutral atom distribution on the detector for differently displaced beams. Centre to centre distance between the two foci is given on the right side. The number of atoms detected at any position is colour coded from blue (low) to red (high). The laser propagates along the  $z$ -axis and the time delay between the two pulses is  $500 \text{ fs}$ .

first pulse are shown, while the second row contains results where both pulses were present without lateral displacement. The figures below show results for ever higher displacements of the second beam along the  $x$ -axis with respect to the first one. Especially the measurement at  $12 \mu\text{m}$  distance between the foci shows a clear shift of the atomic distribution towards the left side.

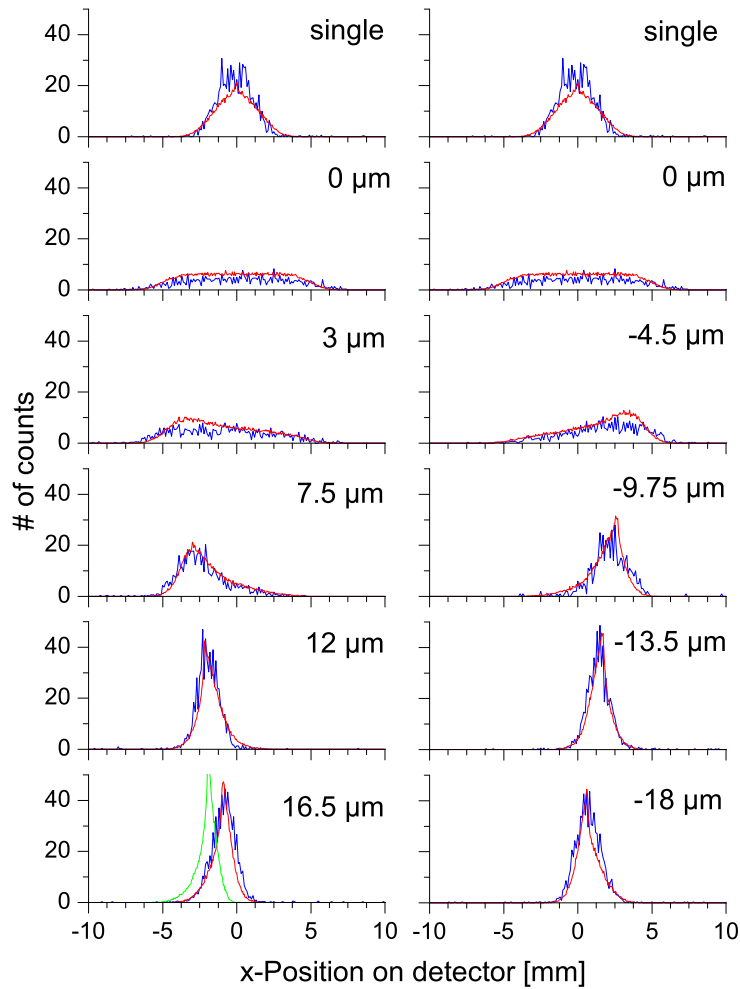


Figure 4.9: Cuts through the density distributions at the focal plane for differently displaced beams.

Blue line: Measured Rydberg distributions.

Red line: Calculations for values used in the experiment.

Green line: Calculation using a higher intensity for the second laser pulse (factor  $\sqrt{2}$ ).

To analyse this comparison in more detail, cuts through the focal plane at  $z = 0$  are shown in figure 4.9. This time displacements in both directions are displayed. To gauge the focus displacement of the second beam in the experiment, the adjustment made at mirror M1 (see figure 3.4) was controlled by measuring the distance between the two beam spot centres outside of the

vacuum chamber after a long beam path of 14.5 *m*. This yielded a linear dependency of the adjustment of the mirror to the displacement in the focus. One measurement (indicated 7.5  $\mu\text{m}$  in figure 4.9) was used to obtain the correct correlation between the measured distances of the beam spots and the actual focus displacements inside the vacuum chamber. All other curves were then obtained using the correlated focus displacement. The only additional adjustment is a single common normalisation factor applied to all curves to adjust the height.

## 4.4 Conclusion

A very good agreement between the measured data and the calculation is apparent. The position of the distribution and the structure within is very well reproduced for all eight displacements. The high agreement over a wide range of displacements reveals the robustness and broad applicability of the underlying acceleration theory, which was presented in section 2.3. Not only the single pulse acceleration can be reproduced quite nicely, also the additional acceleration shows a high agreement. The assumption that the electron is tunnelling at the maximum of the first pulse, which implicates that for half the pulse length the Rydberg atom is actively accelerated, while the second elliptical pulse is accelerating the neutral atom over its full length, obviously seems to be true, given the high agreement between measurement and simulation. Therefore, the tunnelling and subsequent acceleration can be seen as two independent parts of the process. A gradient free field would yield FTI atoms without acceleration, while the second elliptical pulse yields acceleration without the FTI process taking place simultaneously. It should be remarked again that the additional acceleration is only possible due to the high survival rate of the Rydberg atoms in the strong field. A calculation with a slightly stronger second pulse (intensity multiplied by a factor of  $\sqrt{2}$ , shown in green) shows a significantly higher deflection. This reveals on the one hand the high dependency of the calculated deflection on the focus parameters, as only the calculations with the actually used experimental values fits to the measured deflection. On the other hand the green calculation indicates the possible scalability of the deflection, as a clear shift in the expected deflection

is visible compared to the red case. Proper pulse control or multi step setups could thus provide a very compelling option to "steer" neutral atoms with high control, using the ponderomotive force in a cascaded manner.

## 5 Standing Wave

The second main part of this thesis focuses on a standing wave configuration with femtosecond laser pulses. An optical standing wave represents a substantially different electromagnetic field. In contrast to the classical field of a travelling laser pulse, the minima and maxima of the intensity are fixed in space and only their heights are oscillating in time. A standing wave is usually formed by the interference of two continuous waves travelling in opposite direction, the classic example being a continuous wave resonator. However, the overlap of two counter-propagating pulses can also form a standing field during the short moment of overlap in time. This type of field has been used in the strong field regime to modify HHG [81], form electron bunches [82] or characterise Bose-Einstein condensates [83].

As mentioned before (see section 2.3), the acceleration observed for neutral atoms depends on the gradient of the electric field, which, for the electromagnetic field of a single laser pulse, is usually provided by the envelope of the beam and can, therefore, be increased by focussing. To test the upper limits of the acceleration and the stability of the Rydberg atoms one would thus have to focus a Gaussian pulse even harder or use considerably shorter pulses while maintaining the same pulse energy to achieve a higher gradient. In a standing wave, in contrast, the gradient of the electric field component is considerably different. While the intensity in the focus area changes on a  $\mu m$  scale, the gradient in the standing wave alternates on the wavelength scale. Due to this, a higher gradient can be achieved with lower laser energy. But most importantly, the alternating nature of the standing wave field does not only allow for a high gradient and accordingly a high acceleration, but due to the gradient itself changing on this short length scale, the whole process of frustrated tunnelling has to be revisited. Many explanations in this picture

rely on the dipole approximation (see section 2.1) which cannot automatically be expected to hold true under these conditions.

Therefore, the use of a standing wave can expand the high field research in several ways:

- Even steeper electric field gradient for acceleration and survival
- Gradient on shorter length scale to test the limits of the dipole approximation in classic high field physics
- “Exotic” field structure with areas of pure electric or pure magnetic field component

## 5.1 Electromagnetic field configuration

A fundamental standing wave is formed by overlapping two counter-propagating plane wave fields of equal strength, wavelength and polarisation. In case of linear polarisation and a continuous wave (cw) laser one obtains for the electric field component

$$E_{1,2} = F \cos(\omega t \mp kz) \quad (5.1)$$

$$E_{sw} = 2F \cos(\omega t) \cos(kz), \quad (5.2)$$

where  $E_{1,2}$  are the single beams with  $+$  or  $-$  respectively and  $E_{sw}$  is the standing wave.  $F$  represents the field strength. The time evolution and the spatial evolution are no longer combined in one argument but are now separate from each other. The electric field passes through its full excursion only at the defined positions  $z = n\pi/k$ , with  $n = 0, 1, 2, \dots$  and stays zero for  $z = (n + 0.5)\pi/k$ . With the definition of the wave number  $k = 2\pi/\lambda$ , one can directly obtain the length from the field maximum to a stationary point or the field minimum and calculate the gradient.

Unfortunately such a basic or fundamental standing wave with linear polarised fields, while easier realisable in the experimental setup, cannot be used to measure the desired Rydberg atoms selectively. The reason for this lies in the fact that each of the two counter-propagating beams on its own already

interacts with the atoms. Considering the fact, that the volume where the standing wave is formed is only about  $13.5 \mu\text{m}$  long along the laser axis, given the speed of light for a  $45 \text{ fs}$  pulse, compared to several millimetres of sufficiently high intensity to produce Rydberg atoms for each of the two beams on their own, the amount of atoms excited in the standing wave is negligible compared to the overall amount of Rydberg atoms which get excited in the combined fields. Since the measurement accumulates all atoms that drift with their normal thermal beam velocity from the interaction zone to the detector, and one cannot discern where they stem from, a separation of the results would be impossible. Therefore, another field configuration had to be used which suppresses atoms not originating from the standing wave itself.

Recalling the fact that only linearly polarised light excites atoms into Rydberg states, which holds particularly true for He atoms, both beams were changed to elliptical polarisation.

$$\mathbf{E}_1 = F [\mathbf{e}_x \cos(\omega t - kz) + \mathbf{e}_y \epsilon \sin(\omega t - kz)] \quad (5.3)$$

$$\mathbf{E}_2 = F [\mathbf{e}_x \cos(\omega t + kz) \pm \mathbf{e}_y \epsilon \sin(\omega t + kz)] \quad (5.4)$$

$\epsilon$  is the ellipticity, where  $\epsilon = 0$  denotes linear polarisation and  $\epsilon = 1$  fully circular polarised light. The  $\pm$  sign denotes the two possible helicity orientations the two beams can have with respect to each other.

Calculating the standing wave for both helicities yields:

$$\mathbf{E}_+ = 2F \cos(kz) [\mathbf{e}_x \cos(\omega t) + \mathbf{e}_y \epsilon \sin(\omega t)] \quad (5.5)$$

$$\mathbf{E}_- = 2F \underbrace{\cos(\omega t)}_a \underbrace{[\mathbf{e}_x \cos(kz) - \mathbf{e}_y \epsilon \sin(kz)]}_b \quad (5.6)$$

Although the two possibilities look very similar on first glance, the results are substantially different.

In the simplified case of circular polarisation  $\epsilon = 1$ , the difference can be easily understood. In the co-rotating case  $\mathbf{E}_+$  the resulting field is circularly polarised (term b). The amplitude of this light varies over the propagation axis of the two laser beams and gives rise to the typical intensity modulation along the  $z$ -axis of  $\cos^2(kz)$ . While a standing wave is produced, no Rydberg excitation is expected because of the circular polarisation of the light field itself.

In the second case of counter-rotating polarisation  $\mathbf{E}_-$  the light is linearly polarised (term a), but it rotates with a constant field amplitude along the  $z$ -axis. Because of this, the intensity along the  $z$ -axis is constant, which corresponds to a field without gradient. Without a gradient present no acceleration is expected for the neutral atoms.

However, the situation changes if one does not use circular polarised light and instead changes to elliptical light with  $0 < \epsilon < 1$ . In the  $\mathbf{E}_+$  case the polarisation is the same as the polarisation of each individual beam, which implies that it is now elliptical as well. Therefore, there is still no Rydberg excitation expected. The cycle averaged intensity in the  $\mathbf{E}_-$  case reveals how the standing wave can finally be used effectively. The intensity in the elliptical case reads:

$$\bar{I}(z) = \overline{\mathbf{E}_-^2} = F^2 [1 + \epsilon^2 + (1 - \epsilon^2) \cos(2kz)] \quad (5.7)$$

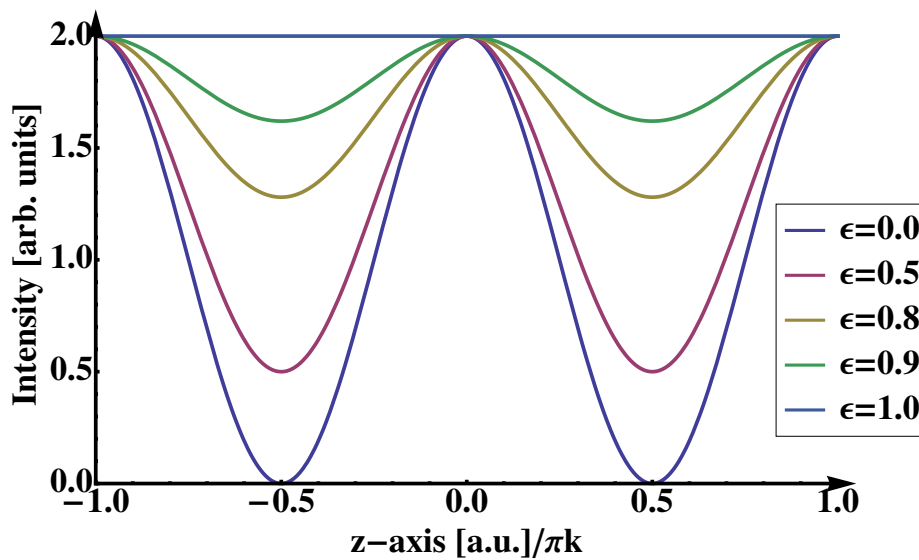


Figure 5.1: Intensity distribution for cycle averaged standing wave (using equation 5.7).

The resulting intensity for different  $\epsilon$  is shown in figure 5.2. The intensity gradient of the resulting field can be tuned by changing the ellipticity of the two laser beams while still keeping the linear polarisation of the combined field.

For different ellipticities or field strengths in both beams it changes to equation 5.8, which still gives a very similar intensity distribution for slightly mismatched field strengths or ellipticities.

$$\bar{I}^*(z) = \frac{F_1^2}{2} (1 + \epsilon_1^2) + \frac{F_2^2}{2} (1 + \epsilon_2^2) + F_1 F_2 (1 - \epsilon_1 \epsilon_2) \cos(2kz) \quad (5.8)$$

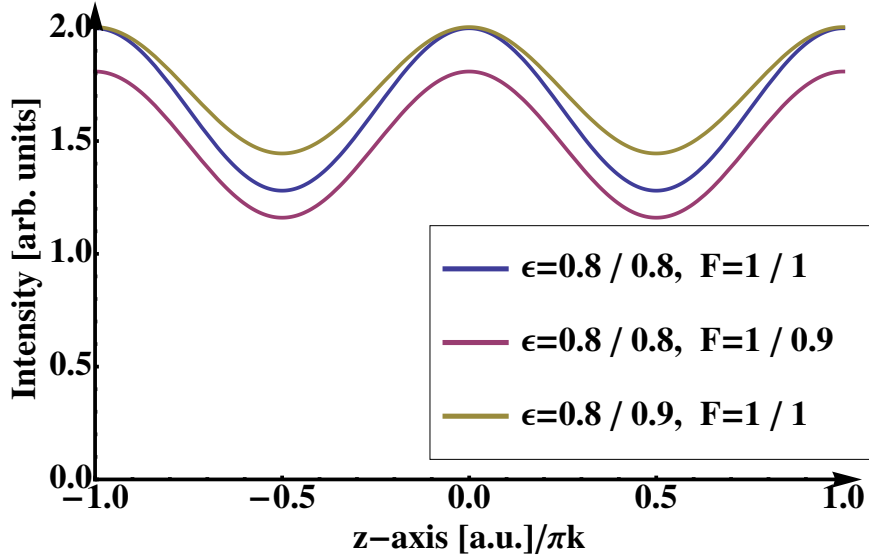


Figure 5.2: Intensity distribution for cycle averaged standing wave in a slightly mismatched case (using equation 5.8).

In case of different field strengths the total intensity drops slightly, while the gradient stays almost the same. For mismatched ellipticities the curve changes to a result of an ellipticity in between both individual values.

One can now make a first assumption about the spatial deflection such a standing wave is expected to cause. Using the ideas of the theory presented for the single pulse acceleration, which agreed very well with experimental results (see [68]), the same method can be applied to the standing wave. It is assumed that the neutral atom survives the acting field and is mainly accelerated by the ponderomotive force acting on the quasi free electron far from the core. The ponderomotive force depends on the gradient of the field intensity and can thus be directly calculated for the simplified case (see also equation 2.34).

$$F_p = -\frac{F^2 k}{\omega^2} (\epsilon^2 - 1) \sin(2kz) \quad (5.9)$$

The final velocity of the full neutral atom is given by

$$v_f = \int_{t_0}^{\infty} a_{cms}(t) dt = \frac{F_p}{M} \int_{t_0}^{\infty} f(t) dt, \quad (5.10)$$

with  $\int_{t_0}^{\infty} f(t) dt$  representing an effective time of acceleration, which changes depending on the time of tunnelling during the pulse.

The most common time of tunnelling will be at the maximum of intensity, which implies that the electron, and in turn the whole helium atom, would be accelerated for half the pulse length. By calculating this final velocity  $v_f$  for all  $z$ -positions between  $z = \mp 0.5\pi k$  inside the standing wave with equal probability, to include all possible gradients of the field, a characteristic distribution is retrieved (see figure 5.3).

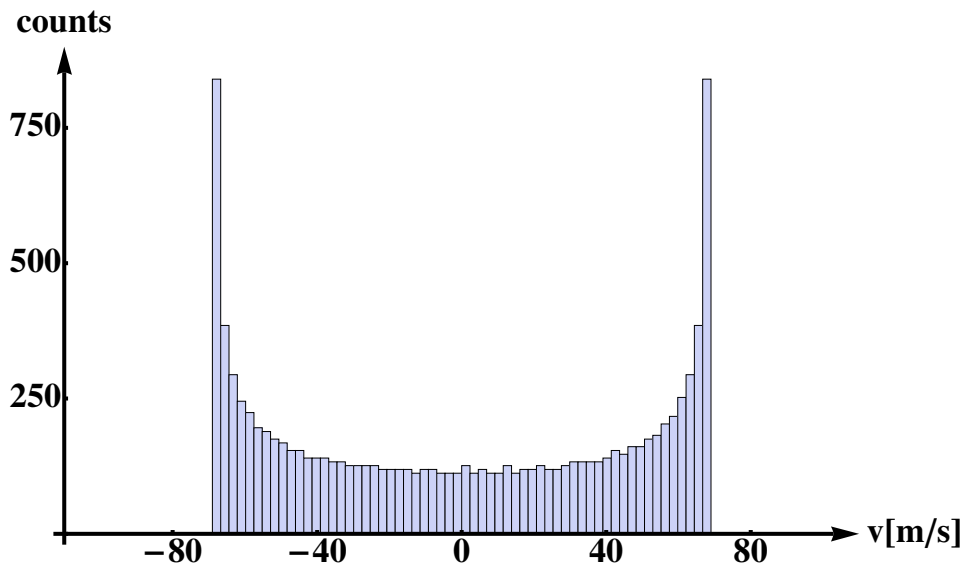


Figure 5.3: Velocity distribution of neutral atoms accelerated by the standing wave for exactly half the laser pulse.

A sharp increase for the highest possible velocity is observed, while the distribution around zero velocity is rather flat. In this simplified case only the width of the distribution changes dependent on the field strength and ellipticity, but its shape stays the same.

However, while the used acceleration time is the most probable, tunnelling is also possible before or after the field reaches its maximum. The electric field then acts longer or shorter on the tunnelled electron, which accumulates different momenta. To include this effect, the same histogram is calculated while allowing for a slight variation of  $t_0$  around the maximum overlap of the two pulses (see figure 5.4).

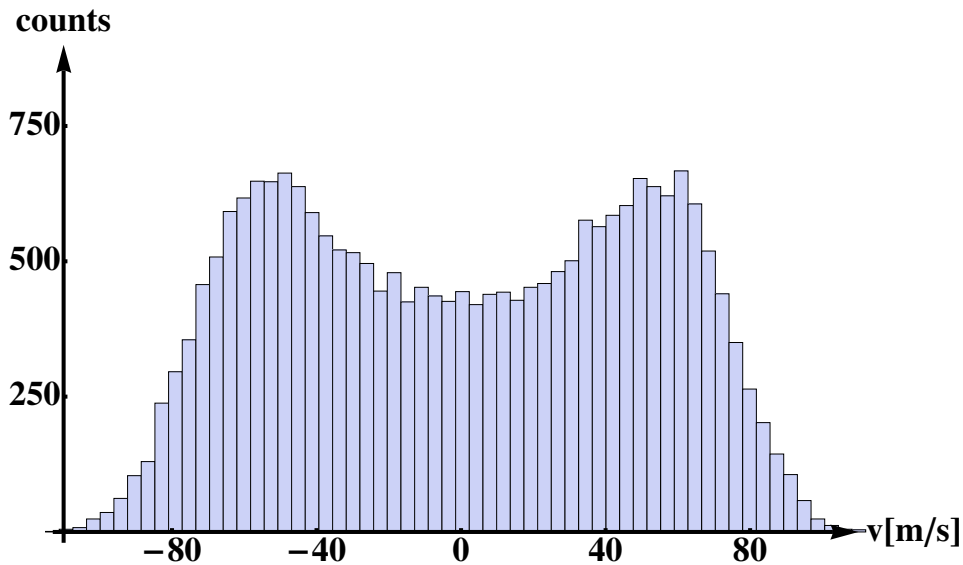


Figure 5.4: Velocity distribution of neutral atoms accelerated by the standing wave for a random time which follows a normal distribution with a FWHM of 100 *a.u.* around half the laser pulse length.

The sharp drop of at the maximum velocity is gone and instead a double hump structure is visible, which represents the now possible variation in maximum velocity due to the different effective acceleration times. It should be noted, that for these basic assessments no weighting due to the changing tunnelling rate along the  $z$ -axis, as well as for the actual microscopic field strength at the time of tunnelling during the pulse, is included. However, the basic structure observed here can also be seen in some of the full calculation results shown later. The two figures 5.3 and 5.4 are calculated for a field strength of  $F = 0.1$  *a.u.* and an ellipticity of  $\epsilon = 0.85$  and already show velocities comparable to the highest ones measured. The velocities calculated by this method for higher intensities, as they are applied in the experiment, are considerably higher than anything observed in the experiment, which already hints at the fact that there seems to be an upper limit to the momentum the electron can obtain, while still

being bound to the ionic core to form a neutral atom. The full Monte-Carlo simulations shown later reveal the interplay between the obtained maximum velocity and the stability of the helium atoms.

## 5.2 Simple quantum mechanical model

The acceleration can also be explained with the help of a simplified quantum mechanical model. Again, the atoms are assumed to be stable against ionisation and only motion along the standing wave axis is allowed. Since  $\cos^2(x)$  is proportional to  $\frac{1}{2} \cos(2x)$  the Hamiltonian is given by [84]

$$\hat{H} = -\frac{1}{2M} \frac{\partial^2}{\partial z^2} + V_0 \cos^2 kz \quad (5.11)$$

where  $V_0 = \frac{F^2}{2\omega^2}(1 - \epsilon^2)$  represents the strength of the potential inside the standing wave.

The plane wave solutions are defined as

$$\psi = \sum_n c_n(t) e^{inkz}. \quad (5.12)$$

The  $c_n$  coefficients represent the probability to find the atom with a momentum of  $nk$  and have to fulfill the following differential equation:

$$i \frac{dc_n}{dt} = \left( \frac{k^2 n^2}{2M} + \frac{V_0}{2} \right) c_n + \frac{V_0}{4} (c_{n-2} + c_{n+2}). \quad (5.13)$$

The last term on the right hand side already reveals the fact, that the atom momentum can only change by an even number.

The solution to this differential equation can be found analytically [84] and reads

$$c_n = i^n e^{-iV_0 t} J_n(V_0 t), \quad (5.14)$$

with  $n = 0, \pm 2, \pm 4, \dots$ .  $J_n$  represents the  $n$ th Bessel function of the first kind.

The probability for the atom to absorb an even number  $n$  of photons is now determined by

$$P_n = |c_n|^2 = \left| J_n \left( \frac{F^2}{2\omega^2} (1 - \epsilon^2) t \right) \right|^2, \quad (5.15)$$

with  $t = \sqrt{\pi} \tau \operatorname{erfc}(\frac{t_0}{\tau})$ .

A probability distribution, to find the neutral atom with the corresponding two photon momenta velocity change, can now be calculated. The velocity of the full neutral atom is given by the number of absorbed photon momenta

$$v = \frac{n2k}{M} \quad (5.16)$$

and yields very similar results to the classical calculation shown before (see figure 5.3 and 5.4).

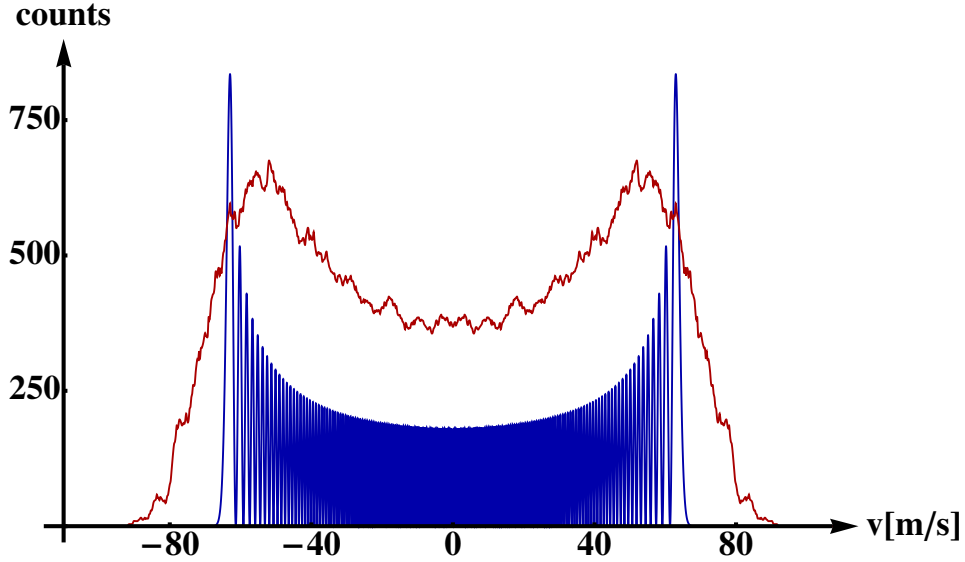


Figure 5.5: Velocity distribution calculated with the simplified quantum mechanical model for a fixed time of tunnelling at the pulse maximum (shown in blue) and for random times around the pulse maximum (shown in red).

A more detailed look at the quantum mechanical solution of the two body problem is presenten in the Appendix. The simplified potential used here can also be identified as the first part of equation A.14. The total momentum the atom is left with after the laser pulses are over corresponds to more than 400 two photon momenta. Therefore, the absorption of such a high momentum

by the neutral atom within the pulse length of 55 fs yields a scattering rate higher than  $10^{16} \text{ s}^{-1}$  in this picture.

### 5.3 Observing the standing wave deflection

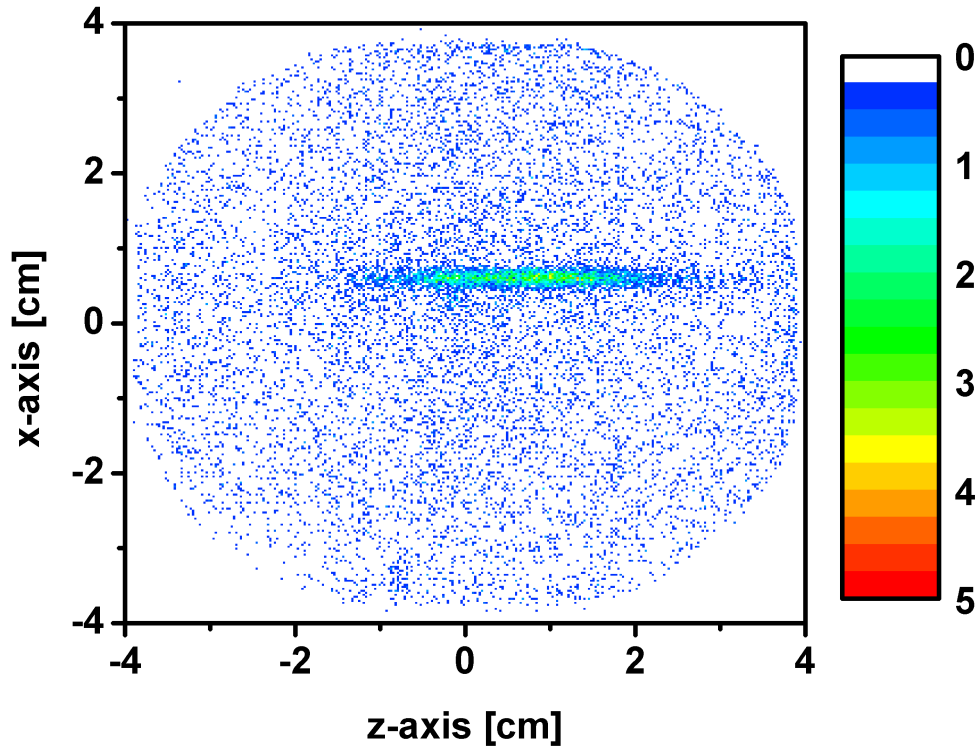


Figure 5.6: Typical detector image for the standing wave.  
The laser beams are aligned along the z-axis.

An experimental sample result measured with the spatially resolving detector is shown in figure 5.6. A clear distribution of excited neutral atoms along the laser axis is visible. It is important to note that this distribution is only visible for the expected field configuration, marked as  $\mathbf{E}_-$  before (equation 5.6). In the  $\mathbf{E}_+$  case no enhancement over the uniform background is visible, as can be seen in figure 5.7 b). Likewise, no signal is observed for each beam alone in elliptical polarisation. This means, that by applying the aforementioned field configuration, a background free observation of atoms purely originating from the standing wave is realised, as no additional neutral atoms are excited.

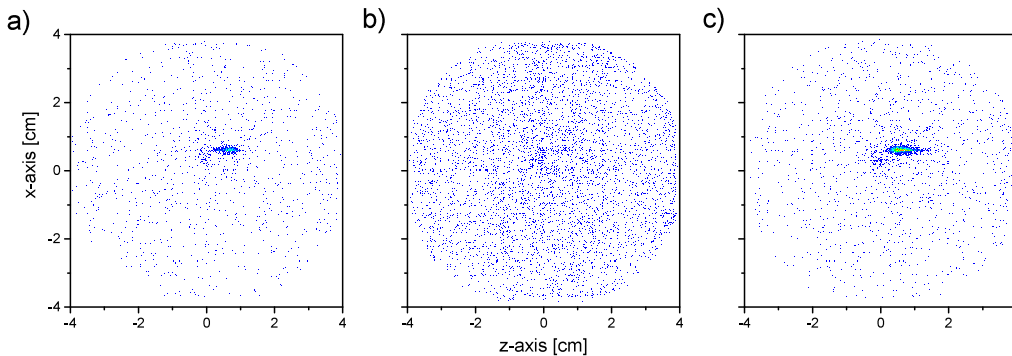


Figure 5.7: Additional detector images resulting from using

- a) only the left arm in linear polarisation
- b) both arms in the co-rotating case  $\mathbf{E}_+$
- c) only the right arm in linear polarisation

Figure 5.7 also shows the pure signal stemming from each laser beam alone in the linear case, which is clearly shorter and differently shaped than the clear line observed in the standing wave field. For the linear polarised single pulses the length of the signal along the laser axis is broadened during the projection of the focus region onto the detector due to the divergence of the gas beam.

For the standing wave all atoms stem from the overlap region of the two beams, which is constricted to the  $13.5 \mu\text{m}$  the light travels during the pulse length. Due to this, no beam divergence has to be included and the visible line can be directly converted into a velocity distribution imparted by the standing wave. Compared to the results shown before (e.g. figure 4.1) the gradient of the standing wave is perpendicular to the gradient of the laser focus and is aligned along the propagation axis (in this case the  $z$ -axis). Therefore, the width of the observed line is determined by the velocity imparted on the Rydberg atoms by focussing the beam, while the length represents the imparted momentum by the standing wave gradient. One can already see the huge difference between the two, which directly shows how much stronger the standing wave deflection actually is.

In case of the maximum energy of  $2.3 \text{ mJ}$  each beam would produce a focus intensity of  $\approx 1 \cdot 10^{15} \text{ W/cm}^2$ . While the overlap adjustment of the two beam foci inside the vacuum chamber was done very carefully and the lateral displacement should be minimal, the displacement alongside the beam axis is

a lot harder to retrieve. A possible misalignment could thus prevent a perfect overlap of the two smallest diameters. Additionally, the used beam splitter, while specifically optimised for the polarisation that the aforementioned energy adjustment (see section 3.3) provided, did not split the beam equally, but in a 45%:55% ratio.

All of these factors prohibit an exact calculation of the field strength present in the standing wave, which was produced in the laboratory. Instead, the full energy entering the interaction chamber is used as a reliable value to monitor the changes in the experimental situation. Because of the beam splitter behaviour, the two beams in each arm were not polarised equally and thus a different angle for each quarter wave plate was used to compensate for this in the final measurements. The angle was determined by experimentally locating the highest excitation rate of Rydberg atoms for each beam, which directly corresponds to the case for linearly polarised light (see figure 2.6). As soon as a slight ellipticity is introduced, the signal drops significantly. The midpoint in degree between two of these maxima of Rydberg excitation serve as the quarter wave plate position for the standing wave measurement for each beam individually, as these should produce circular polarised light.

Figure 5.8 shows the velocity distribution obtained for the three lightest noble gases helium, neon and argon. The measurements were taken with an equal angle of both quarter wave plates and a total energy of 1.5 *mJ*. Because of the Maxwell distributions for the different gases in the effusive beam, an individual factor is used for each gas to convert the point of impact into an acquired velocity. All three gases can be detected with the MCP and Rydberg atoms are excited. An acceleration along the laser axis is observed for every gas, which means that the fundamental acceleration concept holds true for the standing wave. Owing to the different atomic masses of 4, 20 and 40 *a.u.* a different velocity is acquired for each of them. In the case of argon, a very small additional signal is visible at the foot of the argon peak to the right side. It stems from a tiny amount of neutral argon atoms that are produced by the single elliptical beam. While these were visible due to the extremely long measurement time, no neutral helium atoms are excited by a single elliptical laser pulse at all. The maximum velocity obtained for each gas is inversely proportional to the atomic mass. As stated in section 2.3, it is mainly the

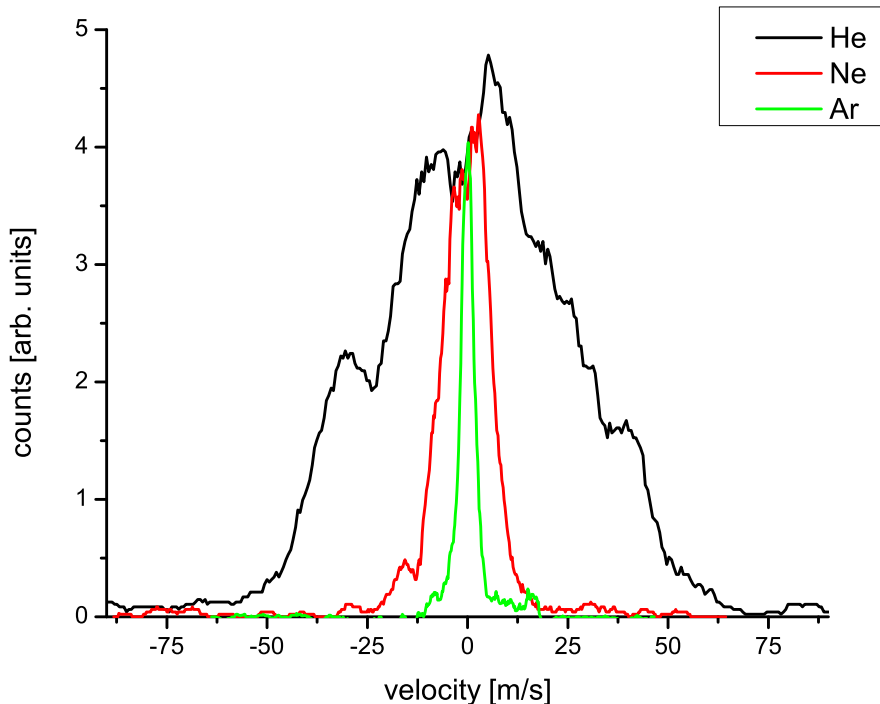


Figure 5.8: Comparison of the velocity distributions of three different noble gases. The total energy of the entering laser beams is  $1.5 \text{ mJ}$ .

electron that is acquiring kinetic energy and the ionic core is pulled along. Since the acquired energy of all electrons is comparable, only the total mass that is accelerated changes. Therefore, a velocity distribution depending on the the total mass of the neutral atom is confirmed in the standing wave.

All measurements displayed in the following sections concentrate on helium for two reasons. On the one hand, the observed acceleration is strong enough to be easily discernible on the detector due to the low total mass. On the other hand, at the most two electrons have to be included when simulating the results, which opens the possibility to perform a full quantum mechanical calculation.

Because of the rather small interaction volume, combined with the very low density of atoms in the gas beam to ensure single atom interaction, the excitation rate of Rydberg atoms is rather low. Several methods have been used to extract as much information as possible from the obtained signal.

Firstly, only a fixed narrow stripe of signal along the  $z$ -axis of the detector was used, which allows for a better suppression of the background signal, visible above and below the stripe in figure 5.6, which inevitably builds up over the long measurement time. These selective counts are then projected onto the  $z$ -axis to sum up all signal in the width of the distribution.

To be able to convert the measured spatial distribution into a velocity distribution imposed on the Rydberg atoms during the short interaction, each point of impact has to be associated with a velocity. This is only possible if one includes the flight time from the interaction zone to the detector. This can be understood by looking at the conditions for the measured deflection.

$$d = \frac{l_{flight}}{v_{flight}} v_f, \quad (5.17)$$

with  $d$  being the distance of the measured point of impact to the center of the undisturbed gas beam,  $l_{flight}$  the flight length from interaction zone to the detector,  $v_{flight}$  the velocity of the atom inside the gas beam towards the detector and  $v_f$  the imparted velocity by the laser beam (see equation 5.10). While  $l_{flight}$  is fixed during the experiment, different combinations of  $v_{flight}$  and  $v_f$  can yield the same measured distance  $d$ . In other words, slow atoms have more time to deviate from their initial flight path and, therefore, can arrive at the same spot on the detector as fast atoms that only got accelerated a little during the laser interaction. The full neutral atom signal, which is detected, still contains the Maxwell velocity distribution of the thermal beam, which is rather broad. For an accurate extraction of  $v_f$  from the detector signal only a small part of the distribution can be used and, therefore, the amount of useable signal would be severely limited. To compensate for this, six different flight time-bins, centred at  $150 \mu s$ ,  $182 \mu s$ ,  $220 \mu s$ ,  $265 \mu s$ ,  $320 \mu s$  and  $385 \mu s$  have been used instead of just one fixed flight time at the maximum of the Maxwell distribution. The spatial picture of each timeslice on its own is converted into a velocity distribution along the  $z$ -axis with the corresponding  $v_{flight}$  for each time-bin. This conversion is only possible if the velocity introduced by the laser field in drift direction of the beam is very small compared to the initial velocity the atoms have before interaction, so that no redistribution between the flight time-bins takes place. With a maximum laser induced velocity of  $\approx 90 \text{ m/s}$  compared to a mean thermal velocity of  $\approx 1700 \text{ m/s}$  this assumption

should not alter the results noticeably. All the individual calculated velocity data is then summed up to constitute the final velocity distribution, which includes almost all excited Rydberg atoms of the thermal beam that produced a signal on the MCP. Several measurements under different conditions have been performed. As mentioned before, no signal is visible if the quarter wave plates are set to the co-rotating case.

However, it has to be said that a slight deflection of atoms along the laser axis was visible in every measurement. This, in turn, means that no standing wave from two perfectly circular polarised counter-rotating beams could be achieved, because the  $\epsilon = 1$  case shown before should theoretically result in no acceleration at all. The reason for this lies most likely in the extremely high requirements for the two beams regarding equality in energy as well as polarisation, but could also be explained by the high dependence on perfect spatial adjustment and stability. The precision limit the quarter wave plates can be produced with has to be considered as well. The high quality achromatic wave plates which were used are manufactured with an allowed 5% optical retardation difference over their whole bandwidth of 600-1200 *nm*, which reduces to 2% over the bandwidth of the used laser system. The slight differences these optics could have introduced into each laser beam arm probably have prohibited the implementation of a standing wave without gradient, obtained by two perfectly circular polarised beams. Nevertheless, the clear observation of the standing wave by itself, especially considering the observed dependence on the correct helicity, still assure a high degree of precision.

## Acceleration by the focussing gradient

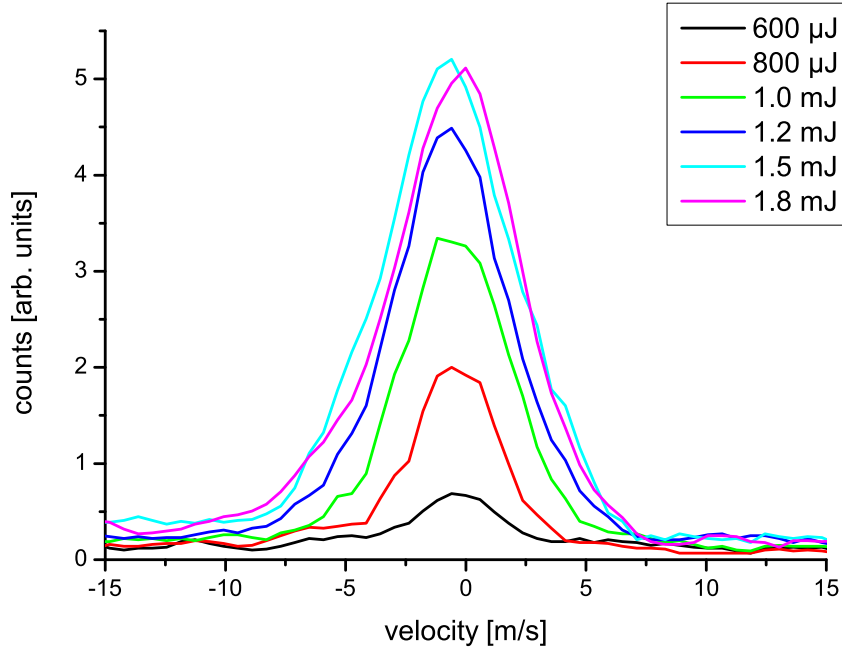


Figure 5.9: Perpendicular velocity stemming from the focus gradient of the standing wave for different total laser energies.

Figure 5.9 shows the width of the stripe for different energies entering the vacuum chamber. This perpendicular velocity is caused by the gradient of the laser focus and not by the gradient inside the standing wave. The graphs shown consist of the full signal inside the line projected onto the  $x$ -axis.

energy	FWHM
$600 \mu J$	4.1
$800 \mu J$	4.2
$1.0 mJ$	5.3
$1.2 mJ$	5.7
$1.5 mJ$	6.7
$1.8 mJ$	6.3

Table 5.1: FWHM values for the measurements shown in figure 5.9.

Table 5.1 gives the Full width at half maximum values (FWHM) for each measurement, obtained by fitting a Gaussian onto each distribution, to highlight the clear broadening. Comparing figure 5.9 to figure 5.10 demonstrates the difference the perpendicular gradient of the focus has on the neutral atoms compared to the standing wave gradient.

### Acceleration by the standing wave gradient

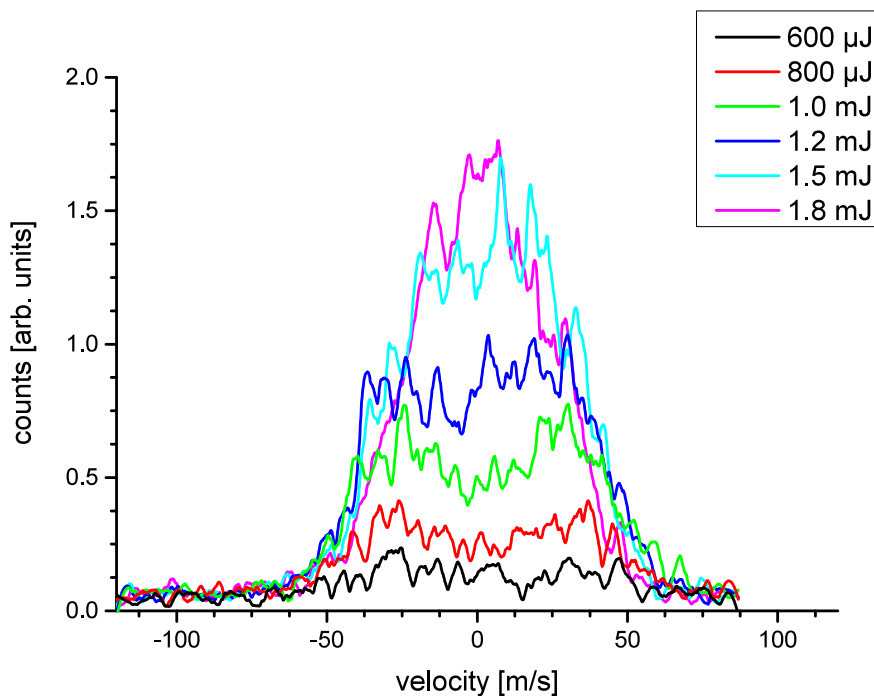


Figure 5.10: Initial velocity distributions stemming from the standing wave for different total laser energies and an ellipticity of  $\epsilon = 0.85$ .

In figure 5.10 the standing wave velocity distributions of the first proof of principle measurement set is shown. Again, the same fixed value for both quarter wave plates has been used. It is immediately obvious that all distributions exhibit a very similar maximum velocity, although a wide range of energies was used. Only the amount of detected atoms changes and a clear peak around zero builds up. The behaviour visible in this measurement suggests, that there exists a maximum in the momentum a neutral atom can acquire inside the electric field before getting ionised.

To model this behaviour, the final velocity calculation explained before (see formula 5.10) was slightly modified. A maximum gradient is introduced, which discards atoms from the calculated velocity distribution if they exceed it. In case of a fixed tunnelling time at the pulse maximum, this acts as a direct cut-off of the distribution, which can be seen by comparing the green curves in figure 5.11 with the full curve in figure 5.3. With higher and higher intensities the extreme ends are removed and an almost flat distribution is left.

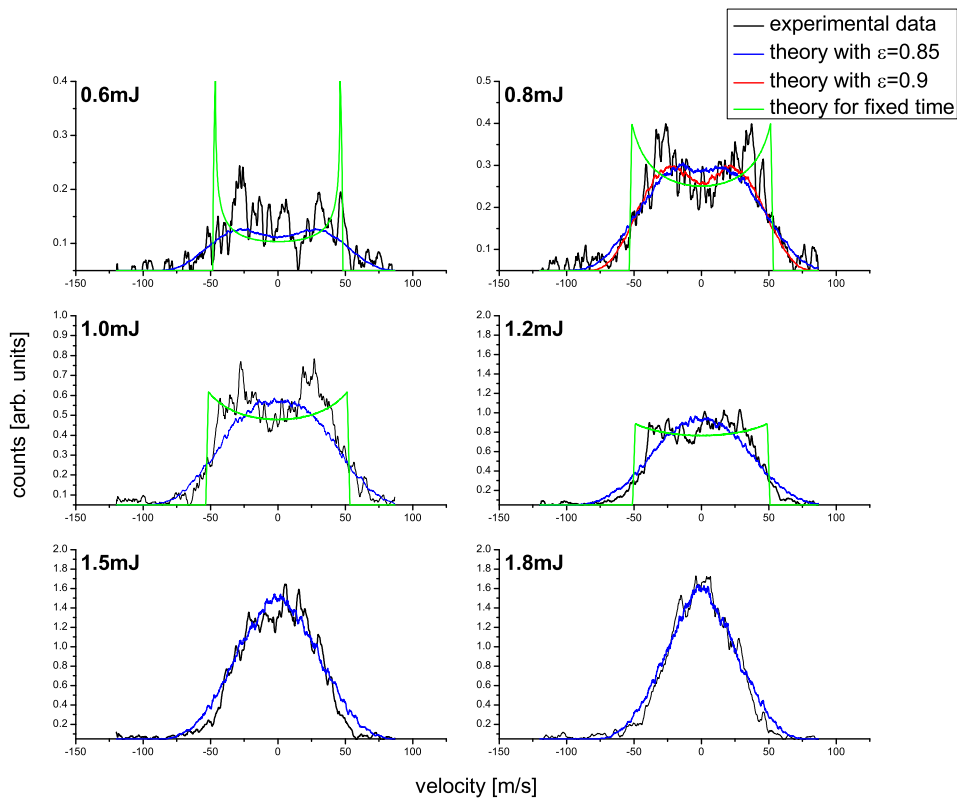


Figure 5.11: Comparison of measured velocity distribution and the simple theoretical explanation.

Black lines represent the measured data, blue lines the fit of the theoretical simulation for the measured ellipticity. The red line represents a slightly better fit obtained by using a different ellipticity. The green curves represent the theoretical simulation with a fixed time of tunnelling exactly at the pulse maximum (see also 5.3).

Figure 5.11 shows the results of this simple calculation for the measured ellipticity of  $\epsilon = 0.85$  and all energies depicted in figure 5.10. As before, tunnelling is allowed during a certain time width around the pulse maximum and the global cut-off is included by hand to accomplish a good fit. A compelling agreement between the measurement and the simple calculation can be achieved. With a different ellipticity an even better agreement can be obtained, which reproduces the visible double peak structure more closely, represented by the red line in figure 5.11.

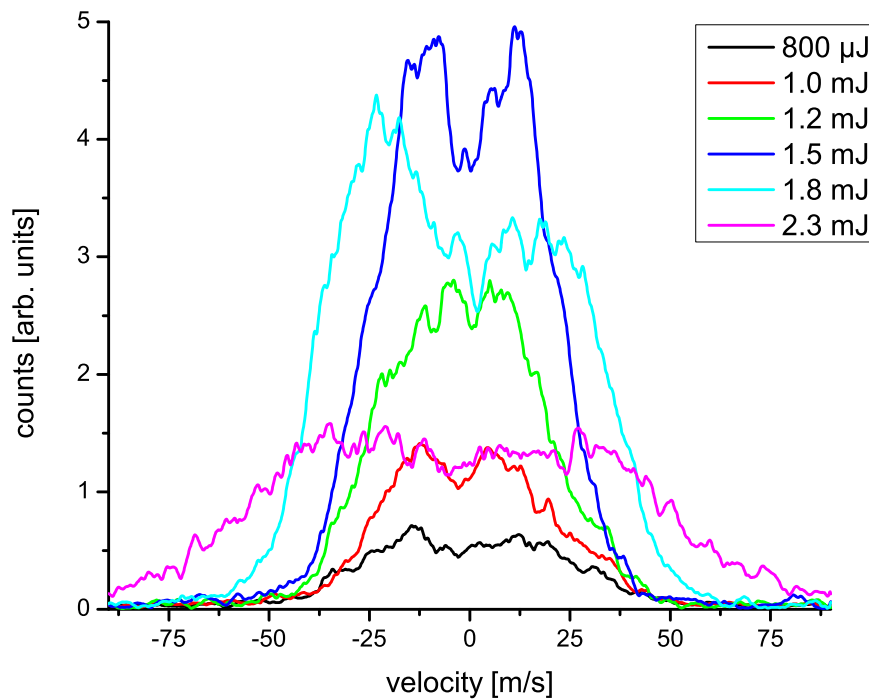


Figure 5.12: Final velocity distributions stemming from the standing wave for different total laser energies.

In figure 5.12 the standing wave acceleration results from another measurement set with a newly adjusted standing wave is shown. This time the ellipticity of each beam on its own was measured and different angles for the quarter wave plate of each side were used to compensate the difference due to the beam splitter. The ellipticity was then kept constant during the measurement set.

Several aspects of these distributions are noticeable. Starting with the lower energies one can see rather similar maximum velocities for all the measurements from  $800 \mu J$  up to  $1.5 mJ$ . Mainly the average amount of detected atoms increases due to the tunnelling rate, which increases for higher field strength. The tunnelling rate constitutes the starting point for the FTI process. At the two higher energies of  $1.8 mJ$  and  $2.3 mJ$  the signal is clearly broadened and slowly becoming smaller. In the  $2.3 mJ$  case a significant reduction in the amount of measured Rydberg atoms is visible. The other clearly visible aspect of the velocity distributions is a double peak structure in the  $1.8 mJ$ , the  $1.5 mJ$  and the  $1.0 mJ$  measurement. Apparently the uniform maximum acceleration that was observed before (see figure 5.10) did not hold true in the newly adjusted standing wave measurements. Additionally a measurement with a different ellipticity, corresponding to a higher gradient, also revealed a higher maximum velocity of the neutral atoms, which shows, that the artificial cut-off gradient cannot be considered a generally fixed value.

One unfortunate limitation concerning the ellipticity of each beam was found later on. The unequal split of the 50 : 50 beam splitter, in conjunction with the pulse energy attenuator described in section 3.3, introduced an energy dependent change in the polarisation of each laser arm. To determine this, the energy split percentage of each beam was measured for the used quarter wave plate angles and energy settings. It was performed by recording the laser energy that passed through a rotatable Glan-Taylor prism onto an energy detector. The prism separates  $s$  and  $p$  polarisation (only  $p$  polarised light is transmitted) and allows, therefore, the observation of the change of the polarisation of each arm while altering the beam energy.

The results of both beams are shown in figure 5.13 and 5.14. As can be seen in figure 5.13 the polarisation of the weaker beam is very consistent. The position of the maxima and minima does not change for different energies obtained with the attenuator. Unfortunately the result of the stronger beam is not constant. The position of the peak shifts continuously to different angles, which implies that the ellipticity is not the same for the different energies used in the experiment. Up to  $20^\circ$  difference between the extrema of the transmitted part for different total laser energies are recorded, which amounts to a change of up to 0.5 for the ellipticity when altering the total laser energy.

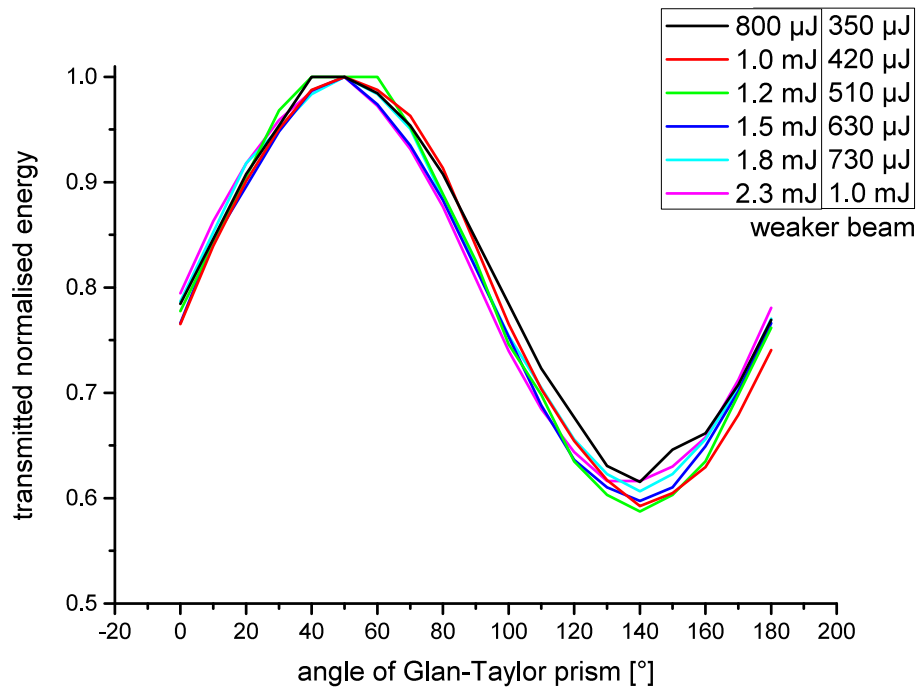


Figure 5.13: Measured polarisation characteristics of the quarter wave plate at the angle used in the measurement of figure 5.12 for all laser intensities of the weaker beam. The energy in the beam for every total energy used is shown in the top right.

The difference can be explained if one assumes that the beam splitter reflects only a pure polarisation. This reflection makes up the weaker beam, which in turn is very stable. On the other hand the polarisation contamination, which is present in the beam, is passing through the beam splitter and consecutively is only found in the stronger beam. Here it interferes and causes the observed ellipticity shift. This unresolvable problem influences the energy dependent measurements and prohibits a pure observation of the effect a changing intensity with constant ellipticity has in the standing wave, as the energy cannot be adjusted independently of the ellipticity.

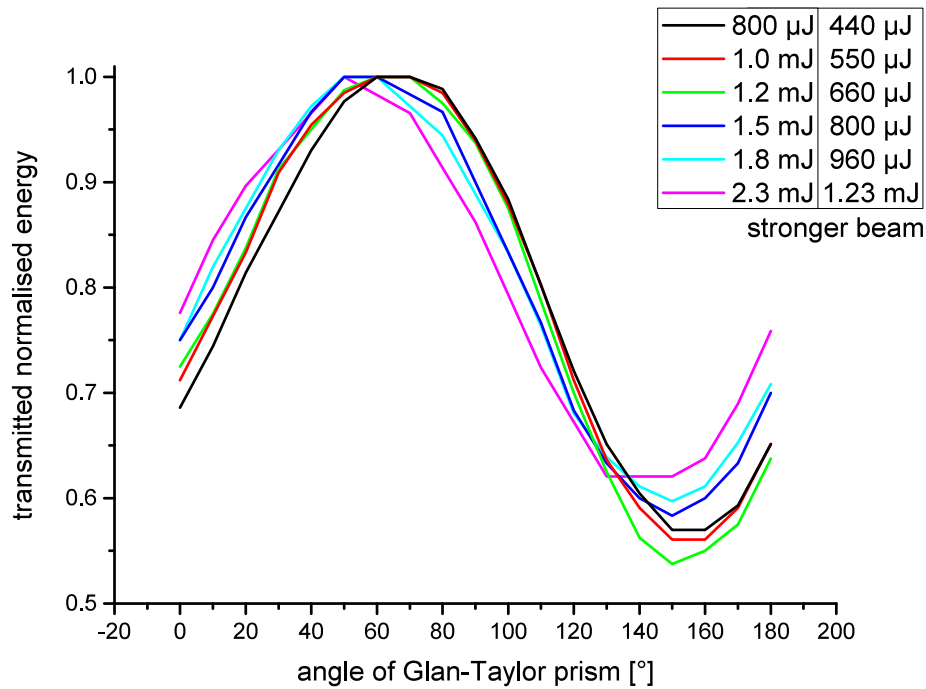


Figure 5.14: Measured polarisation characteristics of the quarter wave plate at the angle used in the measurement of figure 5.12 for all laser intensities of the stronger beam. The energy in the beam for every total energy used is shown in the top right.

One can still deduce several key aspects concerning the standing wave acceleration from these measurements. Firstly the atoms actually survive a wide range of field strength in this more complex polarised field. Secondly the maximum deflection visible for the lower four energies is very similar, while it dramatically changes for the two highest energies. This already discloses that a more complex correlation between field intensity and imparted momentum is at work here, compared to the single pulse experiment, where the deflection increases linearly. To comprehend this behaviour two kinds of calculations have been performed, which will be shown later.

## Acceleration dependence on ellipticity

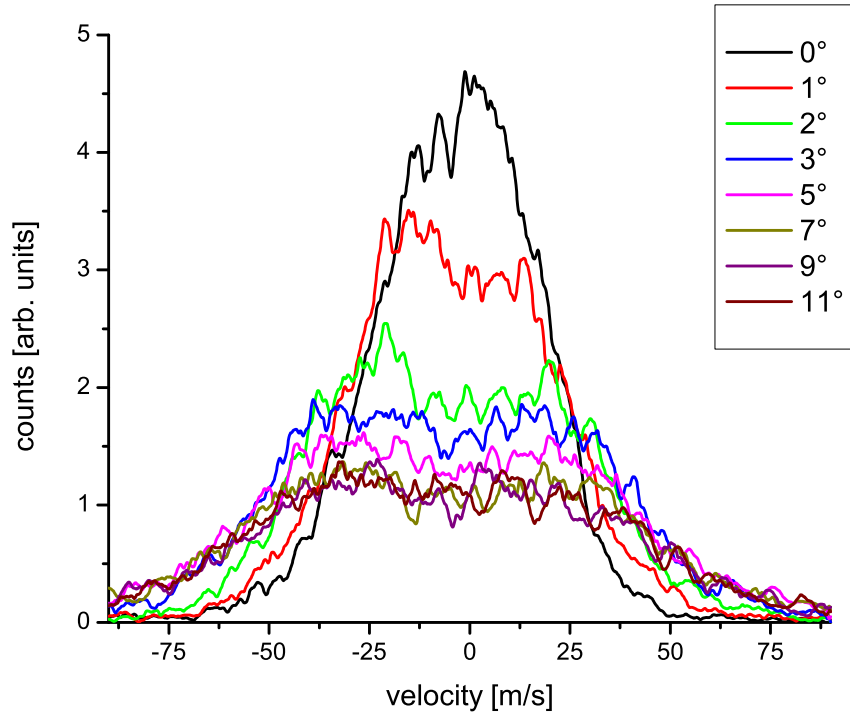


Figure 5.15: Velocity distributions stemming from the standing wave for different rotation angles of the quarter wave plate. These correspond to ellipticities shown in table 5.2 and 5.3. The total energy for each measurement is  $1.8 \text{ mJ}$ .

Figure 5.15 shows the results for a measurement set focused on different ellipticities. This time the laser energy was kept constant. The measurement specified as  $0^\circ$  does not correspond to the centre in degrees between the maxima in Rydberg production mentioned before, but instead was found by systematic measurements with different angles for both quarter wave plates. After finding a minimum length of the observed distribution, both quarter wave plates have been manipulated simultaneously to the angles shown in the figure's legend. Full width at half maximum (FWHM) values are given in table 5.2, which were determined by fitting a Gaussian onto the data. Additionally, theoretical ellipticity values are calculated for the quarter wave plate angles used in the measurements. These values assume the  $0^\circ$  measurement to represent perfect

circular polarisation, which is not the case as mentioned before. However, since the relation between angle and ellipticity is not linear, this approximation was used to give an illustration of the expected ellipticity values. The change of  $\epsilon$  per single degree of quarter wave plate rotation varies between 0.025 and 0.035 in the first  $10^\circ$  away from circular polarisation.

quarter wave plate angle	theoretical ellipticity $\epsilon$	FWHM
$0^\circ$	1	46
$1^\circ$	0.97	59
$2^\circ$	0.93	89
$3^\circ$	0.9	123
$5^\circ$	0.84	138
$7^\circ$	0.78	140
$9^\circ$	0.73	136
$11^\circ$	0.67	140

Table 5.2: FWHM values and ellipticities for the measurements shown in figure 5.15.

A clear trend is visible in the evolution of the distributions width. By detuning the ellipticity away from the optimum, it broadens constantly, which directly translates to higher acquired momentum during the interaction. An upper limit is present which stops the atoms from gaining arbitrary high momentum. This is represented by the fact that the measurements after reaching  $5^\circ$  are nearly identical.

While the deflection measurements follow the predictions with increasing ellipticity, the measurement of the ellipticity itself outside of the vacuum setup displays different results than what the velocity distribution predicts.

The measurement of the ellipticity  $\epsilon$  was performed by recording the minimum and maximum value of laser energy, that passed through the Glan-Taylor prism. This time the prism was rotated and the quarter wave plate was fixed. The measurements were performed directly after the quarter wave plate and before the final multilayer mirror of each beam in the otherwise unaltered beam path. While the mirrors that were used had the specification to reflect all polarisations equally, a change in polarisation, evoked by the mirror, cannot be ruled out with absolute certainty. However, a measurement closer to the vacuum chamber after the last mirror was not possible.

degrees	left side	right side
0°	0.60	0.53
1°	0.61	0.57
2°	0.73	0.61
3°	0.78	0.67
5°	0.85	0.75
7°	0.91	0.80
9°	0.85	0.87
11°	0.75	0.87

Table 5.3:  $\epsilon$  values for the measurements shown in figure 5.15.

As can be seen in table 5.3 the measured difference of the two perpendicular polarisation fractions is bigger in the beginning and becomes smaller for higher angles, which corresponds to light close to circular polarisation, with an exception at the maximum value of 11°. The velocity distribution, however, as well as the expected theoretical behaviour of the quarter wave plates, suggests that the ellipticity value decreases with higher angle for the quarter wave plate. Unfortunately the specific reason for this discrepancy could not be found during the work on this thesis. Since the quarter wave plate angle dependent Rydberg production measurements of each beam provides the angle under which linear polarisation is established inside the chamber very precisely, this before explained method of establishing nearly circularly polarised light was trusted. The expected broadening of the distribution with changing ellipticity supports this assumption strongly.

## 5.4 Semi classical simulation

After the surprising experimental findings a thorough theoretical modelling was needed to shed more light on the process. Therefore, *ab initio* calculations of the standing wave excitation commenced. Two different calculation schemes have been used to investigate this new field configuration. Following the method used before, both calculations were performed using classical trajectories after the tunnelling process. One calculation uses the classical Newton equation with dipole approximation in Coulomb gauge (see page 6). The acceleration in  $z$ -direction is incorporated by including the ponderomotive force acting on the electron after tunnelling. The gradient is given by formula 5.7. The time envelope of the ponderomotive force is given by the decay the two counter-propagating pulses will yield for their combined field, which amounts to

$$\tau_{sw} = \frac{\tau}{\sqrt{2}}, \quad (5.18)$$

where  $\tau$  is the length of the single pulses.

Additionally, a calculation without ponderomotive force in dipole approximation is also performed.

In the second case no artificial force is included, instead the full Lorentz force acting on the ionic core and the single tunnelling electron (see equation 2.36) was used, which also includes the magnetic field component of the laser field. In this case the acceleration appears naturally through the averaging of the forces on both particles over the oscillations of the electromagnetic field.

Using both calculation methods allows on the one hand to obtain a full velocity result not influenced by the expectations of the FTI picture in the full Lorentz case, as well as results relying on a simplified case which has been proven very reliable in strong field tunnelling. Comparing both results yields inside into the applicability of the simple model for more exotic field configurations and possible limitations.

The Lorentz force was calculated from the full electric field of the two pulse process. The electric field of the two counter-propagating pulses in the  $\mathbf{E}_-$  case (see equation 5.6) reads:

$$\begin{aligned} E_x &= F_l e^{-\frac{(ct-z)^2}{c^2\tau^2}} \cos\left[\omega\left(t - \frac{z}{c}\right)\right] + F_r e^{-\frac{(ct+z)^2}{c^2\tau^2}} \cos\left[\omega\left(t + \frac{z}{c}\right)\right] \\ E_y &= F_l \epsilon e^{-\frac{(ct-z)^2}{c^2\tau^2}} \sin\left[\omega\left(t - \frac{z}{c}\right)\right] - F_r \epsilon e^{-\frac{(ct+z)^2}{c^2\tau^2}} \sin\left[\omega\left(t + \frac{z}{c}\right)\right] \\ E_z &= 0 \end{aligned} \quad (5.19)$$

Equal ellipticity was assumed for both beams. The same field is used for the calculations in dipole approximation. To include the full Lorentz force the magnetic field component is calculated with the Maxwell equation

$$\nabla \times \mathbf{E} = \frac{\partial \mathbf{B}}{\partial t}. \quad (5.20)$$

The divergence of the electric field and the magnetic field was tested to be zero, as required in the vacuum.

$$\begin{aligned} \nabla \cdot \mathbf{E} &\stackrel{!}{=} 0 \\ \nabla \cdot \mathbf{B} &\stackrel{!}{=} 0 \end{aligned}$$

With both components now given, the full system of equations can be written down. First the three coordinates of the ionic core, followed by the three coordinates of the active electron.

For easier readability the ionic core coordinates are coloured in red, while the electron coordinates are in blue.

$$\begin{aligned}
 \ddot{X} &+ \frac{X - x}{M\sqrt{(x - X)^2 + (y - Y)^2 + (z - Z)^2}^3} \\
 &- \frac{1}{Mc} e^{-\frac{2(c^2t^2 + Z^2)}{c^2\tau^2}} \left( e^{\frac{(ct+Z)^2}{c^2\tau^2}} F_l \cos \left[ \omega \left( t - \frac{Z}{c} \right) \right] (c - \dot{Z}) \right. \\
 &\quad \left. + e^{\frac{(-ct+Z)^2}{c^2\tau^2}} F_r \cos \left[ \omega \left( t + \frac{Z}{c} \right) \right] (c + \dot{Z}) \right) = 0 \\
 \ddot{Y} &+ \frac{Y - y}{M\sqrt{(x - X)^2 + (y - Y)^2 + (z - Z)^2}^3} \\
 &- \frac{1}{Mc} e^{-\frac{2(c^2t^2 + Z^2)}{c^2\tau^2}} \left( e^{\frac{(ct+Z)^2}{c^2\tau^2}} F_l \epsilon \sin \left[ \omega \left( t - \frac{Z}{c} \right) \right] (c - \dot{Z}) \right. \\
 &\quad \left. - e^{\frac{(-ct+Z)^2}{c^2\tau^2}} F_r \epsilon \sin \left[ \omega \left( t + \frac{Z}{c} \right) \right] (c + \dot{Z}) \right) = 0 \\
 \ddot{Z} &+ \frac{Z - z}{M\sqrt{(x - X)^2 + (y - Y)^2 + (z - Z)^2}^3} \\
 &- \frac{1}{Mc} e^{-\frac{(ct+Z)^2}{c^2\tau^2}} \left\{ e^{\frac{4tZ}{c\tau^2}} F_l \left( \cos \left[ \omega \left( t - \frac{Z}{c} \right) \right] \dot{X} + \epsilon \sin \left[ \omega \left( t - \frac{Z}{c} \right) \right] \dot{Y} \right) \right. \\
 &\quad \left. - F_r \left( \cos \left[ \omega \left( t + \frac{Z}{c} \right) \right] \dot{X} - \epsilon \sin \left[ \omega \left( t + \frac{Z}{c} \right) \right] \dot{Y} \right) \right\} = 0 \\
 \ddot{x} &+ \frac{x - X}{M\sqrt{(x - X)^2 + (y - Y)^2 + (z - Z)^2}^3} \\
 &+ \frac{1}{Mc} e^{-\frac{2(c^2t^2 + z^2)}{c^2\tau^2}} \left( e^{\frac{(ct+z)^2}{c^2\tau^2}} F_l \cos \left[ \omega \left( t - \frac{z}{c} \right) \right] (c - \dot{z}) \right. \\
 &\quad \left. + e^{\frac{(-ct+z)^2}{c^2\tau^2}} F_r \cos \left[ \omega \left( t + \frac{z}{c} \right) \right] (c + \dot{z}) \right) = 0 \\
 \ddot{y} &+ \frac{y - Y}{M\sqrt{(x - X)^2 + (y - Y)^2 + (z - Z)^2}^3} \\
 &+ \frac{1}{Mc} e^{-\frac{2(c^2t^2 + z^2)}{c^2\tau^2}} \left( e^{\frac{(ct+z)^2}{c^2\tau^2}} F_l \epsilon \sin \left[ \omega \left( t - \frac{z}{c} \right) \right] (c - \dot{z}) \right. \\
 &\quad \left. - e^{\frac{(-ct+z)^2}{c^2\tau^2}} F_r \epsilon \sin \left[ \omega \left( t + \frac{z}{c} \right) \right] (c + \dot{z}) \right) = 0 \\
 \ddot{z} &+ \frac{z - Z}{M\sqrt{(x - X)^2 + (y - Y)^2 + (z - Z)^2}^3} \\
 &+ \frac{1}{Mc} e^{-\frac{(ct+z)^2}{c^2\tau^2}} \left\{ e^{\frac{4tz}{c\tau^2}} F_l \left( \cos \left[ \omega \left( t - \frac{z}{c} \right) \right] \dot{x} + \epsilon \sin \left[ \omega \left( t - \frac{z}{c} \right) \right] \dot{y} \right) \right. \\
 &\quad \left. - F_r \left( \cos \left[ \omega \left( t + \frac{z}{c} \right) \right] \dot{x} - \epsilon \sin \left[ \omega \left( t + \frac{z}{c} \right) \right] \dot{y} \right) \right\} = 0
 \end{aligned} \tag{5.21}$$

With this set of coupled differential equations the full simulation of the physical problem after tunnelling is possible. It is important to note that only by fully including the magnetic field component or adding the ponderomotive force manually an acceleration along the  $z$ -axis is reproduced. If one only uses the electric field component no net force would act on the particles in the standing wave.

If the total energy of the electron in the potential of the ionic core is below zero after the laser pulses are gone, a bound atom is formed.

$$\frac{1}{2} \frac{M}{(M+1)} (\dot{\mathbf{R}} - \dot{\mathbf{r}})^2 - \frac{1}{|\mathbf{R} - \mathbf{r}|} \stackrel{!}{<} 0 \quad (5.22)$$

The atoms found by this method are the Rydberg atoms excited and measured in the experiment. The total momentum is calculated by adding the two acquired momenta from the ionic core and the electron. Divided by the combined mass of both parts the final velocity  $v_f$  is retrieved.

$$v_f = \frac{1}{(M+1)} (M\dot{\mathbf{R}} + \dot{\mathbf{r}}) \quad (5.23)$$

Monte Carlo simulations were performed to retrieve the velocity distributions for different standing wave parameters. The NDSolve algorithm included in Mathematica 8 by Wolfram Research Inc. was used to solve the differential equations 5.21 and calculate the final energies and velocities. The starting point in space inside the standing wave was randomised over a full wavelength to include areas with high field strength as well as areas with maximum field gradient. Consequently the same amount of trajectories is started inside the standing wave regardless of the actual field strength. Intermediate results at this stage can unfold details about the influence the different field environments have upon the FTI process, as one can look at it independently from the tunnelling probability.

Afterwards the amount of trajectories at every starting point in space is weighted by the tunnelling probability provided by the ADK theory [7] using the local field strength inside the standing wave. The perpendicular momentum the electron possesses at the tunnel exit was also taken from the ADK theory and randomised for every trajectory. Nine oscillations around the

maximum overlap of the two *cosine* functions have been calculated separately, to shed light on the influence of the starting point in time inside the standing wave, each one deductively also weighted by its tunnelling probability. In contrast to a standing wave with continuous wave lasers, the movement of the two pulses with respect to each other changes the field strength the tunnelled electron experiences. It is different for each of the calculated oscillations, so that the individual weighting is necessary. The intermediate unweighted results that are used for the comparisons between the two calculation methods provide the possibility to look at results starting at different tunnelling times inside the formed standing wave, while the weighted results give distributions that should be comparable to the measurements. Around nine million trajectories are started for every standing wave parameter set.

All calculations were performed for two different ellipticities  $\epsilon = 0.85$  and  $\epsilon = 0.6$ . These values were chosen as typical measured values for the ellipticity present in the experiment (see table 5.3). For comparison it can be stated that an ellipticity of  $\epsilon = 0.85$  corresponds to a quarter wave plate angle of  $4.5^\circ$  detuned from perfect circular polarised light, while  $\epsilon = 0.6$  corresponds to  $14^\circ$ . Also two sets of field strengths have been used. On the one hand a field strength of 0.1, 0.14 and 0.2 *a.u.* per beam and equally strong beams were used, and on the other hand a set with the same values for one of the beams, but only 80% of this field strength in the second beam. For comparison with the experimental data one can recall that  $F = 0.14$  *a.u.* corresponds to a total focus intensity of  $6.9 \cdot 10^{14}$   $W/cm^2$  in the case of linear polarised light.

## Calculation results without ADK weighting

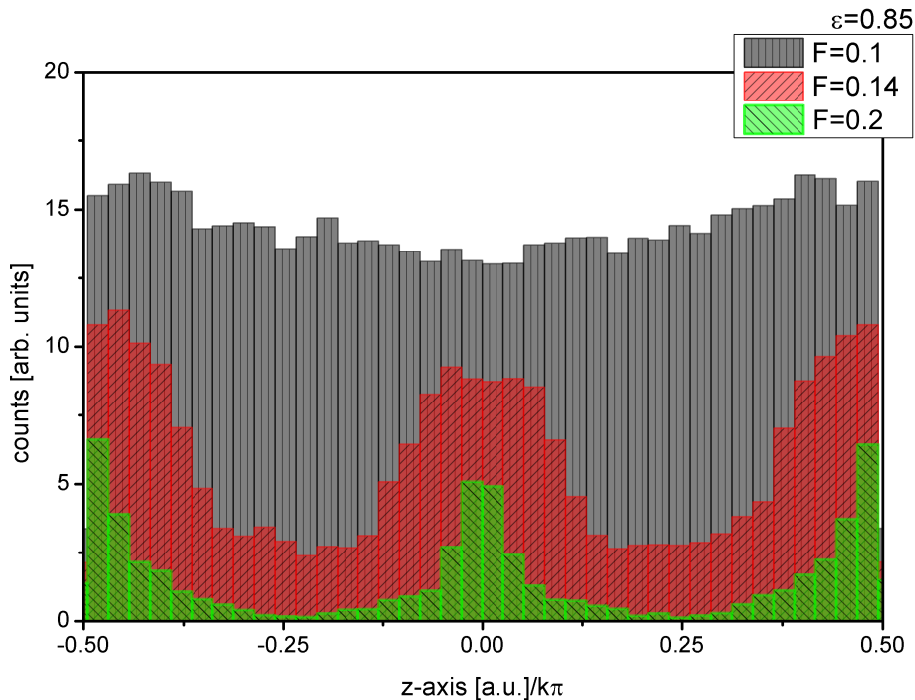


Figure 5.16: Distribution of surviving Rydberg atoms inside the standing wave, dependent on their starting position, for  $\epsilon = 0.85$ . Shown are three different field strengths ( $F$  in  $a.u.$ ) for both beams. 0 on the  $z$ -axis represents the point of maximum field strength but no field gradient,  $\pm 0.25$  represents the points of maximum field gradient, while  $z = \pm 0.5$  are the points of the lowest intensity and no gradient.

Several aspects of the excitation process can be obtained from these calculations. The intermediate results before ADK-weighting represent the probability of a Rydberg atom to survive the standing wave field. For these figures all  $z$ -positions are equally populated. In figure 5.16 the number of bound trajectories depending on the starting point inside the standing wave is shown for the full Lorentz force calculation. The  $z$ -axis extends from minimum to minimum inside the averaged intensity distribution (see figure 5.2) of the standing wave. One can clearly see how the survivability changes from a nearly uniform distribution in the low field strength case  $F = 0.1 a.u.$  to three distinct spikes in the higher field strength cases. At the points of maximum

field gradient  $z = k\pi/4$  dents are rapidly evolving. These are the points where the survivability of neutral atoms decreases the most.

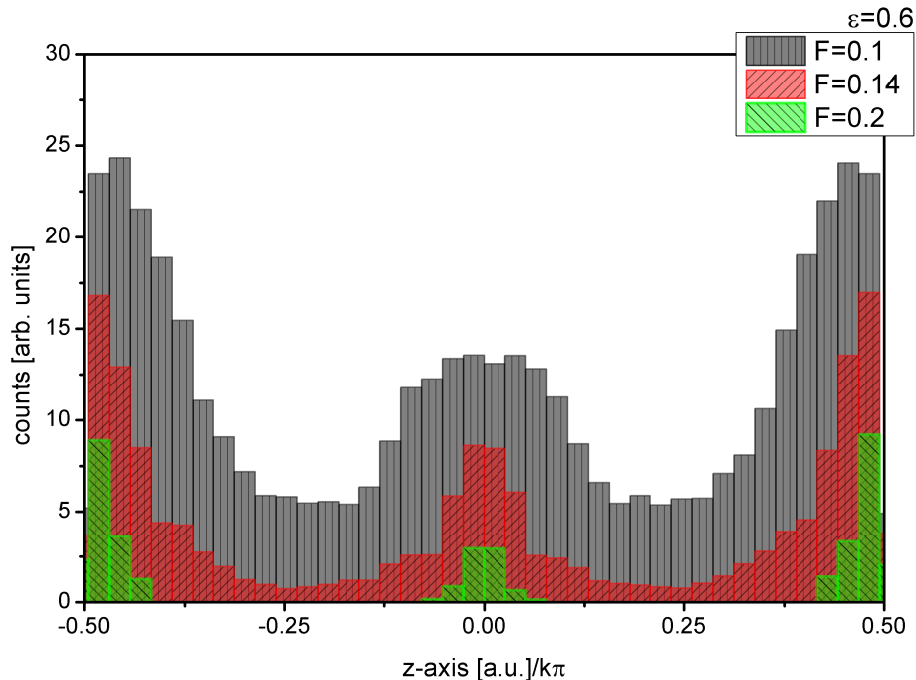


Figure 5.17: Distribution of surviving Rydberg atoms inside the standing wave, dependent on their starting position, for  $\epsilon = 0.6$ . Shown are three different field strengths ( $F$  in  $a.u.$ ) for both beams.

0 on the  $z$ -axis represents the point of maximum field strength but no field gradient,  $\pm 0.25$  represents the points of maximum field gradient, while  $z = \pm 0.5$  are the points of the lowest intensity and no gradient.

Comparing with figure 5.17, which shows the same calculation with higher ellipticity, one can see how this behaviour intensifies until in the  $F = 0.2 a.u.$  case no bound atoms are formed in between the three distinct spikes at the maxima and minima of the intensity distribution along  $z$ . All the calculations shown in figure 5.16 and 5.17 are taken from the point of maximum overlap of the two beams. Taking trajectories starting earlier, which thus interact with the complex field longer, pronounces the dips even further, while late trajectories have a higher survivability due to the shorter interaction and the fact that the electron never experiences the highest field strength.

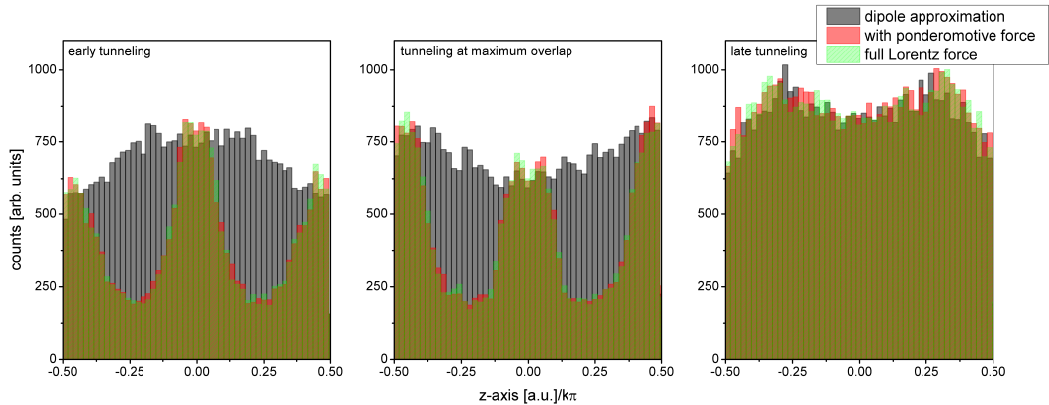


Figure 5.18: Amount of surviving neutral atoms for electrons starting over one wavelength inside the standing wave for low gradient conditions. Shown are three times during the standing wave when tunnelling takes place: 4 oscillations before the maximum overlap on the left, the time of maximum overlap in the middle and 4 oscillations after the maximum overlap on the right. A field strength of  $F = 0.14 \text{ a.u.}$  and an ellipticity of  $\epsilon = 0.85$  was used.

Three different calculations are shown:

Black bars: using only the dipole approximation

Red bars: using the dipole approximation with the addition of the ponderomotive force acting only on the electron

Green bars: using the full Lorentz force acting on both particles

In Figure 5.18 three different graphs are depicted which show how the behaviour changes depending on the time the electron tunnels during the build up and decay of the standing wave. These survival probabilities are calculated for a field strength of  $F = 0.14 \text{ a.u.}$  and an ellipticity of  $\epsilon = 0.85$ . Electrons tunnelling early experience the field for a comparably long time, while electrons tunnelling late never experience the full intensity of the field after their tunnelling. Comparing the results for different times, one can see how the survivability at the field position where the electron experiences the maximum gradient decreases, the longer it has to survive inside this field. Therefore, distinct minima develop at  $z = \pm 0.25$ . This is expected, as the electron is getting more and more drift energy due to the ponderomotive force acting upon it in the laser field. Additionally, this figure also includes all three different calculation schemes used. In the calculation without ponderomotive force, where the electron does not gain energy in the field, the minima are not present. No force is pulling the electron away from the ionic core so that

the binding energy is not reduced. Therefore no minima develop at the points of the maximum gradient. The full Lorentz calculation and the calculation in dipole approximation with ponderomotive force added on the other hand, yield close to identical results for the survivability in all cases. Obviously the ponderomotive force acting on the electron is confirmed to be the major influence the full Lorentz force is introducing compared to the field in dipole approximation.

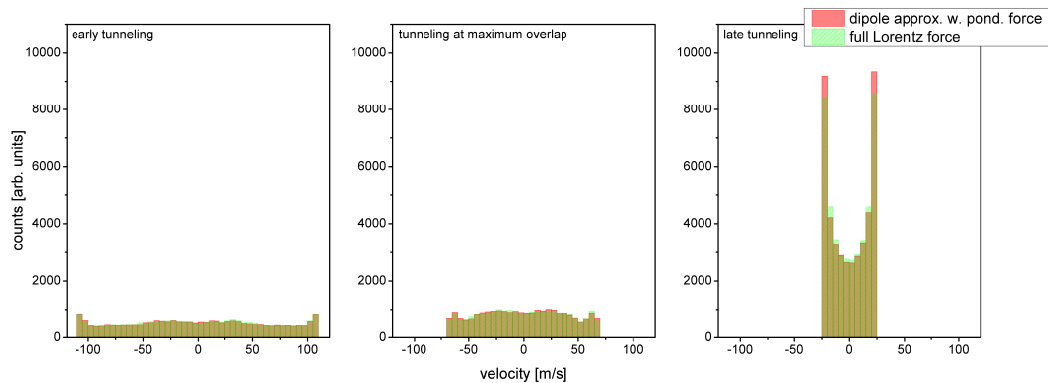


Figure 5.19: Velocity of surviving neutral atoms from the standing wave for low gradient conditions. Shown are three times during the standing wave when tunnelling takes place: 4 oscillations before the maximum overlap on the left, the time of maximum overlap in the middle and 4 oscillations after the maximum overlap on the right. A field strength of  $F = 0.14 \text{ a.u.}$  and an ellipticity of  $\epsilon = 0.85$  was used.

Two different calculations are shown:

Red bars: using the dipole approximation with the addition of the ponderomotive force acting only on the electron

Green bars: using the full Lorentz force acting on both particles

Figure 5.19 shows the centre of mass velocity of the Rydberg atom after the laser pulses are over. For the pure dipole approximation calculation without ponderomotive force no velocity is accumulated at all, therefore, it is not included in the figure. The comparison of the ponderomotive force calculation and the full Lorentz force again reveals a near identical result. In the case of a short interaction with a weaker field, which corresponds to the late tunnelling in the right graph of figure 5.19, the velocity distribution resembles the double spike structure shown in figure 5.3. This is exactly what is expected in a case where no distinct minima are present in the  $z$ -dependent survivability (see

figure 5.18 on the right), as all atoms are accelerated with equal probability just dependent on the gradient in the standing wave. As soon as the gradient becomes too high and the survivability is reduced the shape of the acceleration changes. As can be seen in the early tunnelling calculation the spikes at the far end of the velocity spectrum slowly vanish and a more even distribution is resulting.

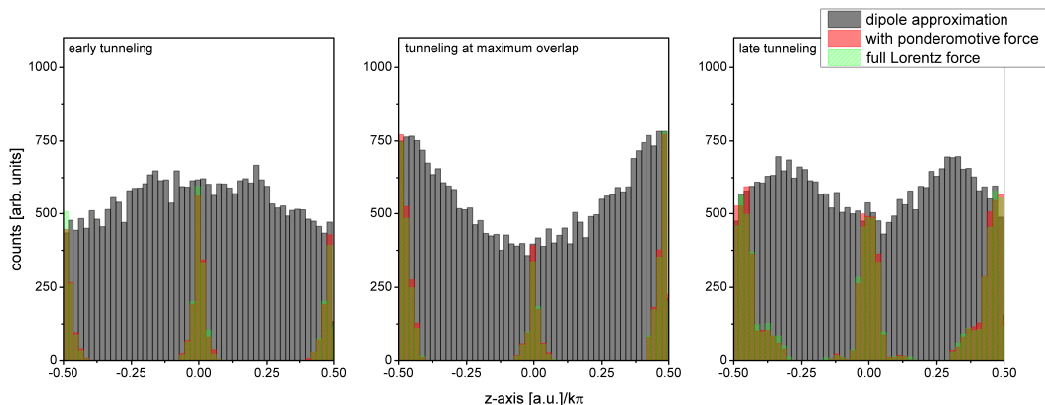


Figure 5.20: Amount of surviving neutral atoms for electrons starting over one wavelength inside the standing wave for high gradient conditions. Shown are three times during the standing wave when tunnelling takes place: 4 oscillations before the maximum overlap on the left, the time of maximum overlap in the middle and 4 oscillations after the maximum overlap on the right. A field strength of  $F = 0.2 \text{ a.u.}$  and an ellipticity of  $\epsilon = 0.6$  was used.

Three different calculations are shown:

Black bars: using only the dipole approximation

Red bars: using the dipole approximation with the addition of the ponderomotive force acting only on the electron

Green bars: using the full Lorentz force acting on both particles

To illustrate the influence the gradient dependent depletion has on the survivability, the most extreme case calculated with a field strength of  $F = 0.2 \text{ a.u.}$  and an ellipticity of  $\epsilon = 0.6$  is shown in figure 5.20 and 5.21.

Again it is immediately obvious that the slowly developing minima in the low gradient case are now severely stronger (see figure 5.17 for comparison). At the points of no field gradient the low drift momentum results in many trajectories which end in a Rydberg state, while the survivability of neutral atoms vanishes in between. Because there exists only a negligible amount of

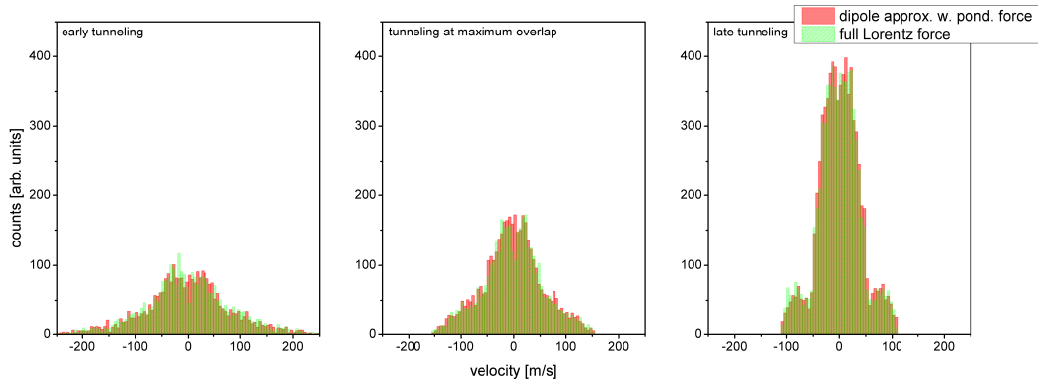


Figure 5.21: Velocity of surviving neutral atoms from the standing wave for high gradient conditions. Shown are three times during the standing wave when tunnelling takes place: 4 oscillations before the maximum overlap on the left, the time of maximum overlap in the middle and 4 oscillations after the maximum overlap on the right. A field strength of  $F = 0.2 \text{ a.u.}$  and an ellipticity of  $\epsilon = 0.6$  was used.

Two different calculations are shown:

Red bars: using the dipole approximation with the addition of the ponderomotive force acting only on the electron

Green bars: using the full Lorentz force acting on both particles

neutral atoms, which acquire high drift momentum, the extreme ends of the velocity distributions are heavily suppressed. The whole shape of the velocity distribution changes into a distribution with a clear maximum around zero velocity, instead of the two peak structure shown before.

When including the tunnelling rate, the atoms originating from the area around  $z = 0$  will be increased even more due to the higher intensity inside the standing wave at this point in space in the elliptical case (see figure 5.2).

Looking at the principal quantum number distribution, depicted in figure 5.22, calculated again using equation 4.2, one can see that no real difference between the distributions with different ellipticities in the area of no field gradient around  $z = 0$  is present. Both distributions are also remarkably similar to the results calculated for a single pulse with different methods (see figure 2.12). Once more no difference was visible between dipole approximation with included ponderomotive force compared to the full Lorentz force, so that only the full Lorentz force results are shown. This again shows, that

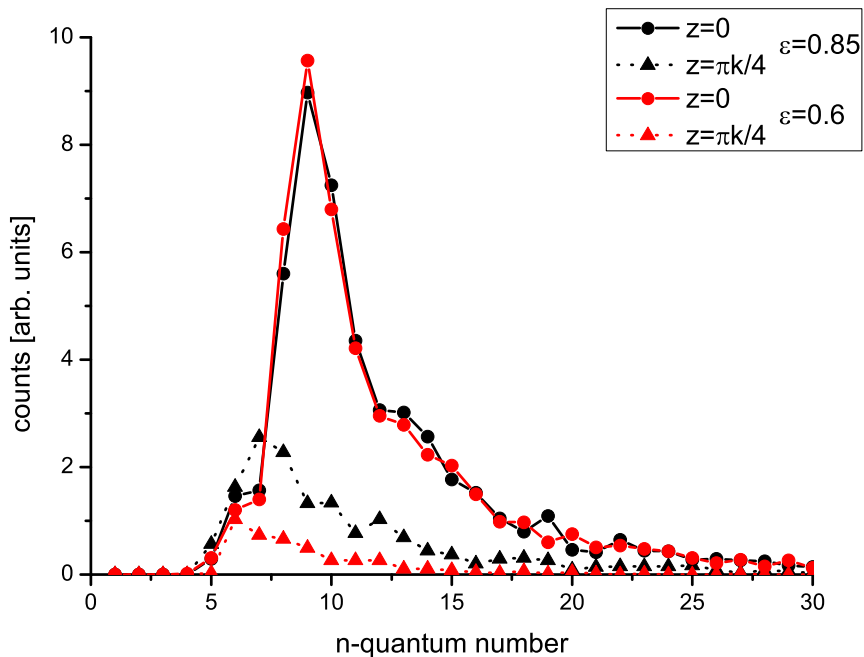


Figure 5.22: Principal quantum number distribution in the standing wave. Calculated for the atoms stemming from the area of maximum intensity  $z = 0$  and atoms stemming from the area of maximum field gradient  $z = \pi k/4$  for two different ellipticities. Equally strong beams with a field strength of  $F = 0.14$  *a.u.* were used.

the fundamental process of frustrated tunnelling still holds true in this more complex field configuration. At  $z = \pi k/4$ , where a high field gradient acts on the electrons, the distributions change, but no obvious redistribution is visible. For both ellipticities states with  $n > 7$  are severely suppressed. However, the reduction in the  $\epsilon = 0.6$  case is greater, which is expected due to the higher gradient. This is in accord with the minima visible in figure 5.16 and 5.17.

Recalling the fact that the gradient is also responsible for the acceleration of the neutral atoms, one can now understand the delicate interplay between survivability and acceleration, which limits the maximum deflection in the experiment. Because of this interplay the velocity distributions do not follow a simple broadening during the change of one parameter.

## Calculation results with ADK weighting

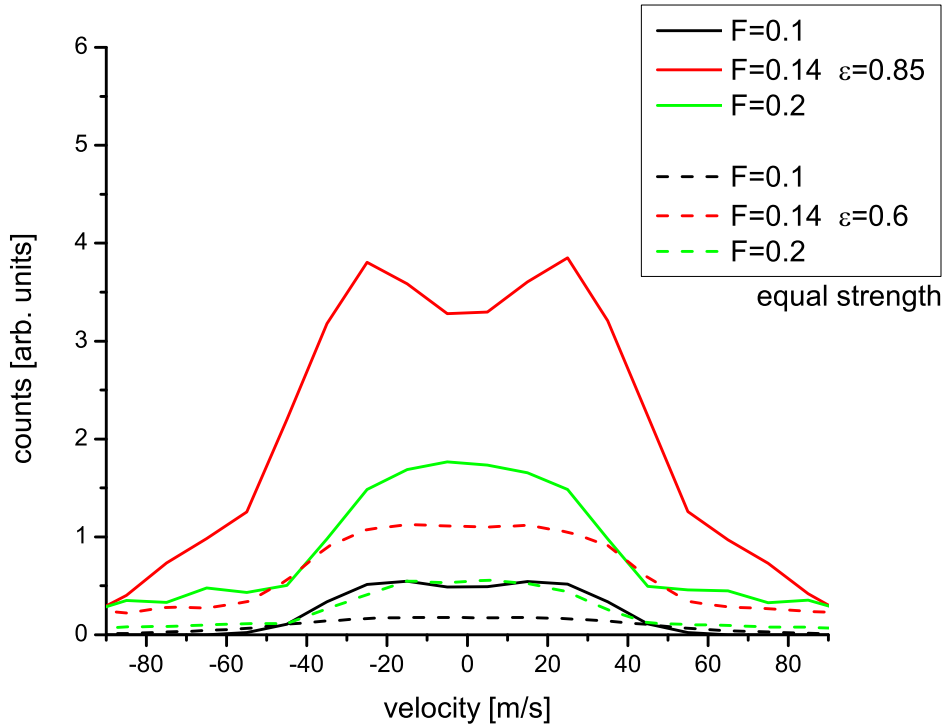


Figure 5.23: Calculated velocity distribution including ADK weighting stemming from the standing wave for two equally strong beams.

Shown are three different field strengths ( $F$  in *a.u.*) for both beams. The solid lines show results for an ellipticity of  $\epsilon = 0.85$ , while the dashed lines show results for calculations using  $\epsilon = 0.6$ .

The full results including ADK weighting for two equally strong beams are shown in figure 5.23. In the  $\epsilon = 0.85$  case the structure broadens from the lowest field strength  $F = 0.1$  *a.u.* to the intermediate field strength  $F = 0.14$  *a.u.*, while for the highest field strength  $F = 0.2$  *a.u.* the main peak is smaller again. Additionally, the total amount of atoms surviving is severely decreased. However, there are some wider features visible in this case which do extend further than for the lower field strength case. The calculations for  $\epsilon = 0.6$  show rather similar results for the two lower intensity cases. The main peak in the velocity distribution is almost identical, only the drop off on the corners of the distribution has a different slope. The high field strength case

again shows a distinct drop in overall survivability and an even smaller width in the central main structure of accelerated atoms.

The calculations show quite a few features that were also seen during the experiment. The double peak structure, that was clearly visible in figure 5.12, is directly reproduced in the calculation. This structure also vanishes for higher gradients, which it also did in the measurement. Additionally, as observed in the experiment, the highest intensity displays a smaller absolute number of detected excited neutral atoms.

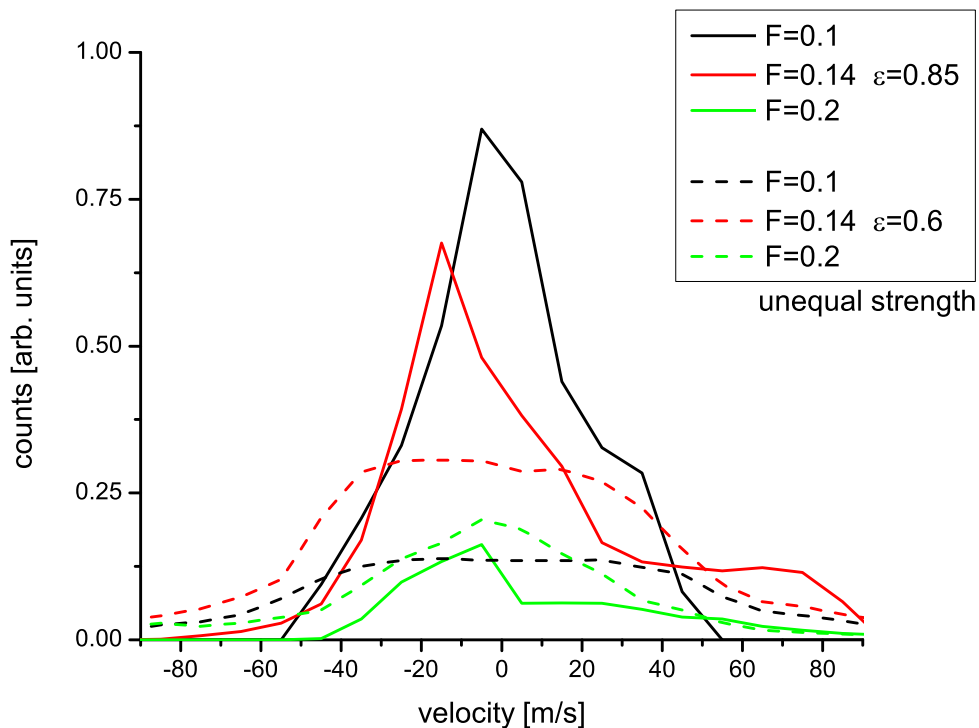


Figure 5.24: Calculated velocity distribution including ADK weighting stemming from the standing wave for two differently strong beams. One beam has the shown field strength ( $F$  in *a.u.*), while the other one is reduced to 80% of the value. The solid lines show results for an ellipticity of  $\epsilon = 0.85$ , while the dashed lines show results for calculations using  $\epsilon = 0.6$ .

Figure 5.24 shows the full results with ADK weighting for two differently strong beams. All other parameters have been kept constant. A strong imbalance is visible between the two sides. The imbalance visible in the

1.8 mJ measurement of figure 5.12, while a lot smaller, could be attributed to different intensities in the two beams. As mentioned before, due to the used beam splitter, the two beams were not split equally. However, because of the different focus spot sizes this difference was compensated when comparing the final focus intensity. Interestingly, the strong imbalance in the  $\epsilon = 0.85$  case of the calculation is almost gone for the other ellipticity of  $\epsilon = 0.6$ . In the measurements a strong imbalance is only truly visible for one energy specific measurement. With a different pulse energy it disappeared.

## 5.5 Conclusion

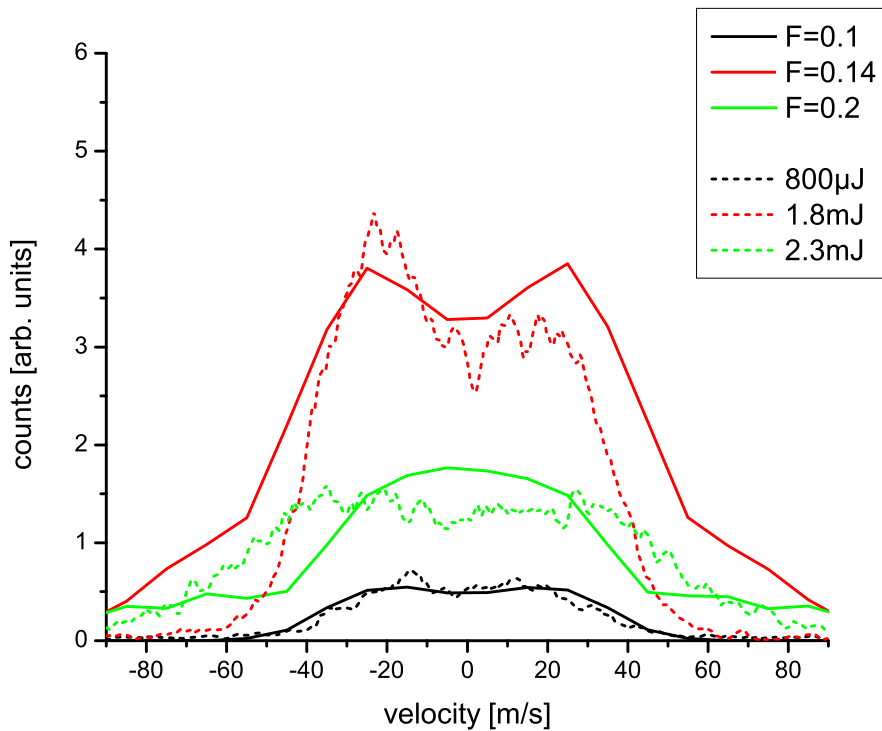


Figure 5.25: Comparison between the full calculation and corresponding measurements.

Solid lines represent the calculation with equally strong beams with a field strengths  $F$  in *a.u.* and an ellipticity of  $\epsilon = 0.85$ , while dashed lines represent measurements of the velocity distribution with given total laser energies before the beamsplitter.

Figure 5.25 finally shows the comparison of the measurements performed with different energies (see figure 5.12) to the calculated velocity distributions obtained with equally strong counter-propagating laser pulses and an ellipticity of  $\epsilon = 0.85$ . While the calculations do not reproduce the measurements exactly, which can be attributed mainly to the limited knowledge of the actual standing wave properties, the agreement is still very good. High effort went into establishing a stable standing wave, but some experimental limitations could not be set aside. The adjustment of the overlap of the two beams had to be performed under atmospheric pressure and the measurement chamber had to be pumped afterwards which could introduce a slight change in the properties of the entrance windows. While an overlap of the two beams could be ensured during all measurements due to the background free measurement method, which relied on two elliptical pulses, the actual amount of overlap could have been unlike for different measurements. Since the quarter wave plates in the beam path had to be rotated, they could also introduce a very slight lateral displacement. It would not change the position of a single focus noticeably, but the properties of the formed standing wave could be altered due to a slight wavefront mismatch.

Nevertheless, for the low energy case the agreement between measurement and calculation is excellent. The width of the distribution, representing the maximum velocity, is very well reproduced. Additionally, the drop off of the distribution follows the calculated shape nicely.

In the medium energy case the calculation exhibits a double hump structure, which is also present in the measurement. The calculated drop off at high velocities is less steep than the measured distribution. A slight difference between the two humps is visible in the measurement, which hints at slightly different energies in the two beams. This was tested by calculating the standing wave acceleration with differently strong beams. As shown in figure 5.24 the distribution can change dramatically in this case, which can also lead to a slightly steeper drop off at maximum velocity.

The peak in the high energy distribution is distinctly broader than the calculation. But it also shows a higher amount of high velocity Rydberg atoms. Smoothing the steep drop off would yield a distribution similar to the measured data.

Several key aspects of the measurements could be reproduced in the calculations and the measured maximum velocity fits nicely to the calculated distributions.

Ultimately, a deeper understanding of the excitation and acceleration process has been reached. While in case of normal laser focusses the gradient acceleration in the simplified picture grants excellent results for comparison with the experiment and characterisation of the focus properties, the standing wave case differs. The extreme field gradients, which are present here, ultimately limit the maximum achievable velocity possible with a one step acceleration. However, even in this very complex field configuration composed of counter-propagating elliptical pulses the classic trajectory calculation yields very good results.

Additionally, it was found that the ponderomotive force acting on the tunnelled electron is the essential force influencing the trajectories of the electron after tunnelling. This could be established due to the fact that the calculations in dipole approximation, with the inclusion of the ponderomotive force on the electron, yield identical results to the calculations with the full Lorentz force, for all measurable observables concentrated on in the extent of this research.

## 6 Summary

The goal of this thesis was the investigation of the momentum that is imparted on neutral atoms due to the ponderomotive force in the strong field regime. So far only single pulses have been used to excite Rydberg atoms and accelerate them at the same time. Here, two pulses were used to form more complex field configurations, where the magnetic field component becomes important. While it is constantly weak compared to the electric field component in a travelling wave, in a standing wave there are places where the magnetic field is the main influence on the interaction.

Several discoveries have been made throughout the research. Firstly, the process of frustrated tunnelling ionisation (FTI) itself was reviewed. It can be understood as an extension of the three-step model of strong field interaction. When including the Coulomb field after tunnelling, its influence on electrons can alter the interaction process. Especially electrons which gain low energy in the laser field cannot leave the Coulomb potential of the ion. Therefore, they stay bound to it after the laser pulse is over and one ends with a neutral atom in an excited state. If ionisation or excitation of the atom was triggered by the strong electromagnetic field can only be determined after the field itself is switched off. Therefore, in contrast to the classical three-step model which neglects the Coulomb influence after tunnelling, tunnelling rates of an atom in the laser field do not equal ionisation rates of the atom. The FTI process represents an additional excitation channel in the strong field regime.

Trajectory calculations done in the extent of this thesis show that the Coulomb interaction decisively influences the electron trajectory from directly after the moment of tunnelling on. While the immediate movement is indeed dominated by the much stronger laser field, the averaged trajectory of most FTI electrons already follows the final Rydberg orbit that the electron is left in after the

laser field is switched off. Therefore, when looking at the long term evolution of tunnelled electrons in high fields, it is highly advised to include the Coulomb potential of the parent ion.

The experimental pump-probe setup allowed to expose the helium Rydberg atoms, that are produced during the FTI process, to another strong laser field. Although the electron is only very weakly bound, the Rydberg atoms are astonishingly resistant against subsequent ionisation. The measured acceleration, that occurs during the FTI process, is also present for the already prepared Rydberg atoms and, therefore, contains directly the intensity the Rydberg atoms have been exposed to. With the help of different polarised beams it was possible for the first time to ensure that the Rydberg atoms that are observed did in fact interact with almost the full intensity of the second laser beam. A high survival rate of 73% is measured which fits to a calculated survival rate of 61%. Classical trajectory calculations visualise the reason for the high resistance against ionisation. In case of Rydberg orbits the electron spends a proportionally large time far away from the ionic core, which implies that, when the second short laser pulse interacts with the atom, it is likely that the electron is not close to the core region. Therefore, the "quasi-free" electron is not substantially altered and remains in its energy state. Only when the electron is close to the core region during the interaction with the second laser an ionisation is possible. The calculations performed of the two laser pulse process exhibit a very distinctive dip in the survival rate for exactly the Rydberg orbits whose round-trip times match the time delay between the two pulses.

In a modified setup the high survival rate in conjunction with the acceleration was utilised to steer neutral atoms selectively. The two laser foci of the subsequent pulses were adjusted very precisely in space with respect to each other. A clear deflection in both directions is accomplished and the performed Monte-Carlo simulation exhibits an excellent agreement with the measurements. An additional calculation using a higher intensity shows an even stronger deflection and displays the scalability of the setup. A possible multi step setup could also provide even higher selective control over neutral atoms.

---

The explanation of the observed acceleration based on the gradient due to the focussing of a laser beam has been extremely successful in the first observation in [68] and in utilising it in the two pulse setup presented here. Therefore, exploring its limits with even higher gradients was the intent for the second part of the thesis. By realising a standing wave in the femtosecond time domain, a very different electromagnetic field could be realised in the laboratory, while still maintaining the high intensity needed to apply the tunnelling theory. A deliberate change in the ellipticity of the two laser pulses allowed for a changeable electric field gradient along the laser axis and a background free measurement of Rydberg atoms stemming purely from the overlap region, where the standing wave develops. This enabled the observation of the Kapitza-Dirac effect for neutral atoms in a high intensity field for the first time.

To simulate the results *ab initio* Monte-Carlo simulations utilising different approximations have been performed. Calculations with the laser field included purely in dipole approximation do not produce the observed acceleration along the laser propagation axis. By including the ponderomotive force only acting on the tunnelled electron, results which are nearly indistinguishable from calculations employing the full Lorentz force have been produced. Therefore, it can be concluded that even in more complex fields, where areas of pure magnetic field are present, and the field strength changes on the wavelength scale, the dipole approximation can still yield applicable results, if one includes averaged forces as e.g. the ponderomotive force. The simulation exhibits many of the characteristic features found in the measurements, and gives insight into the survival of neutral atoms. It can be concluded that a delicate interplay between the gradient force and the dynamics in the field limit the maximum velocity that a neutral atom can obtain during a femtosecond laser pulse, which is confirmed in the experimental observation.



# Appendix

One can have a look at the full Hamiltonian of the tunnelled electron and the ionic core in comparison to the reduced mass system to extract the components which cause the additional acceleration.

To accomplish this the full Hamiltonian has to be separated into two parts, one for the reduced mass and one for the centre of mass:

$$\hat{H}(r_1, r_2, p_1, p_2) = \hat{H}_{red}(r, p) + \hat{H}_{cm}(R, P) \quad (\text{A.1})$$

The new coordinates are defined as

$$\begin{aligned} r &= r_1 - r_2 \\ R &= \frac{m_1 r_1 + m_2 r_2}{m_1 + m_2} \\ p &= \frac{m_2 p_1 - m_1 p_2}{m_1 + m_2} \\ P &= p_1 + p_2 \end{aligned} \quad (\text{A.2})$$

and the additional relations for the reduced mass  $\mu$  and the combined mass  $M$  are given by

$$\begin{aligned} \mu &= \frac{m_1 m_2}{m_1 + m_2} \\ M &= m_1 + m_2 \end{aligned} \quad (\text{A.3})$$

Without loss of generality all coordinates with 1 denote the ionic core and 2 the single active electron.

The Hamiltonian for the reduced mass reads

$$\hat{H}_{red} = \frac{1}{2\mu} (\mathbf{p} + q\mathbf{A})^2 \quad (\text{A.4})$$

where  $q$  denotes the charge.

Expanding equation A.4 yields:

$$\hat{H}_{red} = \frac{1}{2\mu} \left( \underbrace{p^2}_a - \underbrace{2q\mathbf{A} \cdot \mathbf{p}}_b + \underbrace{q^2 A^2}_c \right) \quad (\text{A.5})$$

Parts a-c can now be identified inside the full 2 body Hamiltonian, which is given by adding the Hamiltonian of the ionic core and the active electron

$$\begin{aligned} \hat{H} &= \frac{(\mathbf{p}_1 + q_1 \mathbf{A}_1)^2}{2m_1} + \frac{(\mathbf{p}_2 + q_2 \mathbf{A}_2)^2}{2m_2} \\ &= \underbrace{\frac{p_1^2}{2m_1}}_1 + \underbrace{\frac{q_1 \mathbf{A}_1 \cdot \mathbf{p}_1}{m_1}}_2 + \underbrace{\frac{q_1^2 A_1^2}{2m_1}}_3 + \underbrace{\frac{p_2^2}{2m_2}}_4 + \underbrace{\frac{q_2 \mathbf{A}_2 \cdot \mathbf{p}_2}{m_2}}_5 + \underbrace{\frac{q_2^2 A_2^2}{2m_2}}_6. \end{aligned} \quad (\text{A.6})$$

Parts 1 and 4 can be combined into the expressions for the reduced and combined mass

$$\begin{aligned} \frac{p_1^2}{2m_1} + \frac{p_2^2}{2m_2} &= \frac{p_1^2(m_1 + m_2)}{2m_1(m_1 + m_2)} + \frac{p_2^2(m_1 + m_2)}{2m_2(m_1 + m_2)} \\ &= \frac{1}{2M} \left( \frac{m_2}{m_1} p_1^2 + \frac{m_1}{m_2} p_2^2 + p_1^2 + p_2^2 \right) \\ &= \frac{1}{2M} \left( \frac{m_2^2}{m_1 m_2} p_1^2 + \frac{m_1^2}{m_1 m_2} p_2^2 - \frac{2m_1 m_2 p_1 p_2}{m_1 m_2} \right) + \frac{1}{2M} (p_1^2 + p_2^2 + 2p_1 p_2) \\ &= \frac{1}{2\mu} (m_2^2 p_1^2 + m_1^2 p_2^2 - 2m_1 m_2 p_1 p_2) + \frac{1}{2M} (p_1^2 + p_2^2 + 2p_1 p_2) \\ &= \frac{p^2}{2\mu} + \frac{P^2}{2M} \end{aligned}$$

whose first part corresponds to the term a in equation A.5.

For the remaining parts a magnetic vector potential has to be defined. It can be calculated from the electric field of the standing wave (see equation 5.2) by integration.

$$\mathbf{E}(\mathbf{r}, t) = 2F \cos(\omega t) \cos(k\mathbf{r}) \quad (\text{A.7})$$

$$\mathbf{A}(\mathbf{r}, t) = 2 \frac{F}{\omega} \cos(k\mathbf{r}) \sin(\omega t) \cdot f(t) \quad (\text{A.8})$$

To simplify the following formulas all factors independent of  $\mathbf{r}$  have been combined into the factor  $A_x$ .

$$\mathbf{A}(\mathbf{r}, t) = A_x(t) \cos(k\mathbf{r}) \quad (\text{A.9})$$

Parts 2 and 5 are investigated and  $\mathbf{A}$  is inserted. Additionally the single charge  $q_1$  and  $q_2$  of electron and ionic core are inserted.

$$\begin{aligned} \frac{q_1 \mathbf{A}_1 \cdot \mathbf{p}_1}{m_1} + \frac{q_2 \mathbf{A}_2 \cdot \mathbf{p}_2}{m_2} &= e \left( \frac{m_2 \mathbf{A}_1 \cdot \mathbf{p}_1 - m_1 \mathbf{A}_2 \cdot \mathbf{p}_2}{m_1 m_2} \right) \\ &= \frac{e A_x}{m_1 m_2} [m_2 \mathbf{p}_1 \cos(k\mathbf{r}_1) - m_1 \mathbf{p}_2 \cos(k\mathbf{r}_2)] \end{aligned}$$

The following approximations have been used for the two coordinates:

$$\begin{aligned} \mathbf{R} &= \frac{m_1 \mathbf{r}_1 + m_2 \mathbf{r}_2}{m_1 + m_2} = \underbrace{\frac{m_1}{m_1 + m_2}}_{\cong 1} \left( \mathbf{r}_1 + \underbrace{\frac{m_2}{m_1}}_{\cong 0} \mathbf{r}_2 \right) \\ &\implies \mathbf{r}_1 \cong \mathbf{R} \\ \mathbf{r} &= \mathbf{r}_1 - \mathbf{r}_2 \cong \mathbf{R} - \mathbf{r}_2 \\ &\implies \mathbf{r}_2 \cong \mathbf{R} - \mathbf{r} \end{aligned} \quad (\text{A.10})$$

Now the field can be rewritten in the form:

$$\frac{e A_x}{m_1 m_2} (m_2 \mathbf{p}_1 \cos(k\mathbf{R}) - m_1 \mathbf{p}_2 \cos(k\mathbf{R} - k\mathbf{r}))$$

With the trigonometric identity

$$\cos(x \pm y) = \cos(x) \cos(y) \mp \sin(x) \sin(y) \quad (\text{A.11})$$

one can simplify further in the direct vicinity of the ionic core

$$\cos(k\mathbf{R} - k\mathbf{r}) \stackrel{r \approx 0}{\cong} \cos(k\mathbf{R}) \underbrace{\cos(k\mathbf{r})}_{=1} + \sin(k\mathbf{R}) \underbrace{\sin(k\mathbf{r})}_{=0+k\mathbf{r}}$$

which finally yields

$$\begin{aligned} & \frac{eA_x}{m_1 m_2} [(m_2 \mathbf{p}_1 - m_1 \mathbf{p}_2) \cos(k\mathbf{R})] - \frac{eA_x}{m_2} \mathbf{p}_2 k\mathbf{r} \sin(k\mathbf{R}) \\ \implies & \frac{eA_x}{\mu} \mathbf{p} \cos(k\mathbf{R}) - \frac{eA_x}{m_2} \mathbf{p}_2 k\mathbf{r} \sin(k\mathbf{R}) \end{aligned} \quad (\text{A.12})$$

While the first term can be identified with the b term in the reduced mass system, the second term cannot. It still depends on  $\mathbf{p}_2$  and, therefore, it represents the first addition the electron experiences in the standing wave.

The same procedure is executed for parts 3 and 6.

$$\begin{aligned} \frac{q_1^2 A_1^2}{2m_1} + \frac{q_2^2 A_2^2}{2m_2} &= \frac{e^2 A_x^2}{2} \left[ \frac{\cos^2(k\mathbf{r}_1)}{m_1} + \frac{\cos^2(k\mathbf{r}_2)}{m_2} \right] \\ &= \frac{e^2 A_x^2}{2m_1 m_2} [m_2 \cos^2(k\mathbf{r}_1) + m_1 \cos^2(k\mathbf{r}_2)] \end{aligned}$$

Using the coordinate substitution from before (see equation A.10) yields:

$$\frac{e^2 A_x^2}{2m_1 m_2} [m_2 \cos^2(k\mathbf{R}) + m_1 \cos^2(k\mathbf{R} - k\mathbf{r})]$$

With the trigonometric identity from before (equation A.11) and

$$\cos^2(x) = \frac{1}{2} [1 + \cos(2x)] \quad (\text{A.13})$$

one can again simplify further in the direct vicinity of the ionic core

$$\begin{aligned} \cos^2(k\mathbf{R}) &= \frac{1}{2} [1 + \cos(2k\mathbf{R})] \\ \cos^2(k\mathbf{R} - k\mathbf{r}) &= \frac{1}{2} [1 + \cos(2k\mathbf{R} - 2k\mathbf{r})] \\ &\stackrel{\mathbf{r} \approx 0}{\approx} \frac{1}{2} \left[ 1 + \underbrace{\cos(2k\mathbf{R})}_{=1} + \underbrace{\sin(2k\mathbf{R})}_{=0+2k\mathbf{r}} \underbrace{\sin(2k\mathbf{r})}_{=0+2k\mathbf{r}} \right] \end{aligned}$$

which yields

$$\frac{e^2 A_x^2}{4m_1 m_2} [m_2 + m_2 \cos(2k\mathbf{R}) + m_1 + m_1 \cos(2k\mathbf{R}) + 2m_1 k\mathbf{r} \sin(2k\mathbf{R})]$$

---

Factorising and simplifying leads to

$$\begin{aligned}
& \frac{e^2 A_x^2}{4m_1 m_2} [m_1 + m_2 + (m_1 + m_2) \cos(2k\mathbf{R}) + 2m_1 k\mathbf{r} \sin(2k\mathbf{R})] \\
& \implies \frac{e^2 A_x^2}{4\mu} [1 + \cos(2k\mathbf{R})] + \frac{e^2 A_x^2}{2m_2} k\mathbf{r} \sin(2k\mathbf{R}) \quad (\text{A.14}) \\
& \implies \frac{e^2 A_x^2}{2\mu} \cos^2(k\mathbf{R}) + \frac{e^2 A_x^2}{2m_2} k\mathbf{r} \sin(2k\mathbf{R})
\end{aligned}$$

Once more the first term can be directly identified with the term  $c$  in the reduced mass system, while the second term is another addition inside the standing wave.

The two expressions

$$f_1 = -\frac{eA_x}{m_2} \mathbf{p}_2 k\mathbf{r} \sin(k\mathbf{R}) \quad (\text{A.15})$$

$$f_2 = +\frac{e^2 A_x^2}{2m_2} k\mathbf{r} \sin(2k\mathbf{R}) \quad (\text{A.16})$$

have been identified to be the additional terms stemming from the standing wave.



# List of Figures

2.1	Photo ionisation and multiphoton ionisation . . . . .	7
2.2	Photoelectron energy spectrum of ATI-peaks with different pulse energies . . . . .	8
2.3	Observation of the plateau region of different noble gases . . . . .	9
2.4	Tunnel ionisation at lower field strength and ABI at high field strength . . . . .	10
2.5	Three-step model . . . . .	11
2.6	Ellipticity dependence of Rydberg survival . . . . .	12
2.7	Electron trajectories for different ionisation times . . . . .	13
2.8	Sketch of a $\Lambda$ -transition in a Rydberg atom . . . . .	15
2.9	Energy levels of the potassium atom during a strong laser pulse	16
2.10	Map of electrons which end in an excited state after tunnelling .	19
2.11	Trajectories of FTI electrons . . . . .	20
2.12	$n$ quantum number distribution . . . . .	21
3.1	Neutral particle detection method . . . . .	25
3.2	Maxwell-Boltzmann distribution of helium atoms moving towards the detector . . . . .	26
3.3	Vacuum chamber . . . . .	29
3.4	Acceleration setup . . . . .	32
3.5	Standing wave setup . . . . .	34
3.6	Width of the laser beams along the focus measured with the knife edge method . . . . .	37
4.1	Additional acceleration imparted on Rydberg atoms . . . . .	40
4.2	Trajectories for double pulse experiment part 1 . . . . .	42
4.3	Trajectories for double pulse experiment part 2 . . . . .	43
4.4	Trajectories for double pulse experiment part 3 . . . . .	44

4.5	$n$ -distribution of He atoms after strong-field interaction . . . . .	45
4.6	$n$ selective survival probability of He Rydberg atoms . . . . .	47
4.7	Vector plots of the momentum imparted on the atoms . . . . .	50
4.8	Experimental and theoretical neutral atom distribution on the detector . . . . .	51
4.9	Cuts through the density distributions at the focal plane . . . . .	52
5.1	Intensity distribution for cycle averaged standing wave . . . . .	58
5.2	Intensity distribution for cycle averaged standing wave in a slightly mismatched case . . . . .	59
5.3	Velocity distribution of neutral atoms accelerated by the stand- ing wave for exactly half the laser pulse . . . . .	60
5.4	Velocity distribution of neutral atoms accelerated by the stand- ing wave for a random time which follows a normal distribution around half the laser pulse length . . . . .	61
5.5	Velocity distribution calculated with the simplified quantum mechanical model . . . . .	63
5.6	Typical detector image for the standing wave . . . . .	64
5.7	Additional detector images from different field configurations . . . . .	65
5.8	Comparison of the velocity distributions of three different noble gases . . . . .	67
5.9	Perpendicular velocity stemming from the focus gradient of the standing wave for different total laser energies . . . . .	70
5.10	Initial velocity distributions stemming from the standing wave for different total laser energies . . . . .	71
5.11	Comparison of measured velocity distribution and the simple theoretical explanation . . . . .	72
5.12	Final velocity distributions stemming from the standing wave for different total laser energies . . . . .	73
5.13	Measured polarisation characteristics for all used laser intensi- ties of the weaker beam . . . . .	75
5.14	Measured polarisation characteristics for all used laser intensi- ties of the stronger beam . . . . .	76
5.15	Velocity distributions stemming from the standing wave for different rotation angles of the quarter wave plate . . . . .	77

5.16 Distribution of surviving Rydberg atoms inside the standing wave, dependent on their starting position, for $\epsilon = 0.85$ . . . . .	85
5.17 Distribution of surviving Rydberg atoms inside the standing wave, dependent on their starting position, for $\epsilon = 0.6$ . . . . .	86
5.18 Amount of surviving neutral atoms for electrons starting over one wavelength inside the standing wave for low gradient conditions . . . . .	87
5.19 Velocity of surviving neutral atoms from the standing wave for low gradient conditions . . . . .	88
5.20 Amount of surviving neutral atoms for electrons starting over one wavelength inside the standing wave for high gradient conditions . . . . .	89
5.21 Velocity of surviving neutral atoms from the standing wave for high gradient conditions . . . . .	90
5.22 Principal quantum number distribution in the standing wave . .	91
5.23 Calculated velocity distribution including ADK weighting stemming from the standing wave for two equally strong beams . . .	92
5.24 Calculated velocity distribution including ADK weighting stemming from the standing wave for two differently strong beams .	93
5.25 Comparison between the full calculation and corresponding measurements . . . . .	94



# Bibliography

- [1] A. Einstein, Ann. d. Phy. **17**, 132 (1905).
- [2] M. GÄüppert-Mayer, Ann. d. Phy. **401**, 273 (1931).
- [3] G. S. Voronov and N. B. Delone, Sov. Phys. JETP **23**, 54 (1966).
- [4] P. Agostini, F. Fabre, G. Mainfray, and N. K. Rahman, Phys. Rev. Lett. **42**, 1127 (1979).
- [5] L. V. Keldysh, Sov. Phys. JETP **20**, 1307 (1965).
- [6] A. M. Perelomov, V. S. Popov, and M. V. Terentev, Sov. Phys. JETP **23**, 924 (1966).
- [7] N. N. Delone, M. V. Ammosov, and V. P. Krainov, Sov. Phys. JETP **64**, 1191 (1986).
- [8] S. F. J. Laroche, A. Talebpour, and S. L. Chin, J. Phys. B: At. Mol. Opt. Phys. **31**, 1215 (1998).
- [9] G. G. Paulus *et al.*, Phys. Rev. Lett. **72**, 2851 (1994).
- [10] X. F. Li *et al.*, Phys. Rev. A **39**, 5751 (1989).
- [11] K. J. Schafer, B. Yang, L. F. DiMauro, and K. C. Kulander, Phys. Rev. Lett. **70**, 1599 (1993).
- [12] M. Y. Kuchiev, JETP Letters **45**, 404 (1987).
- [13] G. L. Yudin and M. Y. Ivanov, Phys. Rev. A **63**, 033404 (2001).
- [14] T. Nubbemeyer *et al.*, Phys. Rev. Lett. **101**, 233001 (2008).
- [15] W. C. Henneberger, Phys. Rev. Lett. **21**, 838 (1968).

- [16] M. Pont, N. R. Walet, M. Gavrilu, and C. W. McCurdy, *Phys. Rev. Lett.* **61**, 939 (1988).
- [17] J. H. Eberly and K. C. Kulander, *Science* **262**, 1229 (1993).
- [18] M. Gavrilu, *Journal of Physics B: Atomic, Molecular and Optical Physics* **35**, R147 (2002).
- [19] A. M. Popov, O. V. Tikhonova, and E. A. Volkova, *Journal of Physics B: Atomic, Molecular and Optical Physics* **36**, R125 (2003).
- [20] F. Morales, M. Richter, S. Patchkovskii, and O. Smirnova, *Proceedings of the National Academy of Sciences* **108**, 16906 (2011).
- [21] A. Scrinzi, N. Elander, and B. Piraux, *Phys. Rev. A* **48**, R2527 (1993).
- [22] M. V. Fedorov and A. M. Movsesian, *J. Phys. B: At. Mol. Opt. Phys.* **21**, L155 (1988).
- [23] O. V. Tikhonova, E. A. Volkova, A. M. Popov, and M. V. Fedorov, *Phys. Rev. A* **60**, R749 (1999).
- [24] J. Parker and C. R. Stroud, *Phys. Rev. A* **41**, 1602 (1990).
- [25] M. V. Fedorov and M. Y. Ivanov, *J. Opt. Soc. Am. B* **7**, 569 (1990).
- [26] K. C. Kulander, K. J. Schafer, and J. L. Krause, *Phys. Rev. Lett.* **66**, 2601 (1991).
- [27] K. Burnett, P. L. Knight, B. R. M. Piraux, and V. C. Reed, *Phys. Rev. Lett.* **66**, 301 (1991).
- [28] F. Benvenuto, G. Casati, and D. L. Shepelyansky, *Phys. Rev. A* **45**, R7670 (1992).
- [29] R. R. Jones and P. H. Bucksbaum, *Phys. Rev. Lett.* **67**, 3215 (1991).
- [30] E. Wells, I. Ben-Itzhak, and R. R. Jones, *Phys. Rev. Lett.* **93**, 023001 (2004).
- [31] L. D. Noordam, H. Stapelfeldt, D. I. Duncan, and T. F. Gallagher, *Phys. Rev. Lett.* **68**, 1496 (1992).
- [32] J. H. Hoogenraad, R. B. Vrijen, and L. D. Noordam, *Phys. Rev. A* **50**, 4133 (1994).

- 
- [33] M. P. de Boer and H. G. Muller, Phys. Rev. Lett. **68**, 2747 (1992).
- [34] N. J. van Druten *et al.*, Phys. Rev. A **55**, 622 (1997).
- [35] P. Kapitza and P. Dirac, Proc. Camb. Philos. Soc. **29**, 297 (1933).
- [36] S. Altshuler, L. M. Frantz, and R. Braunstein, Phys. Rev. Lett. **17**, 231 (1966).
- [37] P. L. Gould, G. A. Ruff, and D. E. Pritchard, Phys. Rev. Lett. **56**, 827 (1986).
- [38] C. Salomon *et al.*, Phys. Rev. Lett. **59**, 1659 (1987).
- [39] Y. B. Ovchinnikov *et al.*, Phys. Rev. Lett. **83**, 284 (1999).
- [40] C. Maher-McWilliams, P. Douglas, and P. F. Barker, Nature Photonics **6**, 386 (2012).
- [41] D.-S. Guo and G. W. F. Drake, Phys. Rev. A **45**, 6622 (1992).
- [42] X. Li *et al.*, Phys. Rev. Lett. **92**, 233603 (2004).
- [43] M. A. Efremov and M. V. Fedorov, Journal of Physics B: Atomic, Molecular and Optical Physics **33**, 4535 (2000).
- [44] O. Smirnova, D. L. Freimund, H. Batelaan, and M. Ivanov, Phys. Rev. Lett. **92**, 223601 (2004).
- [45] A. E. Kaplan and A. L. Pokrovsky, Phys. Rev. Lett. **95**, 053601 (2005).
- [46] P. W. Smorenburg *et al.*, Phys. Rev. A **83**, 063810 (2011).
- [47] S. Ahrens, H. Bauke, C. H. Keitel, and C. MÅijller, Phys. Rev. Lett. **109**, 043601 (2012).
- [48] D. L. Freimund, K. Aflatooni, and H. Batelaan, Nature **413**, 142 (2001).
- [49] P. H. Bucksbaum, D. W. Schumacher, and M. Bashkansky, Phys. Rev. Lett. **61**, 1182 (1988).
- [50] C. T. Hebeisen *et al.*, Opt. Express **16**, 3334 (2008).
- [51] M. Heinen, Master's thesis, FakultÄdt fÅijr Mathematik, Informatik und Naturwissenschaften der RWTH Aachen, 2007.

- [52] F. Yergeau, G. Petite, and P. Agostini, *J. Phys. B* **19**, L663 (1986).
- [53] M. Lewenstein *et al.*, *Phys. Rev. A* **49**, 2117 (1994).
- [54] F. Krausz and M. Ivanov, *Rev. Mod. Phys.* **81**, 163 (2009).
- [55] B. Walker *et al.*, *Phys. Rev. Lett.* **73**, 1227 (1994).
- [56] R. Moshhammer *et al.*, *Phys. Rev. Lett.* **84**, 447 (2000).
- [57] W. Becker, X. Liu, P. J. Ho, and J. H. Eberly, *Rev. Mod. Phys.* **84**, 1011 (2012).
- [58] P. B. Corkum, *Phys. Rev. Lett.* **71**, 1994 (1993).
- [59] J.-H. Huang, S. Wölk, S.-Y. Zhu, and M. S. Zubairy, *Phys. Rev. A* **87**, 022107 (2013).
- [60] H. B. van Linden van den Heuvell and H. G. Muller, in *Multiphoton processes*, edited by S. J. Smith and P. L. Knight (Cambridge University Press, Cambridge, 1988).
- [61] T. F. Gallagher, *Phys. Rev. Lett.* **61**, 2304 (1988).
- [62] P. B. Corkum, N. H. Burnett, and F. Brunel, *Phys. Rev. Lett.* **62**, 1259 (1989).
- [63] J. G. Story, D. I. Duncan, and T. F. Gallagher, *Phys. Rev. Lett.* **70**, 3012 (1993).
- [64] M. Gajda, J. Grochmalicki, M. Lewenstein, and K. Rzazewski, *Phys. Rev. A* **46**, 1638 (1992).
- [65] H. G. Muller, *Phys. Rev. Lett.* **83**, 3158 (1999).
- [66] M. Pont and M. Gavrila, *Phys. Rev. Lett.* **65**, 2362 (1990).
- [67] H. Zimmermann, J. Buller, S. Eilzer, and U. Eichmann, *Phys. Rev. Lett.* **114**, 123003 (2015).
- [68] U. Eichmann, T. Nubbemeyer, H. Rottke, and W. Sandner, *Nature* **461**, 1261 (2009).
- [69] T. Nubbemeyer, Dissertation, Technische Universität Berlin, 2010.
- [70] A. Robert *et al.*, *Science* **292**, 461 (2001).

- [71] F. Penent *et al.*, Phys. Rev. Lett. **86**, 2758 (2001).
- [72] A. Browaeys *et al.*, Phys. Rev. A **64**, 034703 (2001).
- [73] J. B. Anderson and J. B. Fenn, Physics of Fluids **8**, 780 (1965).
- [74] C. Iaconis and I. Walmsley, Optics Letters **23**, 792 (1998).
- [75] T. Nubbemeyer and U. Eichmann, The European Physical Journal Special Topics **222**, 2267 (2013).
- [76] U. Eichmann *et al.*, Phys. Rev. Lett. **110**, 203002 (2013).
- [77] M. Klaiber and D. Dimitrovski, Phys. Rev. A **91**, 023401 (2015).
- [78] E. Wells, I. Ben-Itzhak, and R. R. Jones, Phys. Rev. Lett. **93**, 023001 (2004).
- [79] V. S. Popov, Physics-Uspekhi **47**, 855 (2004).
- [80] N. B. Delone and V. P. Krainov, J. Opt. Soc. Am. B **8**, 1207 (1991).
- [81] J. P. Farrell *et al.*, Opt. Lett. **35**, 2028 (2010).
- [82] L. Shi *et al.*, Phys. Rev. Lett. **107**, 095004 (2011).
- [83] R. E. Sapiro, R. Zhang, and G. Raithel, Phys. Rev. A **79**, 043630 (2009).
- [84] H. Batelaan, Rev. Mod. Phys. **79**, 929 (2007).